UC San Diego

UC San Diego Electronic Theses and Dissertations

Title

Small River Plumes in the Surf Zone and Inner-Shelf: Climatic Variability, Transport, and Fate

Permalink

https://escholarship.org/uc/item/838833xp

ISBN

9798171611057

Author

Byrne, Sierra Michelle

Publication Date

2026-10-23

Peer reviewed|Thesis/dissertation

eScholarship.org Powered by the California Digital Library
University of California

UNIVERSITY OF CALIFORNIA SAN DIEGO

Small River Plumes in the Surf Zone and Inner-Shelf: Climatic Variability, Transport, and Fate

A dissertation submitted in partial satisfaction of the
requirements for the degree Doctor of Philosophy

in

Oceanography

by

Sierra Michelle Byrne

Committee in charge:

Professor Sarah N. Giddings, Co-Chair
Professor Mark A. Merrifield, Co-Chair
Professor Alexandra K. Heaney
Professor Alexander R. Horner-Devine
Professor Morgan C. Levy

2026

Copyright

Sierra Michelle Byrne, 2026

All rights reserved.

The Dissertation of Sierra Michelle Byrne is approved, and it is acceptable in quality and form for publication on microfilm and electronically.

University of California San Diego

2026

TABLE OF CONTENTS

Dissertation Approval Page . . . iii

Table of Contents . . . iv

List of Figures . . . vi

List of Tables . . . viii

Acknowledgements . . . ix

Vita . . . xi

Abstract of the Dissertation . . . xii

Chapter 1 Introduction . . . 1

Chapter 2 Southern California winter precipitation variability reflected in 100-year ocean salinity record . . . 6
2.1 Introduction . . . 6
2.2 Results and Discussion . . . 9
2.2.1 Precipitation Influence on Surface Salinity . . . 9
2.2.2 Surface Salinity and Climate Modes . . . 15
2.2.3 Implications . . . 19
2.3 Methods and Data . . . 21
2.3.1 Salinity Data . . . 21
2.3.2 Precipitation and Streamflow . . . 22
2.3.3 Climate Indices and Atmospheric Variables . . . 22
2.4 Acknowledgments . . . 23
2.5 Supplementary Information . . . 23

Chapter 3 Processes impacting the fate of small river plumes following storms . . . 28
3.1 Introduction . . . 28
3.1.1 Large vs. Small Plume Dynamical Regions . . . 29
3.1.2 Dynamics Influencing Small Plumes . . . 30
3.1.3 Outline . . . 32
3.2 Data and Methods . . . 33
3.2.1 Study Region . . . 33
3.2.2 Observations . . . 35
3.2.3 Data Processing . . . 36
3.3 General Conditions . . . 40
3.4 Regimes of Plume Formation . . . 41
3.4.1 Creation of Plume Formation Parameter Q^*_{reg} . . . 41

3.4.2 Parameter Implications . . . 45
3.5 Case Studies: Plume Transport . . . 49
3.5.1 General Conditions . . . 49
3.5.2 Surf Zone Impacts . . . 50
3.5.3 Wind Impacts . . . 55
3.5.4 Buoyancy Impacts . . . 59
3.6 Discussion . . . 64
3.6.1 Conceptual Overview & Dynamical Plume Regimes . . . 64
3.6.2 Applicability to Other Systems . . . 66
3.6.3 Plume Mixing . . . 69
3.7 Conclusions . . . 71
3.A Q^*_{reg} Derivation and Calculation . . . 74
3.B Supplementary Information . . . 77

Chapter 4 Surf zone influence on inter-estuary connectivity and river plume coalescence from low-inflow estuaries . . . 79
4.1 Introduction . . . 79
4.2 Materials and Methods . . . 83
4.2.1 Numerical Model . . . 83
4.2.2 Coordinate Systems and Velocity . . . 87
4.2.3 Stratification . . . 87
4.2.4 Surf Zone Quantities . . . 88
4.2.5 Estuary Volume Transport (Q_{mouth}) . . . 89
4.2.6 Dye as a Plume Tracer . . . 89
4.2.7 In-Estuary Plume Extent . . . 91
4.3 Results . . . 91
4.3.1 Freshwater Input to the Ocean . . . 91
4.3.2 Patterns of Plume Coalescence . . . 98
4.3.3 Surf Zone Plume Coalescence Near-Mouth . . . 99
4.3.4 Far-Field of Surf Zone Plume Coalescence . . . 104
4.3.5 Intrusion of Incoming Plume into Local Estuary . . . 107
4.4 Discussion . . . 108
4.4.1 Surf Zone Plume Coalescence . . . 108
4.4.2 Far-Field/ Surf Zone Plume Interactions . . . 111
4.4.3 Surf Zone Pathway for Inter-Estuary Connectivity . . . 112
4.4.4 Implications for Water Quality . . . 114
4.5 Conclusions . . . 118
4.6 Supplementary Information . . . 122

Chapter 5 Conclusions . . . 123

Bibliography . . . 125

LIST OF FIGURES

Figure 2.1. Time series of local sea surface salinity, precipitation, and streamflow. 9

Figure 2.2. Sea surface salinity preceding and following streamflow events of three magnitudes. 11

Figure 2.3. Seasonal cycles of sea surface salinity, precipitation, and streamflow. 13

Figure 2.4. The SSS_{10} metric presented alongside winter precipitation and streamflow anomalies and relevant climate indices. 15

Figure 2.5. Correlation of the SSS_{10} metric with US precipitation. 16

Figure 2.6. Division of SSS_{10} by relevant climate indices. 16

Figure 2.7. Composite atmospheric conditions for three combinations of climate modes and SSS_{10} wet vs. dry winter groupings. 18

Figure 2.8. Map of the study region. 24

Figure 2.9. Correlations of winter salinity anomaly quantiles with streamflow and precipitation anomalies. 25

Figure 2.10. Winter SSS_{10} timeseries at Scripps Pier and Newport Beach. 26

Figure 2.11. Probability density function of streamflow in salty to fresh SSS_{10} years. 27

Figure 3.1. Map of study region with mooring deployment locations. 34

Figure 3.2. Full winter timeseries of environmental drivers and mooring data. . . 39

Figure 3.3. Parameter Q^*_{reg} and its components. 44

Figure 3.4. Snapshots of data during cases 1, 2, and 3. 47

Figure 3.5. Comparison of three case studies in hours since event start. 48

Figure 3.6. Comparison of plume arrival speed with inner-shelf and surf zone currents. 51

Figure 3.7. Inner-shelf velocities during plume events compared to estimated wind- and buoyancy-driven velocities. 56

Figure 3.8. Vertical velocity shear squared (S^2) and plume depth for each case. . 60

Figure 3.9. Schematic representation of observed plume transport for cases 1, 2, and 3. 63

Figure 3.10. Comparison of data with near-field trapping parameter. 67

Figure 3.B.1. Parameter Q^*_{reg} calculated with both estimated and observed Q_{total}. . 78

Figure 4.1. COAWST model domain and locations of freshwater input. 84

Figure 4.2. 14-months of data including forcings and plume responses. 92

Figure 4.3. Maps of percent plume occurrence and plume coalescence. 96

Figure 4.4. Snapshots of surface salinity and dye for LPL and SDL for 3 continuation and 3 export coalescence examples. 100

Figure 4.5. Comparison of near-mouth grid line transect data for 3 continuation and 3 export cases. 101

Figure 4.6. Snapshots of surface salinity and dye for LPL and SDL for 2 events in the far-field following coalescence events. 104

Figure 4.7. Cross-sectional averages of variables during 2 events in the far-field following coalescence events. 105

Figure 4.8. Plume intrusion into adjacent LIE up-estuary extent compared to timing and strength of tides. 107

Figure 4.9. Alongshore extent of plumes in the surf zone and on the inner-shelf. 113

Figure 4.10. Far-field surface vs depth integrated plume concentration with distance offshore. 115

Figure 4.11. Comparison of wave properties (S_{xx}, S_{xy}, and v_{SZ}) between two estimation methods. 122

LIST OF TABLES

Table 3.1. Physical parameters for each case. 50

ACKNOWLEDGEMENTS

This work would not have been possible without the unwavering support of my advisors, Mark and Sarah. Thank you both for giving me the guidance and freedom that I needed to grow. Mark, thank you for giving me the chance to start this journey and for fostering my excitement to explore new data. Sarah, your kind and empathetic nature is inspirational. Thank you for always listening and for teaching me how to do rigorous, thorough science.

Thank you to my committee members, Alex Heaney and Morgan Levy, for your enthusiasm and support throughout this process. Thank you to my coauthors and collaborators for your contributions to these works. And a special thanks to my committee member Alex Horner-Devine, your excitement about my research has helped me remember the bigger picture when I have been lost in the weeds. I am grateful to the whole PiNC team for welcoming me on board and for the fruitful discussions. I have also been inspired and supported by a number of mentors from high school to present day, especially Baskin, Ng, Janet, and Sophia, thank you all for the opportunities to grow.

Thank you to the CPG field crew for taking me in and teaching me so much about data collection. Our science is only possible because of you. To my fellow CCS folks, it brightened my days to share an office space with you. To my labmates in CPG and in the Giddings lab, I loved growing together and I have learned so much from you all.

Importantly, this dissertation would not have been possible without the support of my family and friends. To my family, thank you for shaping me into the person I am today. Your love and constant encouragement means the world to me. To my friends from home, college, rowing, and Scripps, thank you for reminding me to have fun along the way. To Joshua Tree, it was so special to meet like-minded folks to share this experience with and I am so glad we went on this rollercoaster together. To Dylan, you are my rock and I am forever grateful for you.

While I never had the honor of meeting Nirnimesh Kumar, I know my dissertation

research is largely possible because of paths he carved. I thank him for shining a light so bright that it continues to inspire us all.

Chapter 2, in full, is a reprint of the paper "Southern California winter precipitation variability reflected in 100-year ocean salinity record" published in Communications Earth & Environment by Byrne, S.M.; Merrifield, M.A.; Carter, M.L.; Cayan, D.R.; Flick, R.E.; Gershunov, A.; and Giddings, S.N. in 2023. The dissertation author was the primary investigator and author of this paper.

Chapter 3, in full, is a reprint of the paper "Processes impacting the fate of small river plumes following storms" published in Journal of Geophysical Research: Oceans by Byrne, S.M.; Giddings, S.N.; Merrifield, M.A.; Horner-Devine, A.R.; Spydell, M.S.; Simpson, A.J.; and O'Reilly, W.C. in 2026. The dissertation author was the primary investigator and author of this paper.

Chapter 4, in full, is currently being prepared for submission for publication of the material. Byrne, S.M.; Giddings, S.N.; Merrifield, M.A.; Horner-Devine, A.R.; Spydell, M.S.; and Lou, Y. The dissertation author was the primary investigator and author of this material.

VITA

2021	Bachelor of Science, Atmospheric and Oceanic Sciences - University of California San Diego, USA
2024	Master of Science, Oceanography - University of California San Diego, USA
2026	Doctor of Philosophy, Oceanography - University of California San Diego, USA

PUBLICATIONS

Southern California winter precipitation variability reflected in 100-year ocean salinity record Byrne, S.M.; Merrifield, M.A.; Carter, M.L.; Cayan, D.R.; Flick, R.E.; Gershunov, A.; and Giddings, S.N. Communications Earth & Environment 4 (1), 143 (2023)

Processes impacting the fate of small river plumes following storms Byrne, S.M.; Giddings, S.N.; Merrifield, M.A.; Horner-Devine, A.R.; Spydell, M.S.; Simpson, A.J.; and O'Reilly, W.C. Journal of Geophysical Research: Oceans 131, e2026JC024342 (2026)

Convergent surf zone currents and rips dominate cross-shore transport of freshwater from a small estuary Lou, Y.; Horner-Devine, A.R.; Giddings, S.N.; Derakhti, M.; Spydell, M.S.; Simpson, A.J.; Byrne, S.M.; and Quinn, K.J. *in review Journal of Geophysical Research: Oceans*

ABSTRACT OF THE DISSERTATION

Small River Plumes in the Surf Zone and Inner-Shelf: Climatic Variability, Transport, and Fate

by

Sierra Michelle Byrne

Doctor of Philosophy in Oceanography

University of California San Diego, 2026

Professor Sarah N. Giddings, Co-Chair
Professor Mark A. Merrifield, Co-Chair

River plumes serve as major sources of terrestrial runoff into the coastal ocean, carrying land-based and estuary-modified particles, sediment, debris, and pollutants. Understanding river plume transport across temporal and spatial scales is important for assessing impacts on ecosystem and human health. This dissertation investigates variability in small river plume occurrence and transport from the low-inflow estuary (LIE) Los Peñasquitos Lagoon (LPL) in San Diego, California and has findings relevant to LIEs globally, which are common but under-studied.

I show the occurrence of small river plumes in the far-field is influenced by climate

patterns using 105 years of daily salinity measurements. Climate oscillations influence precipitation which impacts the tendency for small plumes to transport significantly into the far-field. This work illustrates that small, intermittent LIE plumes have a robust impact on coastal ocean freshening when there is enough rainfall. With higher resolution LPL plume observations collected during the Plumes in Nearshore Conditions (PiNC) experiment, I specify when small plumes occur depending on river, tidal, and wave forces using a reproducible parameter. I also show the variable nature of small plume far-field transport within one winter. The surf zone can change far-field plume behavior and control when and where plumes reach the inner-shelf. Once on the shelf, plumes following rain events are driven alongshore in the direction of the wind with a speed enhanced by buoyancy. To better resolve the processes around LPL and adjacent estuaries, a realistic coupled wave-ocean model is run. I find that the surf zone is a common pathway for plume coalescence, the interaction of two river's plumes, between LIEs. When one LIE's surf zone plume reaches an adjacent LIE, the incoming plume can continue in the surf zone with the local ebbing plume, or it can be forced offshore by the ebbing plume thus altering its fate. Alternatively, an incoming plume reaching an adjacent LIE during flood tide intrudes into the local estuary, impacting coastal dispersion and plume fate. Together, these chapters advance knowledge about the response of small plumes to varying conditions in the surf zone and inner-shelf, informing coastal transport of terrestrial materials including pollutants.

Chapter 1

Introduction

Rivers have an important impact on the ocean, discharging around 36,000 km^3 of freshwater and more than 20 billion tons of solid and dissolved material each year (Milliman, Farnsworth, 2013). Freshwater from rivers influences coastal circulation in the ocean and alters transport pathways of important constituents along the coast (Banas et al., 2009; Hickey et al., 2005, 2009; Giddings et al., 2014; Mazzini et al., 2014). River-derived constituents, such as nutrients, larvae, sediment, and pollutants, reach the coastal ocean (Roegner et al., 2002; Swieca et al., 2020) and open ocean (Sharples et al., 2017). The impacts of river-derived and estuary-modified materials on the ocean can be positive, neutral, or negative. Terrestrial nutrients can boost primary productivity and species abundance in the ocean (Liu et al., 2009; Hickey et al., 2010; Vargas-Fonseca et al., 2016), but can also cause harmful algal blooms and hypoxia in bottom waters (Cloern, 2001; Rabouille et al., 2008). Pollutants and pathogens carried to the ocean can cause swimmer illness in nearby beaches (Reeves et al., 2004; Feddersen et al., 2021). The transport of land-based sediment into the ocean contributes to coastal sediment budgets that impact hydrodynamics (Milliman, Syvitski, 1992; Syvitski, Milliman, 2007; Vundavilli et al., 2024). To understand these diverse impacts, it is critical to study the occurrence, transport, and fate of river waters in the coastal ocean.

The interaction of river freshwater with ocean water forms horizontally advecting

river plumes (Ryther et al., 1967; Wright, Coleman, 1971; Boicourt, 1973; Garvine, 1974). River plumes from high discharge rivers are better understood than small river plumes that originate from low-inflow (low discharge) estuaries (Horner-Devine et al., 2015; Fong et al., 1997; Geyer et al., 2000; Wong et al., 2013). Plumes may be defined as large or small based on a number of definitions. Plumes can be considered small if they: have low incoming river discharge (e.g., from low-inflow estuaries; Largier, 2023), can stop formation during flood tides, are not impacted by the Earth's rotation (Cole, Hetland, 2016; Garvine, 1995), or are impacted by the surf zone (Wong et al., 2013; Rodriguez et al., 2018). Small plumes can originate from smaller watersheds and/or regions with less rainfall or meltwater input and hence lower streamflow input (Warrick, Fong, 2004; Largier, 2023). In this dissertation, I explore small plumes that originate from low-inflow estuaries along the southern California coast that meet all of the above definitions. Despite their size, small plume systems are more numerous, can collectively impact a greater cumulative ocean area when measured against a single large river of comparable watershed size (Warrick, Fong, 2004; Mazzini et al., 2014), and can influence coastal ocean biogeochemistry and ecosystems (Wetz et al., 2006; Vargas et al., 2006; Vargas-Fonseca et al., 2016).

Smaller rivers, estuaries, and their river plumes can impact coastal ecosystems. One study shows that the distance between a surf zone location and the nearest estuary has a greater impact than the wave conditions or degree of urbanization on the distribution of fish species in the surf zone (Vargas-Fonseca et al., 2016). There is evidence of larvae accumulation in the Maipo River plume front, impacting species distribution in the nearshore (Vargas et al., 2006). Small rivers in southern California can contain nutrients like nitrogen and phosphorus, e.g. from agricultural runoff, and have been shown to influence nutrients and alkalinity in the coastal ocean (Rodrigues et al., 2009; Paulsen et al., 2018; Howard et al., 2014; Ho et al., 2023). Small river plumes can also pose a risk to human health due to their direct interaction with, and presence in, the surf zone where swimmers and surfers recreate (Grant et al., 2005; Wong et al., 2013; Feddersen

et al., 2021). Fecal indicator bacteria are found in runoff in southern California coastal watersheds and can enter the coastal ocean and surf zone (Reeves et al., 2004; Wong et al., 2013). An example of this is the Tijuana River plume which is routinely polluted with untreated wastewater and causes swimmer illness due to norovirus (Feddersen et al., 2021). Thus, understanding small plume transport is critical for understanding how sediment, nutrients, larvae, organisms, and pollutants move around the coastal regions and impact human and ecosystem health.

A small plume discharging into the ocean can be retained within the surf zone if the onshore-directed wave momentum is stronger than the offshore-directed river momentum (Wong et al., 2013; Rodriguez et al., 2018; Kastner et al., 2019; Lou et al., 2025). The resulting surf zone plume is subject to wave-driven dynamics including radiation stresses and vertical mixing caused by wave injection of turbulent kinetic energy (Guza et al., 1986; Feddersen et al., 1998; Feddersen, Trowbridge, 2005; Feddersen, 2012; Hally-Rosendahl et al., 2014; Kumar, Feddersen, 2017; Spydell et al., 2019; Kastner et al., 2023). The cross-shore gradient of the shear component of wave radiation stress can drive an alongshore current within the surf zone (Bowen, 1969; Longuet-Higgins, 1970) that transports plumes alongshore with a direction dependent on the local wave incidence angle (Rodriguez et al., 2018; Kastner et al., 2019; Baldoni et al., 2022; Brasseale et al., 2023) and channel angle (Wong et al., 2013). Alongshore convergence in surf zone velocity can create transient rip currents, and bottom features can drive bathymetric rip currents, both of which export surf zone waters offshore (Kumar, Feddersen, 2017; Hally-Rosendahl et al., 2015; Moulton et al., 2017; Grimes et al., 2020). The surf zone tends to be vertically homogeneous due to strong vertical mixing induced by wave breaking (Thornton, Guza, 1983; Feddersen, Trowbridge, 2005; Feddersen, 2012; Kumar et al., 2012), although surf zone stratification has been documented in the presence of a river plume (Kastner et al., 2023). While studies of small plumes have increased in recent years (Piñones et al., 2005; Warrick et al., 2007; Kniskern et al., 2011; Osadchiev et al., 2021; Romero et al., 2016; Baldoni et al., 2022;

Basdurak, Largier, 2022; Lemos et al., 2022; Vundavilli et al., 2024; Speiser, Largier, 2024), only a handful resolve surf zone dynamics (Wong et al., 2013; Rodriguez et al., 2018; Kastner et al., 2019, 2023; Lou et al., 2025). There is a need to understand how surf zone processes impact the transport and eventual fate of small plumes.

The physics impacting large and small plumes differ. While small plumes often interact with the surf zone, large plumes tend to be confined by jetties and structures that limit their interaction with the surfzone (Wong et al., 2013; Hickey et al., 1998). Moreover, strong discharge allows large plumes to form strong momentum jets that move material offshore in the near-field. In large plume's far-field, away from the influence of river momentum, the dynamics are typically dominated by rotation, wind, and buoyancy (Lemagie, Lerczak, 2020). Leading balances in a large plume's far-field often involve rotation, e.g. Ekman wind and geostrophic balances (Fong et al., 1997; Geyer et al., 2000; Fong, Geyer, 2001; Toublanc et al., 2023; Yankovsky, Yankovsky, 2024), while small plumes experience negligible rotational effects (Garvine, 1995; Warrick et al., 2007; Basdurak et al., 2020). Instead, small plumes have been shown to have a far-field dominated by direct wind forcing and advection (Piñones et al., 2005; Warrick et al., 2007; Kniskern et al., 2011; Osadchiev et al., 2021; Romero et al., 2016; Basdurak, Largier, 2022; Lemos et al., 2022; Vundavilli et al., 2024). The interaction, or coalescence, of multiple river's plumes occurs under different conditions for large and small plumes and can alter the fate of coastal plumes by impacting their transport and mixing (Warrick, Farnsworth, 2017; Saldías et al., 2012; Salcedo-Castro et al., 2020; Rosa et al., 2022; Vundavilli et al., 2024; Collins, Macdonald, 2025). No prior studies detail surf zone impacts on far-field plume dynamics nor potential for plume coalescence at and across the surf zone/ inner-shelf interface.

This dissertation advances the field's understanding of small river plume dynamics, with specific contributions to understanding the occurrence and fate of small river plumes under varying environmental and climate conditions across the surf zone and inner-shelf.

The following chapters investigate a variety of spatial and temporal scales of small plume transport from the low-inflow estuary Los Peñasquitos Lagoon, located in San Diego, CA. Chapter 2 explains how small plume transport varies on decadal time scales, as a result of climate oscillations, using 105 years of daily salinity measurements. Chapter 3 then zooms in on three case study plume events and uses high-frequency observations to explain what drives their transport across the surf zone and inner-shelf. This chapter also examines the conditions necessary for river plume formation to occur at low-inflow estuary mouths and derives a reproducible parameter for this purpose. Finally, Chapter 4 uses a numerical model to explain how the surf zone acts as a pathway for novel plume-to-plume interactions and for inter-estuary connectivity within multiple low-inflow systems.

Chapter 2

Southern California winter precipitation variability reflected in 100-year ocean salinity record

2.1 Introduction

Southern California precipitation, or lack thereof, occurs in extremity, resulting in multiyear droughts with sporadic years of heavy rainfall and nearly the highest year-to-year precipitation variability in the continental United States (Dettinger et al., 2011). Owing to its lower mid-latitude setting on the eastern flank of the North Pacific High, heavy precipitation occurs relatively rarely, but can carry high intensities (Beighley et al., 2003; Modrick, Georgakakos, 2015; Cannon et al., 2020), sometimes on par with those observed in climatologically wetter region of central California (Oakley et al., 2018). Climate change is projected to exacerbate this pre-existing hydroclimate volatility by reducing the frequency of low- to medium-intensity precipitation while increasing the intensity and contribution of extreme storms (Gershunov et al., 2019). Above-average rainfall years are critical for replenishing valuable water supplies to meet growing agricultural and direct human consumption needs. Precipitation also helps to moderate wildfire risk (Cayan et al., 2022), a costly consequence of dry foliage and long dry periods. In 2018 alone during a severe drought year, California's wildfires cost the US an estimated $148.5 billion

(Wang et al., 2021). The occurrence of extreme rain events and runoff can also have devastating effects across southern California in the form of flooding (Corringham et al., 2019; Committee on Natural Disasters, National Research Council, 1982; Liu et al., 2022), debris flow (Campbell, 1974), and contamination of coastal waters (Reeves et al., 2004; Aguilera et al., 2019).

The mean dry conditions in southern California result in local streams and rivers having little outflow during most of the year. When heavy rain events do occur, primarily during the winter season, outflow increases by orders of magnitude and plumes of freshwater propagate into the coastal ocean (Warrick et al., 2007). In addition, non-point source runoff delivers freshwater to coastal waters. Storm runoff is known to carry pollutants through watersheds to the ocean, reducing local water quality, increasing fecal indicator bacteria signals, and posing public health risks (Reeves et al., 2004; Aguilera et al., 2019). Runoff and river waters also carry other accumulated properties or quantities, including nutrients (important for biological productivity; Howard et al., 2014; Anderson et al., 2002) and sediment (important for coastal morphology and sand budgets; Syvitski, Milliman, 2007).

Climate indices often are used to characterize atmospheric and oceanic patterns favorable to wet or dry conditions over western North America (Ropelewski, Halpert, 1986; Gershunov, Barnett, 1998; Cayan et al., 1999). In particular for the southern California region, El Niño Southern Oscillation (ENSO) usually brings drought-like conditions in the La Niña phase and a higher probability of intense rainfall during strong El Niño years (Cayan et al., 1999). Other studies have considered the influence of the Pacific Decadal Oscillation (PDO) on winter rainfall in the study region (Mantua et al., 1997; Cayan et al., 1998; Shukla et al., 2015). Shukla et al. (2015) found that the negative PDO phase increases the probability of drought favorable conditions in southern California over the late winter months. PDO modulates ENSO teleconnections, including precipitation (Gershunov, Barnett, 1998), and contributes to seasonal precipitation prediction skill in the

study region (Gershunov, Cayan, 2003). Negative PDO and ENSO phases have been linked to increased fire activity in the southwestern US due to decreased precipitation (Westerling, Swetnam, 2003). These climate phases impact the hydrology in the study region due to the latitudinal shifts in the atmospheric pressure systems that are precipitation-bearing versus precipitation-blocking (Cayan et al., 1999).

In this study, we utilize sea surface salinity data to investigate precipitation and climate variability. Over a century of daily sea surface salinity measurements have been recorded at the Scripps Institution of Oceanography Pier. The standardized collection procedures (Carter et al., 2022) provide confidence that the salinity measurements are consistent over time. This long record enables a unique 105-year investigation of hydroclimate variation affecting the Southern California coastal region. Annual-averages of the pier salinity record have been used to assess wind-driven upwelling (Di Lorenzo et al., 2008), but freshwater spikes in the daily record have not been well characterized. In this paper, we demonstrate the potential for using coastal salinity to infer runoff from heavy rain events over the wet winter season when fresh salinity spikes are most prevalent. Here we use a 105-year daily sea surface salinity record to show that the El Niño Southern Oscillation and Pacific Decadal Oscillation both have signatures in coastal sea surface salinity even in a region which receives small total freshwater input (through either direct precipitation or runoff). Specifically, we find that the freshest salinity quantile is a good indicator of year-to-year variations in precipitation and runoff, highlighting the connection between the coastal ocean and the influence of storm activity, or lack thereof, in correspondence with known climate phase shifts.

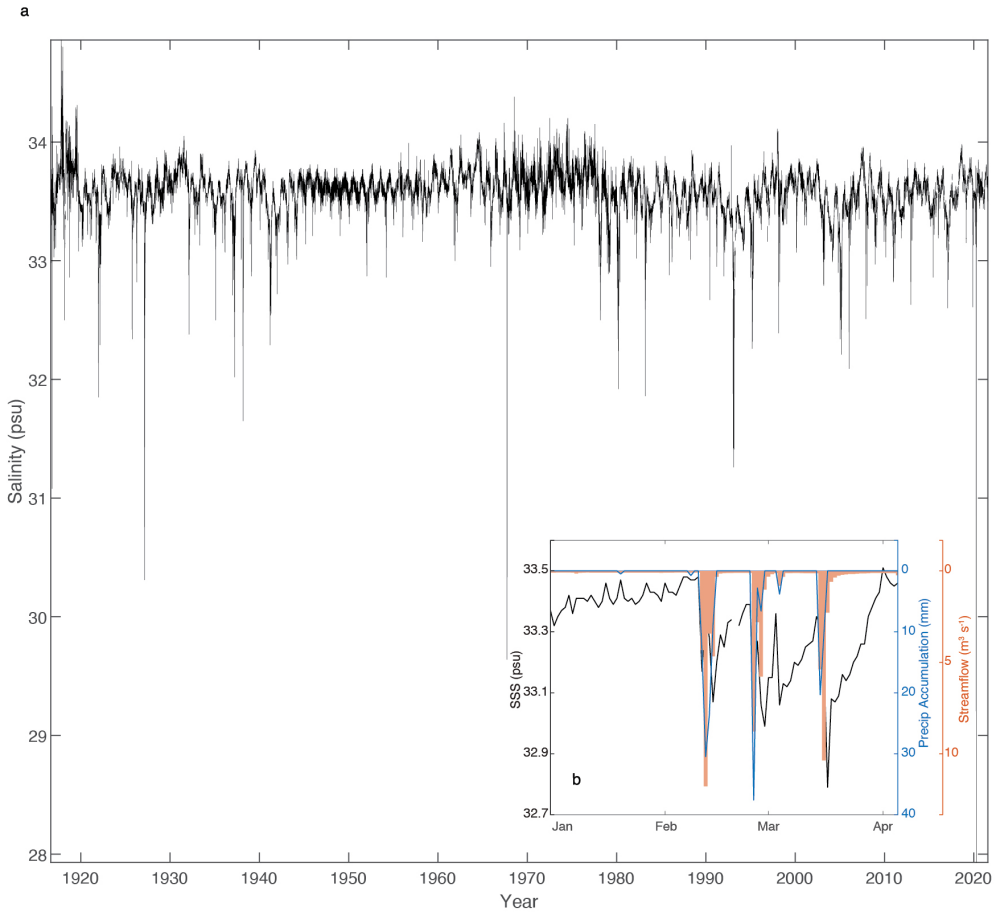


Figure 2.1. Time series of local sea surface salinity, precipitation, and streamflow. a) Daily sea surface salinity (SSS) measurements from surface water samples at the Scripps Pier, spanning 1916-2021. b) The correspondence between daily SSS (black), San Diego Airport daily rainfall (blue, inverted y-axis), and Los Peñasquitos daily streamflow (orange bars, inverted y-axis) is illustrated for January-March of 2003 to highlight a typical winter season.

2.2 Results and Discussion

2.2.1 Precipitation Influence on Surface Salinity

The daily SSS record from Scripps Pier (Figure 2.1a) exhibits spike-like fresh events ranging from -5.6 to -0.3 psu (Practical Salinity Unit), contributing to a negative skewness (-2.84) about a mean value of 33.58 psu. A blowup of the record during January through

March (JFM) for one year (2003 typifies average conditions) shows that the fresh SSS spikes align with winter rain events that last for 1-5 days (Figure 2.1b). Within 1-3 days following each rain peak, salinity at the pier drops abruptly by several tenths psu, and slowly returns to near pre-event values after several weeks. Local streamflow exhibit a near identical pattern to that of the precipitation over the events, with the streamflow peaking within a day of the maximum rainfall (Figure 2.1b). The SSS, precipitation, and streamflow measurements are recorded at locations within 20km of each other (see map in Supplementary Figure 2.8). To quantify this relationship over the longer record, we composite JFM SSS relative to streamflow anomalies, which confirms that, on average, SSS drops for weeks following sizeable outflow events (Figure 2.2). Compounding effects lead to variations in the timing and amplitude of the SSS response relative to a given streamflow or precipitation level. This is evident in the 2003 record (Figure 2.1b) as the largest rain event does not result in the lowest SSS response, but this largest SSS response is the third event in $\sim$ 1 month span.

Numerous factors influence ocean salinity in the study region. Coastal upwelling increases SSS by vertical transport of deep cold salty water to the surface and peaks in the April-July summer period (Schwing, Mendelssohn, 1997). Therefore, this work focusing on winter freshwater events does not investigate upwelling-induced changes. During rain events, atmospheric freshwater input lowers the salinity of the coastal ocean. An additional factor that directly alters surface salinity is horizontal advection. It is unspecified in existing literature whether offshore water mass advection variability influences the nearshore surface waters of the study region. The SSS drops seen at Scripps Pier are sudden and extreme, consistently corresponding in time with rain and streamflow spikes (Figure 2.1b and Figure 2.2). This suggests that the most practical mechanisms for these SSS drops are from precipitation directly, localized runoff during extreme events, and the precipitation-driven streamflow increases and resulting freshwater plumes that propagate into the coastal ocean. The connection between winter rain events and the SSS and hydrology of the

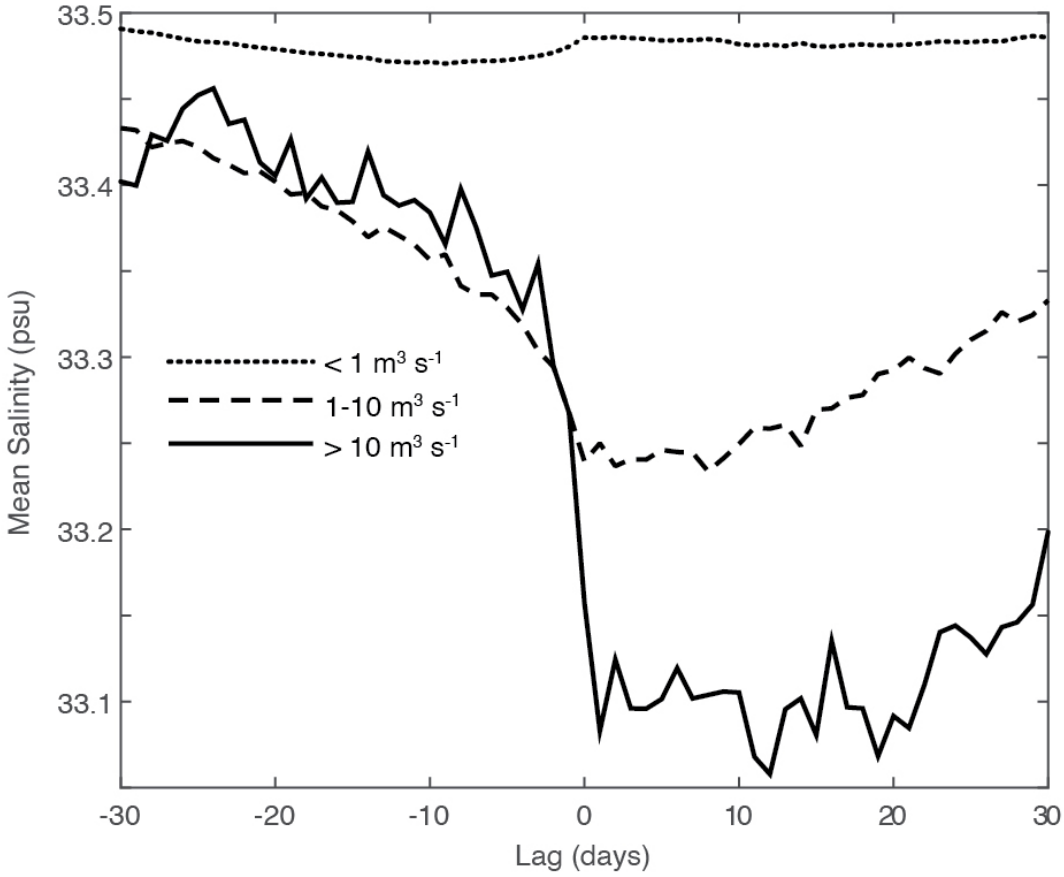


Figure 2.2. Sea surface salinity preceding and following streamflow events of three magnitudes. Sea surface salinity data shown 30 days prior and 30 days following Los Peñasquitos streamflow events of three categories, low flow $<1\ m^3s^{-1}$ (dotted line), medium flow 1-10 m^3s^{-1} (dashed line), and high flow $>10\ m^3s^{-1}$ (solid black line).

nearshore coastal zone in the region has not been examined to our knowledge on yearly to interdecadal time scales and will be a focus of this study. Interannual streamflow variability in larger river systems due to precipitation has been shown to change coastal ocean dynamics (Durocher et al., 2019; Déry, Wood, 2005). Our work shows that even small, intermittent freshwater plumes have a robust impact on coastal ocean freshening in the study region.

River plumes of this relatively fresh stormwater infiltrate the salty ocean waters with a plume area dependent on the amount of rainfall (Nezlin et al., 2005). The fate of

the plume depends on the relative strength of the discharge and the waves. Plumes during relatively small discharge and large waves are trapped in the surfzone and travel along the coast in the direction of the surfzone wave-driven currents (Wong et al., 2013; Rodriguez et al., 2018; Kastner et al., 2019), whereas intermediate to large discharge can escape the surfzone and travel along the coast depending upon the inner-shelf currents (Grimes et al., 2020; Hickey et al., 2005). The direction plumes travel in the inner-shelf varies with wind speed and direction, river discharge inertia, and buoyancy (Warrick et al., 2007). River plumes over the shelf in southern California frequently travel southward along the coast due to the relative timing of regional precipitation and wind patterns (Warrick et al., 2007), which has implications for the study site located 7.5 km south of the Los Peñasquitos Lagoon and 12 km south of the San Dieguito River (see map in Supplementary Figure 2.8). The interaction of freshwater discharge plumes with the surfzone and nearshore is a topic of active research. The SSS time delay relative to the peak rain/streamflow event suggests that the southward advection of local river plumes/estuary outflows contribute to the Scripps signal (Warrick et al., 2007). In addition, the SSS decay time likely reflects advective-diffusive time scales of the plume.

The fresh salinity events at Scripps Pier can occur throughout the year but are most prevalent during JFM (January-March), the three freshest months on average (Figure 2.3). The JFM winter season also corresponds to seasonal highs in Los Peñasquitos streamflow and San Diego Airport rainfall. Approximately half the annual rainfall in the San Diego Airport record occurs during JFM, consistent with estimates for the larger San Diego region (Hydroclimate Report Water Year 2016, https://water.ca.gov). We focus the remainder of our analyses on the JFM winter season of high rainfall, highest streamflow, and lowest salinity (Figure 2.3).

To represent the freshest winter salinity values, the 10% quantile of the JFM salinity anomaly (hereinafter referred to as SSS_{10}) is computed each year after removing the JFM average for that year to de-emphasize background oceanic variability. Similar salinity

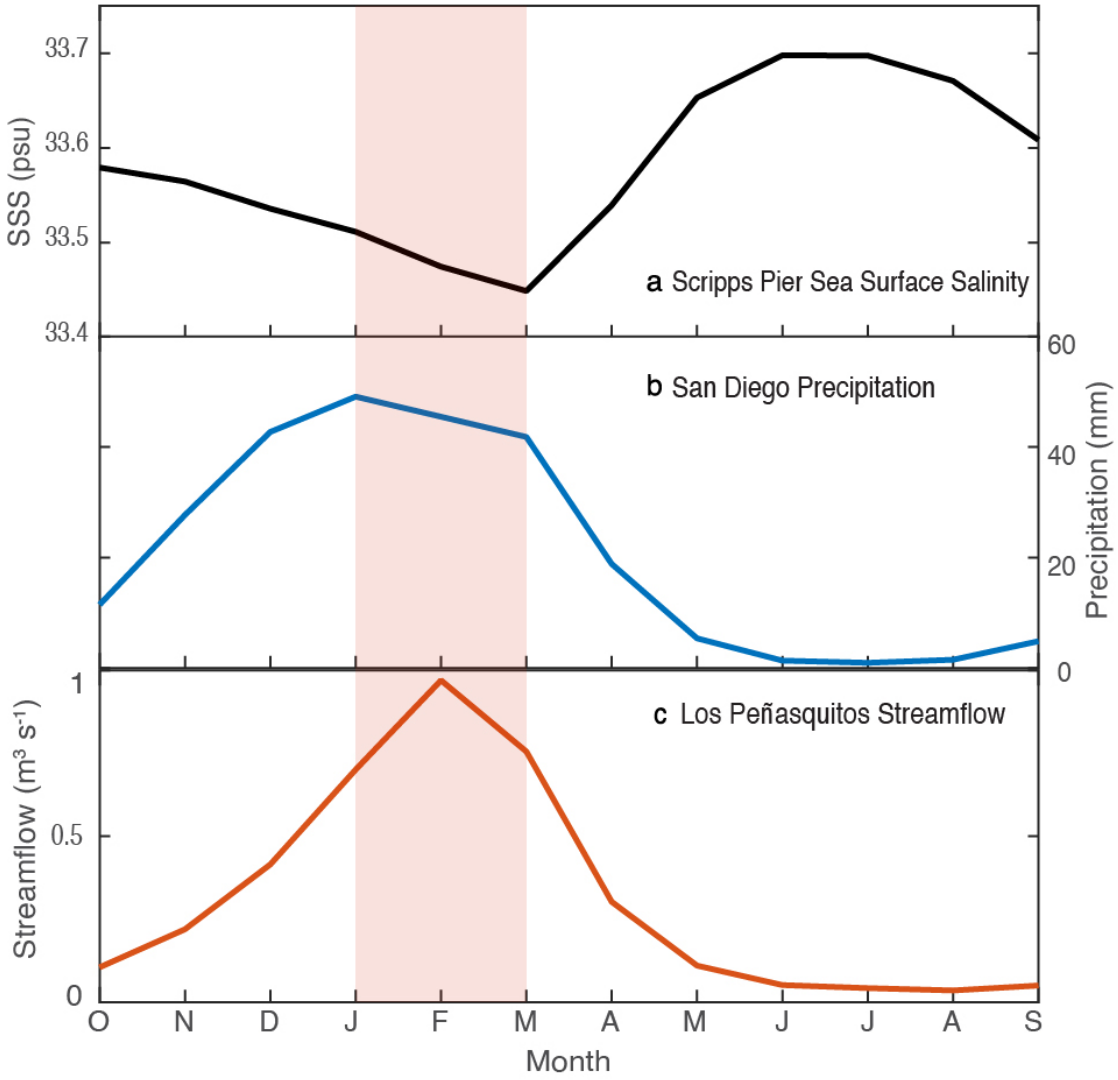


Figure 2.3. Seasonal cycles of sea surface salinity, precipitation, and streamflow. Average monthly values of a) SSS, b) accumulated precipitation at San Diego Airport (NOAA NCEI), and c) Los Peñasquitos streamflow (USGS). The red band highlights the wet winter JFM season.

values to SSS_{10} are obtained by subtracting the median quantile from the 10% quantile for each JFM season. The 10% quantile of the remaining anomaly array is the selected metric as it isolates the most extreme negative values for each year (see Supplementary Figure 2.9 for explanation of quantile calculations).

The SSS_{10} time series captures year-to-year freshening in the JFM winter season. In years of low precipitation, SSS_{10} (Figure 2.4a) remains relatively consistent at a near

zero anomaly (0 to -0.2 psu). The strong correlations of SSS_{10} to precipitation and streamflow (Supplementary Figure 2.9) further confirm that the 10% anomaly quantile characterizes the local response of SSS to rainfall. As a check on the representativeness and reliability of the Scripps SSS_{10} time series, we compare it to a similar estimate of the 10% quantile from the Newport Pier SSS measurements (Supplementary Figure 2.10). A strong significant ($p < 0.05$) correspondence between the SSS_{10} time series of Scripps and Newport ($r = 0.74$) suggests that the rain-related coastal SSS signal is widespread (i.e., not just representative at this one location) and robust in the daily pier measurements (i.e., not subject to changes in observers or methodology).

Together the SSS_{10}, streamflow, and precipitation highlight especially wet winters ($SSS_{10} < -0.35$) against a background of otherwise dry conditions (Figure 2.4a,b). The SSS_{10} record particularly emphasizes consecutive dry years during predominantly negative PDO phases (Figure 2.4a,c). A noteworthy feature in the SSS_{10} record is the negative PDO phase of 1944-1977 (Figure 2.4c) when the precipitation and streamflow are weak and the SSS_{10} is nearly constant for 30+ years. During the two extended negative PDO phases, with the exception of 2005, the JFM-averaged precipitation anomaly remains under 40 mm. In addition, multi-year droughts in excess of 3 years appear to be less apparent in the first 25 years of the SSS_{10} record, prior to the 30-year long dry period. While dry winters tend to occur sequentially, one low SSS/wet winter is rarely followed by another. A potential source of this shorter-term variability in SSS_{10}/precipitation is ENSO phase (Figure 2.4d).

The tails of the daily streamflow distributions (Supplementary Figure 2.11) highlight differences in the number of large outflow events during fresh, moderately fresh, and salty years. In salty years, the probability of rain events causing sustained high streamflow is much lower than that of the freshest years. The fresh years that feature the largest SSS_{10} anomalies (Figure 2.4a) correspond to generally higher chances of sustained intense streamflow (Supplementary Figure 2.11). The distribution of streamflow highlights that

heavy rain events occur less frequently in salty/dry years than fresh years.

To further explore the connection between Scripps Pier salinity and regional winter precipitation patterns, we examine correlations between SSS_{10} and the Livneh gridded precipitation product (Livneh et al., 2013) for 1917-2011. JFM-averaged precipitation exhibits statistically significant correlations ($|r| > 0.20$) with SSS_{10} over a broad swath of the southwestern US, with the highest correlations (up to $r = -0.79$) in the Southern California region (Figure 2.5). The low SSS_{10}/high rain winters appear to be indicative of large-scale precipitation patterns that affect a large part of the Southwest region.

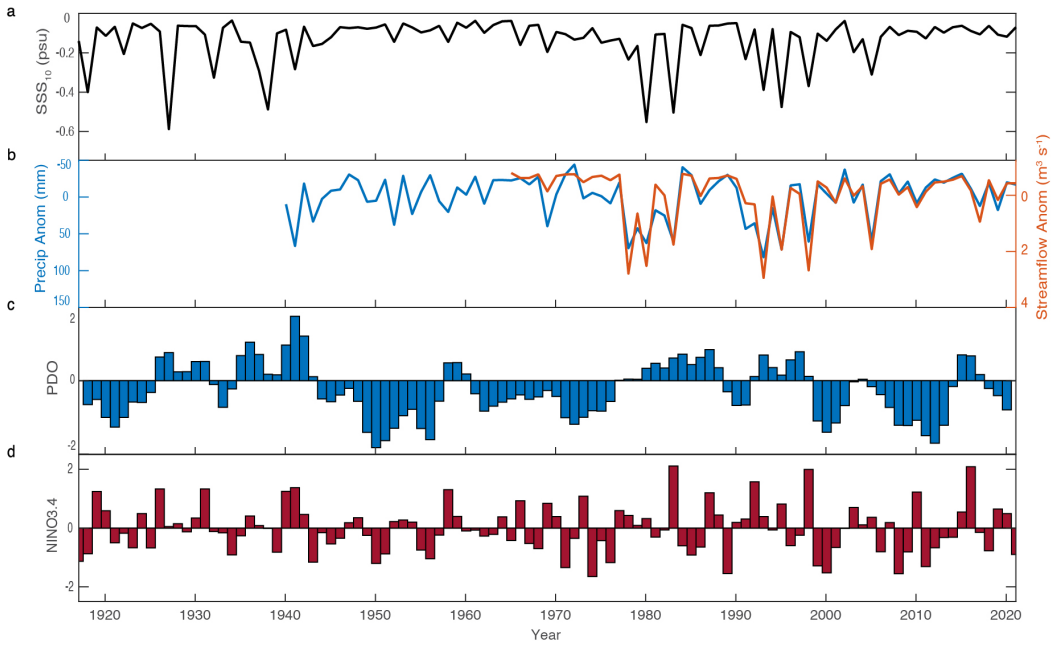


Figure 2.4. The SSS_{10} metric presented alongside winter precipitation and streamflow anomalies and relevant climate indices. a) SSS_{10} (1917-2021). b) JFM-averaged precipitation (blue, 1940-2021) and streamflow (orange, 1965-2021) anomalies with climatological monthly averages removed, shown with flipped y-axes. c) 5-year smoothed JFM-averaged PDO index values. d) JFM-averaged NINO3.4 index values.

2.2.2 Surface Salinity and Climate Modes

We next consider the extent to which Pacific climate modes can provide context and a degree of predictability for the JFM precipitation and runoff captured by the SSS_{10}

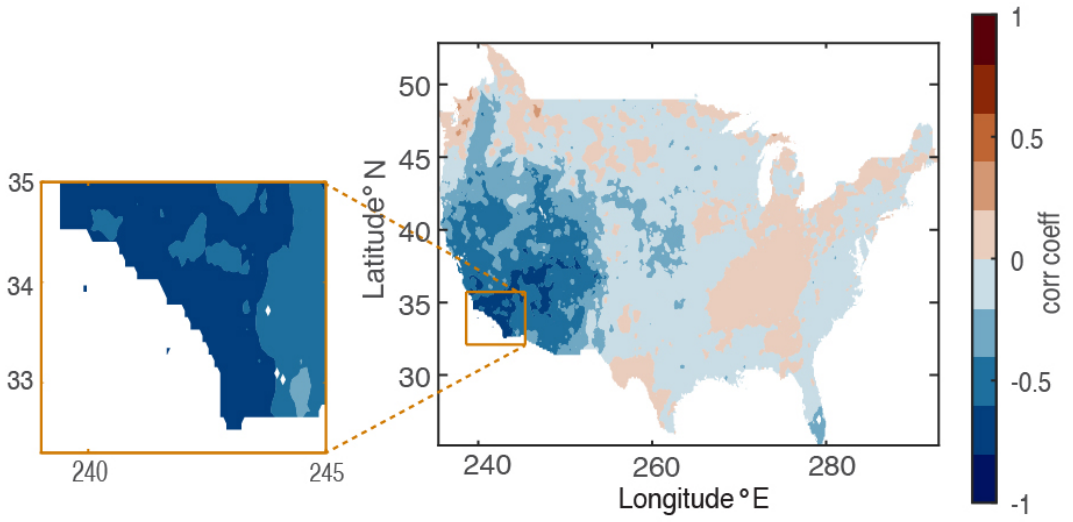


Figure 2.5. Correlation of the SSS_{10} metric with US precipitation. Correlation coefficient contour map of SSS_{10} to Livneh gridded precipitation (Livneh et al., 2013) (1917-2011). Inset on the left shows southern California north of the US-Mexico border and south of San Luis Obispo.

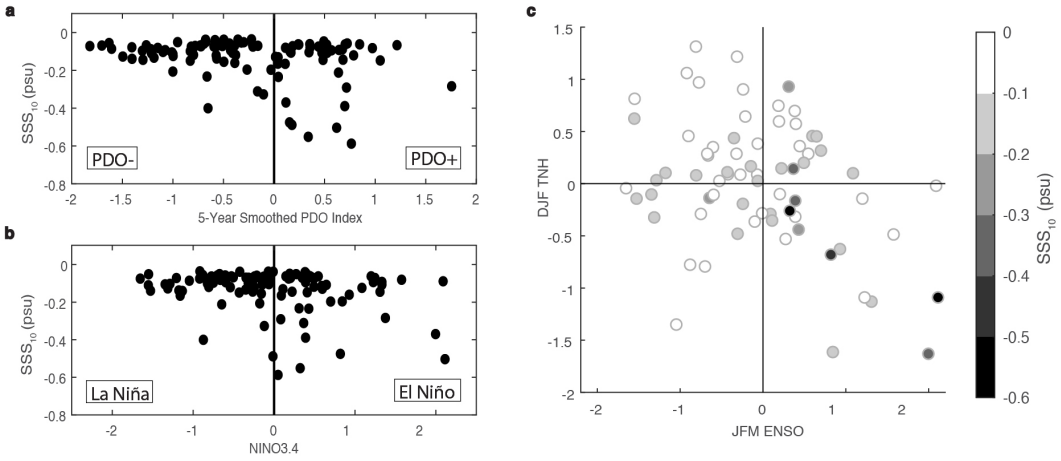


Figure 2.6. Division of SSS_{10} by relevant climate indices. Scatter of SSS_{10} (1917-2021) versus a) 5-year smoothed JFM-averaged PDO index and b) JFM-averaged NINO3.4 index. c) Scatter of JFM-averaged NINO3.4 index with DJF-averaged TNH index, colored by the corresponding SSS_{10} for each year (1951-2021).

time series. For comparison with SSS_{10}, the NINO3.4 and PDO indices are JFM-averaged. The strongest ENSO teleconnections, linking the tropical and midlatitude conditions, occur in JFM (Chapman et al., 2021). Correlations between SSS_{10} and PDO and ENSO indices

are weak with $r = -0.28$ ($p = 0.24$), and $r = -0.25$ ($p = 0.01$), respectively. Despite the low correlation with the PDO, multi-year periods of high SSS_{10}/low rain generally correspond to negative PDO phases (Figure 2.4a,c). Scatter plots confirm that while the linear correlations between SSS_{10} and indices of the PDO (Figure 2.6a) and ENSO (Figure 2.6b) are weak, there is a strong tendency for high SSS_{10}/low rain winter seasons during negative values of both indices (Cayan et al., 1998; Shukla et al., 2015; Gershunov, Barnett, 1998; Gershunov, Cayan, 2003). The case for the PDO is slightly less obvious for annual values, but with a 5-year smoothing to emphasize decadal polarity changes, the relationship is tighter (Figure 2.6a).

JFM ENSO state provides a stronger constraint on year-to-year drought conditions than the PDO, with only one low SSS_{10} winter (in 1918) evident when the ENSO index dips below -0.2, and none during strong La Niña events when the JFM-averaged index falls below -1.0 (Figure 2.6b). Thus, La Niña-like conditions strongly favor below-average rain levels for any given winter (Gershunov, Barnett, 1998), whereas multi-year drought periods tend to fall within prolonged negative PDO phases. In contrast, wet winters occur during positive PDO and ENSO phases (Gershunov, Barnett, 1998), but not consistently so as high SSS_{10}/dry winters are just as likely, and high index values do not ensure low SSS_{10} levels (Figure 2.6a,b). The wettest/lowest SSS_{10} winters almost exclusively occur during El Niño years, but not every El Niño resulted in a wet year. Low SSS_{10}/wet winters ($SSS_{10} < -0.35$) occurred during 17.1% (12.8%) of positive PDO (El Niño) years, but only 1.6% (3.5%) of negative PDO (La Niña) winters. High SSS_{10}/dry winters ($SSS_{10} > -0.20$) happened in 73.2% (76.6%) of positive PDO (El Niño) years and in 91.9% (91.4%) of negative PDO (La Niña) winters.

A recent study (Liu et al., 2018) notes that the Tropical Northern Hemisphere pattern (TNH; Mo, Livezey, 1986) is highly correlated with California precipitation variability, and suggests that a combination of ENSO and TNH indices (as opposed to ENSO alone) provides improved predictability of precipitation. TNH is a prominent winter

climate mode that reflects large-scale changes in the extent and location of the Pacific jet stream (Mo, Livezey, 1986). Dry/wet years in southern California tend to occur during TNH positive/negative phases. A strong negative 500-hPa geopotential height anomaly is seen at TNH negative phases over the NE Pacific Ocean, and vice versa for positive phases (Barnston, Livezey, 1987). Negative phase TNH conditions support cloud formation and precipitation whereas positive phase TNH conditions reduce the winter storm landfalling probability in California (Liu et al., 2018). A scatter plot of SSS_{10} versus the NINO3.4 and TNH indices confirms these tendencies, with low SSS_{10} wet winters clustered primarily in the lower right-hand quadrant of Figure 2.6c where El Niño and negative TNH conditions meet.

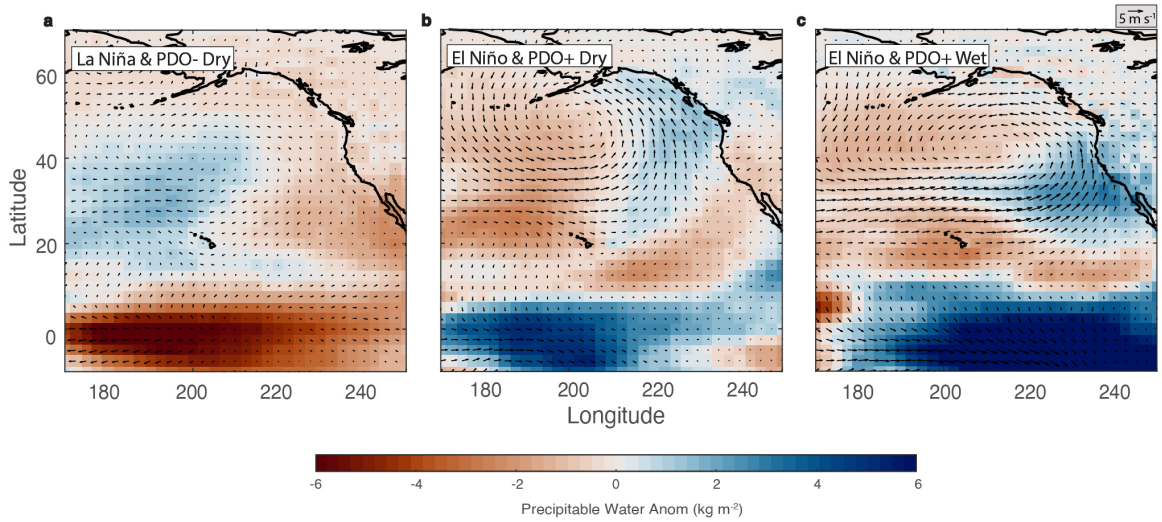


Figure 2.7. Composite atmospheric conditions for three combinations of climate modes and SSS_{10} wet vs. dry winter groupings. Composites of JFM-averaged anomalies of NCEP surface winds and precipitable water (1981-2021) for a) La Niña & PDO negative phases with high SSS_{10}/dry winters (n=13 yrs), b) El Niño & PDO positive phases with high SSS_{10}/dry winters (n=6 yrs), and c) El Niño & PDO positive phases with low SSS_{10}/wet winters (n=4 yrs).

Composites of JFM-averaged surface wind and precipitable water anomalies illustrate the relationship between climate phase and southern California precipitation.

During La Niña and negative PDO phases (Figure 2.7a), the Aleutian low pressure system over the northeast Pacific weakens (clockwise wind anomaly) with negative precipitable water anomalies and average wind conditions over the western US. During El Niño and positive PDO phase wet years (Figure 2.7c), the Aleutian low strengthens and deepens (anticlockwise wind anomaly) forcing the Northern Hemisphere Jetstream (NHJ) southward, resulting in increased storm landfalls on the US west coast and significant positive precipitable water anomalies (Li et al., 2016; Raphael, Mills, 1996). During El Niño and positive PDO phase dry years (Figure 2.7b), the southeastern extent of the NHJ is located more northwest when compared to rainy year conditions (Figure 2.7c), pushing storm landfalls north and causing negligible to negative precipitable water anomalies in the southern California region.

2.2.3 Implications

The long-running salinity record from Scripps Pier reflects regional winter precipitation and streamflow patterns influenced by both the PDO and ENSO. Over the past 70 years, the majority of low SSS_{10}/wet winters have occurred during positive PDO phases, and more specifically when the NINO3.4 and TNH indices are positive and negative, respectively. The SSS_{10} time series especially highlights the occurrences of multi-year drought conditions over the past century. In particular, during the prolonged negative PDO phase between 1944-1977, SSS_{10} was persistently near normal (Figure 2.4b), indicating a lack of heavy winter rain events.

The SSS_{10} observations suggest that a freshwater signal in the coastal surface ocean that persists for multiple days requires a major rain event or a few smaller rain events that result in substantial streamflow and runoff when averaged over the JFM season. Large impact rain events can come in the form of atmospheric rivers (ARs). AR events in the southern California region occur over a few days each year and can contribute up to half of the annual precipitation accumulation (Gershunov et al., 2017). Based on

the AR Rank database, the 1978 to 1999 positive PDO phase featured 50% more days with winter AR events in the southern California region compared to the 1944 to 1977 negative PDO phase ($12 \pm 1.3\%$ to $8 \pm 1.1\%$ respectively). AR events previously have been shown to contribute more to the total water year precipitation during PDO+ and El Niño years in southern California (Dettinger et al., 2011; Gershunov et al., 2017) when compared to other years. In general, we find that mean JFM precipitation provides a better correspondence with SSS_{10} than time series based on AR Rank, as expected, due to ARs providing only some of the precipitation to the region. This implies that not all ARs lead to wet winters, as measured by the coastal ocean's SSS response, and the sources of precipitation that lead to low SSS_{10} winters are variable.

As the climate changes, current projections are uncertain regarding how the climate modes influencing the southern California region will be impacted (Pörtner et al., 2022). The IPCC WGII Sixth Assessment Report (Pörtner et al., 2022) states with moderate confidence that extreme El Niño and La Niña events may become more frequent, up to twice as often, with increased teleconnection responses over the remainder of this century. This would have a direct impact on the severity of dry winters and of the unpredictable wet winters in southern California. A consensus on future PDO conditions under climate change has not been reached (Pörtner et al., 2022). The US west coast may experience a decrease in the frequency of non-AR related rain but an increase in extreme rain due to ARs specifically (Gershunov et al., 2019).

The ocean salinity time series at Scripps Pier complements information provided by nearby streamflow data and reinforces the detection of interannual and decadal winter rainfall variations apparent in rain gauge data. The salinity record also provides a long-term context for assessing the impacts of extreme precipitation events on the coastal zone, even in a region of low total freshwater input, which has impacts on coastal pollution, sediment, nutrient delivery, and beyond. Results here provide a more nuanced view of the value of the coastal salinity record, in that event scale structure in the form of low SSS

pulses (or lack of these) provides a gauge of the vital heavy precipitation events that dictate the status of precipitation and water resources in the southern California coastal region. Together the measurements highlight the strong influence that Pacific climate modes have on regional precipitation and coastal hydrography. The 105-year length of this salinity record provides a unique opportunity to isolate these decadal patterns in precipitation as it scales with the coastal ocean response to these events. Our findings show that salinity can be used to investigate the strong role that interannual to multi-decadal variation plays in driving hydroclimate conditions in this region – multi-decadal periods of relatively dry winters are common for the region and relief from drought periods may not occur until the PDO shifts to a positive state. From revealing climate signals not shown in salinity data previously, to bolstering proof that precipitation and resulting advection of streamflow waters are the leading causes in coastal ocean freshening events, the implications for this study increase the breadth of surface salinity records beyond the uses by oceanographers alone.

2.3 Methods and Data

2.3.1 Salinity Data

Since 1916, daily water samples have been collected at the end of the Scripps Institution of Oceanography (SIO) pier in La Jolla, CA. For the near-surface samples, salinity has been measured with two consistent methodologies over time, initially by titration (1916-1964) and now by inductive salinometer (1965-present). The current collection and measurement procedures are described in the Shore Stations Program Annual Reports (https://shorestations.ucsd.edu/). Here we analyze the year-to-year wet season variability using the daily sea surface salinity (SSS) record spanning 1916 to 2021 for a total of 38,330 days of data. We also examine similar daily salinity measurements collected at the Newport Beach Pier following the same methodology. Time series from

both stations are part of the Shore Stations Program (Carter et al., 2022).

2.3.2 Precipitation and Streamflow

Daily and monthly precipitation accumulation data (1939-2021) for the San Diego International Airport (∼16 km southeast of the Pier) were obtained from the National Oceanic and Atmospheric Administration's National Center for Environmental Information (NOAA NCEI). The Livneh daily near-surface gridded precipitation data (Livneh et al., 2013) (1915-2011) spans the continental US in 1/16 degree resolution and is provided by the Physical Sciences Laboratory (PSL), NOAA.

Daily streamflow time series from Los Peñasquitos, the closest major stream to Scripps Pier, is obtained from the U.S. Geological Survey (1965-2021). The stream feeds into Los Peñasquitos Lagoon, which discharges into the ocean ∼7.5 km north of the Scripps pier. Anomalies for Los Peñasquitos outflow and monthly precipitation accumulation are the JFM averages with JFM mean climatologies removed.

An Atmospheric River rank system categorizes the magnitude of landfalling ARs based on the maximum instantaneous vertically integrated water vapor transport (IVT) and storm duration (Ralph et al., 2019). This work utilizes a retrospective analysis project produced daily AR Rank dataset (1948 to 2020) for consideration of JFM AR events (Gershunov et al., 2017).

2.3.3 Climate Indices and Atmospheric Variables

El Niño-Southern Oscillation (ENSO) variability is characterized using the NINO3.4 SST index (1870 to present), obtained from the PSL, NOAA. NINO3.4 is calculated from the HadISST1's SST averaged between 5°S-5°N and 170-120°W (Rayner et al., 2003).

The Pacific Decadal Oscillation index (1854 to present), obtained from NOAA NCEI, is computed using the ERSST Version 5 extended reconstruction of sea surface temperature (Huang et al., 2017). The PDO index is smoothed using a convolution filter

with a 5-year Blackman window (Oppenheim, 1999) to emphasize decadal variability.

The Tropical/ Northern Hemisphere pattern (Mo, Livezey, 1986) (TNH, 1950 to present) index was provided by the NOAA NCEP Climate Prediction Center (CPC) and accessed through Columbia University International Research for Climate and Society Institute's Climate Data Library. The TNH index is provided by the CPC with only December through February values.

For atmospheric composites (Figure 2.7), surface wind (1948 to present) and precipitable water data (1981 to present) were obtained from NCEP/ NCAR Reanalysis 1 (Kalnay et al., 1996) and NCEP Daily Global Analyses, respectively. NOAA PSL provided access to both NCEP datasets. Precipitable water content over a given area denotes humidity, which is positively correlated to rainfall (Muller et al., 2009).

All climate indices are averaged over the rainy season (JFM), with the exception of TNH which is DJF averaged, and all are referred to without mention of this averaging for the sake of brevity. For all correlations, significance is determined by a p-value < 0.05, assuming every data point is independent unless otherwise specified.

2.4 Acknowledgments

Chapter 2, in full, is a reprint of the material as it appears in *Communications Earth & Environment*: Byrne, S.M., Merrifield, M.A., Carter, M.L., Cayan, D.R., Flick, R.E., Gershunov, A., and Giddings, S.N. (2023). Southern California winter precipitation variability reflected in 100-year ocean salinity record. *Commun Earth Environ* 4, 137. https://doi.org/10.1038/s43247-023-00803-8. The dissertation author was the primary investigator and author of this paper.

2.5 Supplementary Information

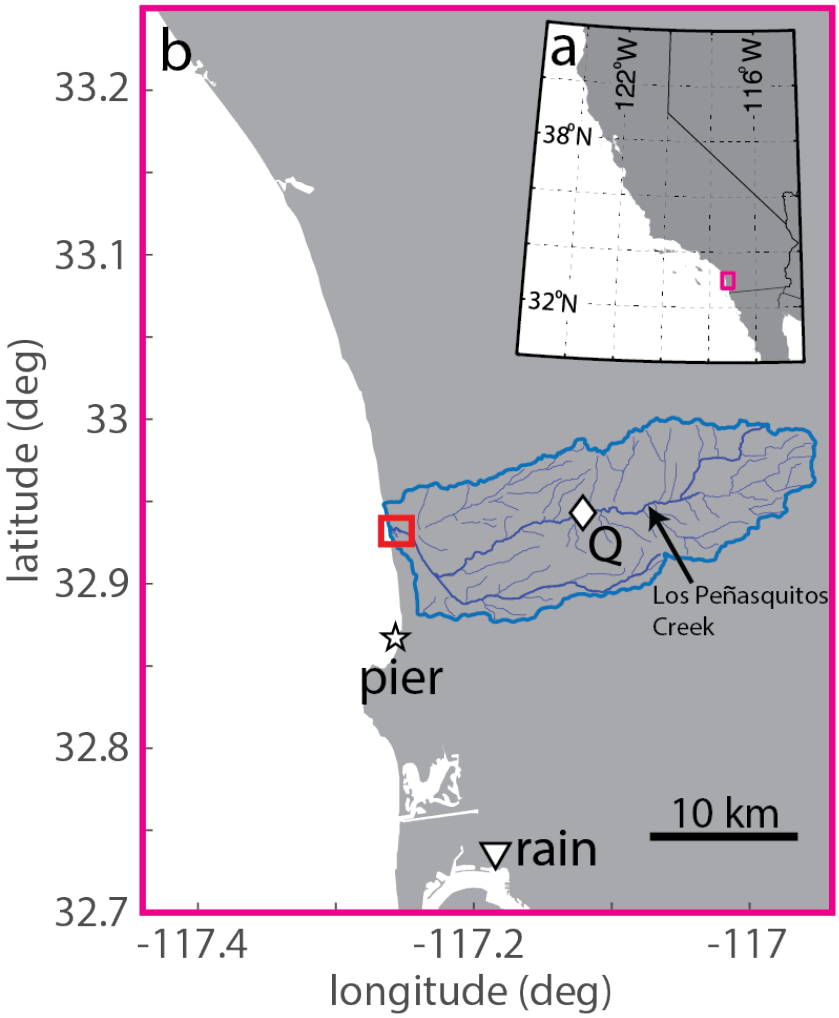


Figure 2.8. Map of the study region that includes where the data is recorded: salinity record (at 'pier', marked with a star), Los Peñasquitos streamflow (at 'Q', marked with a diamond), and precipitation (at 'rain', marked with a triangle). The small red box denotes where Los Peñasquitos connects with the ocean and the blue lines depict the watershed that drains into Los Peñasquitos. Panel a. shows the greater California region with a pink box around study site and panel b. is the zoomed in view of the pink box that shows the data collection locations.

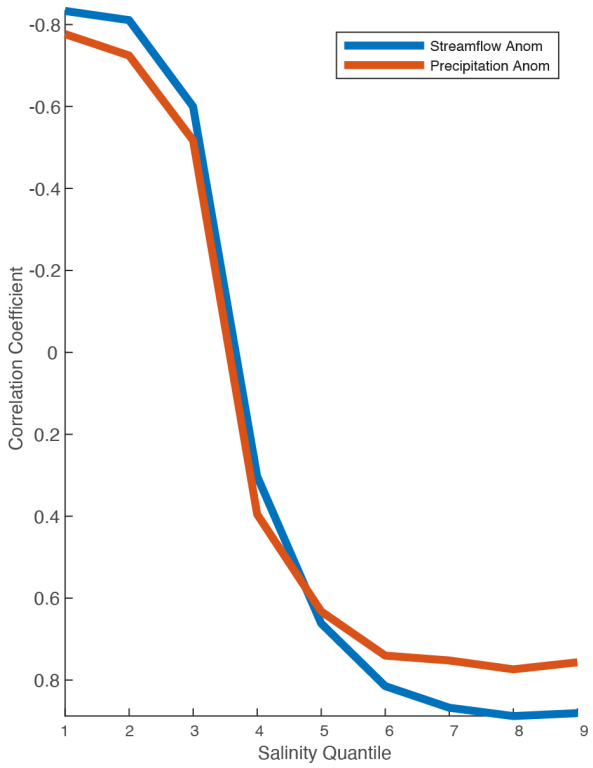


Figure 2.9. Correlations of winter salinity anomaly quantiles with streamflow and precipitation anomalies. Correlation coefficients of streamflow anomaly (blue) and precipitation (orange) to each quantile of January–March (JFM) salinity anomaly. Note the strongest correlations in both cases is to the freshest quantile of salinity, and the weakest to the saltiest. First, an array of JFM anomaly salinity values for every year is arranged so that the quantiles bin the daily values from every JFM day for each year of the record. This array is then put into 9 quantiles that divide the data points into 9 equally sized groups in order from lowest to highest values for each year, where quantile 5 would contain the 50% or median SSS values. Next, a correlation between each year of sea surface salinity anomaly quantiles (SSS_a) with each year of the streamflow anomaly (one value JFM-averaged per year) and with the precipitation anomaly (one-value JFM-averaged per year) provides a correlation coefficient for how the time series line-up for each SSS_a quantile. This figure demonstrates what one may expect, the salinity anomaly quantile with the freshest values correlating most closely with the rain and streamflow data, the median/mean values having low correlation, and the highest salinity quantiles correlating strongly inverse. With this study's focus on salinity's connection to precipitation we chose the quantile with the strongest positive correlation (the 10% quantile) to continue our analysis.

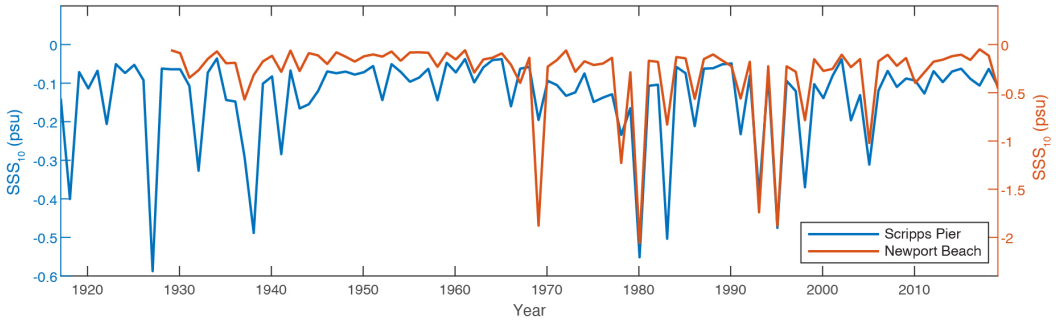


Figure 2.10. Winter SSS_{10} timeseries at Scripps Pier and Newport Beach. The JFM salinity anomaly from Newport Beach pier shows a similar pattern to that seen at Scripps Pier. This data validates the Scripps Pier record findings, and suggests that the La Jolla record likely reflects precipitation levels over a broader southern California coastal region. This figure is included to emphasize the robustness in the salinity signals we see, where most major rain events causing these features are widespread enough to impact the greater southern California region.

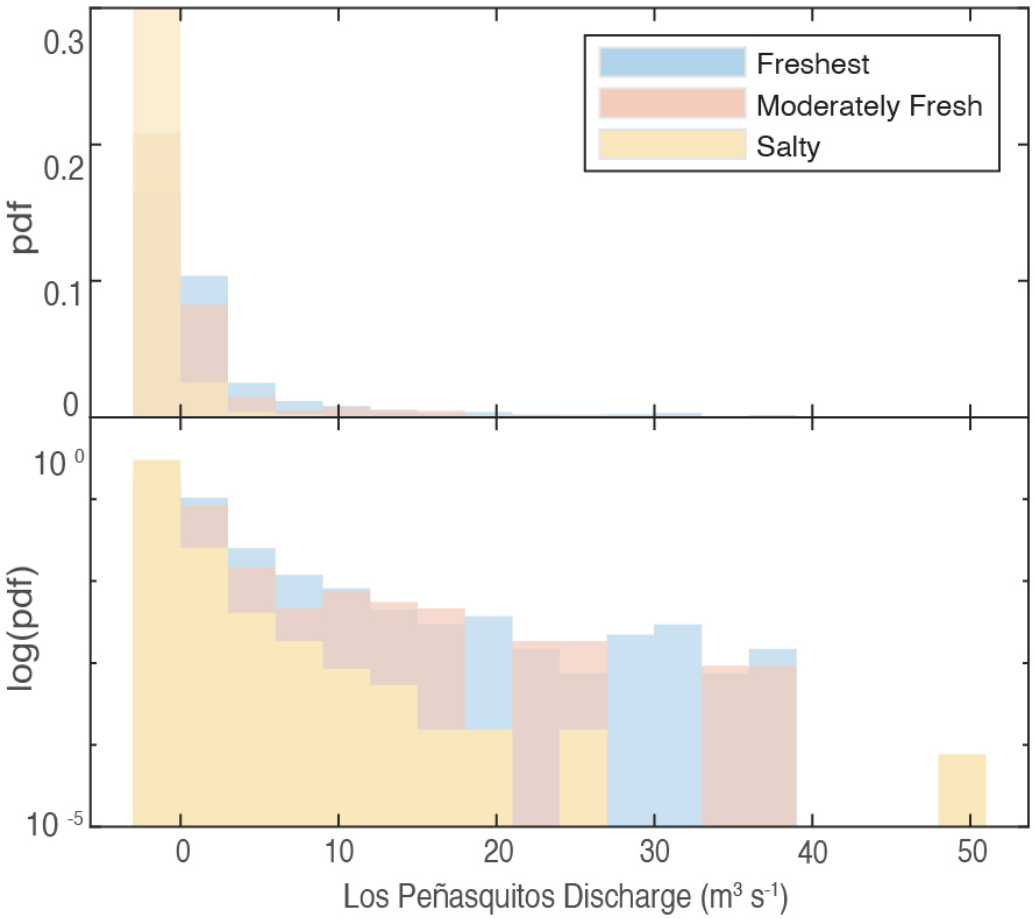


Figure 2.11. Probability density function of streamflow in salty to fresh SSS_{10} years. Probability density function histogram of JFM Los Peñasquitos streamflow daily anomaly divided up by fresh years (blue; $SSS_{10} < -0.35$ psu; n = 5 years/ 451 days), moderately fresh years (pink; -0.35 psu $< SSS_{10} < -0.2$ psu; n = 4 yrs/ 360 days), and salty years (yellow; $SSS_{10} > -0.2$ psu; n = 48 yrs/ 4333 days) between 1965 to 2021. These fresh, moderately fresh, and salty years are a way of visualizing what streamflow properties may cause an SSS_{10} value that is large, medium, or close to zero, respectively. These divisions occur at SSS_{10} values that were selected because of the expected frequency of each level of events, and this figure verifies that streamflow magnitudes support these groupings. The figure is included as a supplement to highlight that the probability is low for high flow events to occur, and when they do, the SSS_{10} will drop in response and therefore fall in the moderately fresh, or the freshest salinity groupings. The binning algorithm is Sturges' rule applied to optimize the number of groups the data is split into, to make visual comparison easiest. Evenly scaled y-axis on top and log scaled y-axis on bottom illustrate overall trend and the extreme tail respectively.

Chapter 3

Processes impacting the fate of small river plumes following storms

3.1 Introduction

Freshwater discharge to the coastal ocean from land serves an important role in both hydrological and biogeochemical cycles (Syed et al., 2010). The interaction of freshwater and ocean water forms horizontally advecting river plumes (Ryther et al., 1967; Wright, Coleman, 1971; Boicourt, 1973; Garvine, 1974). Freshwater river plumes (hereafter referred to as plumes) can contain a host of nutrients, larvae, land-based particles, sediment, debris, and pollutants (Reeves et al., 2004; Milliman, Farnsworth, 2013; Aguilera et al., 2019). Thus, understanding plume behavior is critical for assessing health impacts to beachgoers and coastal ecosystems.

The dynamics that drive river plumes differ depending on the size of the system. Plumes may be defined as large or small based on a number of definitions. For example, plumes can be considered small if they: have low incoming river discharge (e.g., from low inflow estuaries; Largier, 2023), can stop formation during flood tides, are not impacted by the Earth's rotation (Cole, Hetland, 2016; Garvine, 1995), or are impacted by the surf zone (Wong et al., 2013; Rodriguez et al., 2018). In this study, we explore a small plume that fits all of the above definitions. Small plumes can originate from smaller watersheds and/or regions with less rainfall or meltwater input and hence lower streamflow input (Warrick,

Fong, 2004; Largier, 2023). While many studies focus on large plume systems, small plume systems are more numerous, can collectively impact a greater cumulative ocean area when measured against a single large river of comparable watershed size (Warrick, Fong, 2004; Mazzini et al., 2014), and can significantly influence coastal ocean biogeochemistry (Wetz et al., 2006).

3.1.1 Large vs. Small Plume Dynamical Regions

Large plumes have dynamical regions defined by their physical drivers, but it is unclear how these established regions translate to small plumes. The four regions used to describe plumes are: the source region, near-field, mid-field, and far-field (Garvine, 1984; Hetland, 2005; Horner-Devine et al., 2009, 2015).

The source region is where estuarine processes set plume properties at the river mouth (Nash et al., 2009). In many large plumes, this source region is often continuously active, always forming plumes (Garvine, 1984; Hickey et al., 1998; Horner-Devine et al., 2009). In small systems with moderate to large tides, outflow can emerge during ebb tide and cease on flood tide or when the estuary mouth is closed due to morphodynamic processes (Pritchard, Huntley, 2006; Williams, Stacey, 2016; Orescanin, Scooler, 2018; Harvey et al., 2023). Small plume systems such as those in low-inflow Mediterranean climates can experience episodic precipitation that dramatically increases discharge over a very short period (e.g., from 1 to 100 m^3/s over a day), generating plumes greater in freshwater volume than an ebb tidally-pulsed one, but still very small compared to those of large plume systems (Warrick et al., 2007; Rosa et al., 2022; Rojas et al., 2023; Collins, Macdonald, 2025). No previous studies have explicitly explored the connection of these processes to the formation conditions of small plumes in the source region.

After the source region is the near-field, where a plume initially expands and river momentum dominates over buoyancy forcing (Hetland, 2005; Horner-Devine et al., 2015). The near-field ends where frictional processes decelerate the outflowing water sufficiently

that buoyancy takes over as the dominant driver of plume dynamics. The location of this transition sets the scale of the near-field plume (Hetland, 2005). Near-field dynamics are fundamentally altered for small plumes that directly interact with the surf zone, where mixing and momentum imparted by wave-breaking become leading order processes and plumes can become surf zone trapped (Wong et al., 2013; Rodriguez et al., 2018; Kastner et al., 2018, 2019; Spydell et al., 2019; Lou et al., 2025). While some dynamic region definitions are easy to translate to small plumes, a gap exists in the classification of surf zone advected plumes, as they do not belong to any of the defined regions.

The mid-field is the transition zone between the near- and far-field. In large systems, this is where Earth's rotation can start impacting plume transport (Garvine, 1987). In small systems, buoyancy and wind have been shown to drive mid-field transport (Basdurak, Largier, 2022). The last dynamic region is the far-field, defined by its lack of river momentum. In large systems far-field dynamics are typically dominated by rotation, wind, and buoyancy (Lemagie, Lerczak, 2020). Leading balances in a large plume's far-field often involve rotation, e.g. Ekman wind and geostrophic balances (Fong et al., 1997; Geyer et al., 2000; Fong, Geyer, 2001; Toublanc et al., 2023; Yankovsky, Yankovsky, 2024), while small plumes experience negligible rotational effects (Garvine, 1995; Warrick et al., 2007; Basdurak et al., 2020). Instead, small plumes have been shown to have a far-field dominated by direct wind forcing and advection (Piñones et al., 2005; Warrick et al., 2007; Kniskern et al., 2011; Osadchiev et al., 2021; Romero et al., 2016; Basdurak, Largier, 2022; Lemos et al., 2022; Vundavilli et al., 2024).

3.1.2 Dynamics Influencing Small Plumes

Waves and surf zone processes can impact a small plume in a variety of ways. We use the term 'surf zone field (SZ-field)' to highlight the dynamical plume regime where distinct processes impact surf zone plume transport that do not fit within the definitions of near-, mid-, or far-field regions. The SZ-field is influenced by wave-driven

dynamics including radiation stresses, Stokes drift, and vertical mixing caused by wave injection of turbulent kinetic energy (TKE) (Thornton, Guza, 1983, 1986; Feddersen et al., 1998; Feddersen, Trowbridge, 2005; Feddersen, 2012; Hally-Rosendahl et al., 2014; Kumar, Feddersen, 2017; Spydell et al., 2019; Kastner et al., 2023). The cross-shore (x-direction) gradient of the normal component of wave radiation stress ($\frac{\partial S_{xx}}{\partial x}$) can counter a plume's river flux in the near-field and, if strong enough, contribute to retention (trapping) inside the surf zone and create a SZ-field (Wong et al., 2013; Rodriguez et al., 2018; Kastner et al., 2019; Lou et al., 2025). Stokes drift can contribute to the retention of a surface plume feature in the cross-shore (Lentz, Fewings, 2012; Kumar, Feddersen, 2017). Infragravity waves have also been shown to modulate small plumes (Flores et al., 2022; Roco et al., 2024). The cross-shore gradient of the shear component of wave radiation stress ($\frac{\partial S_{xy}}{\partial x}$) can drive an alongshore (y-direction) current within the surf zone (v_{SZ}; Bowen, 1969; Longuet-Higgins, 1970) that transports plumes with a direction depending on the local wave incidence angle (Rodriguez et al., 2018; Kastner et al., 2019; Baldoni et al., 2022; Brasseale et al., 2023) and channel angle (Wong et al., 2013). Convergence in surf zone currents alongshore can create transient rip currents that export surf zone waters offshore. The surf zone can also have bathymetric rip currents due to bottom features that channel water to the inner-shelf (Hally-Rosendahl et al., 2015; Moulton et al., 2017; Grimes et al., 2020). These, among other surf zone to inner-shelf exchange mechanisms, can force some or all of a SZ-field plume to exit to the inner-shelf and the far-field. If a plume is polluted, an understanding of the formation and persistence of the SZ-field will inform the extent of health risks to beachgoers (Wong et al., 2013; Feddersen et al., 2021; Brasseale et al., 2023). As previous studies focus on near-mouth surf zone freshwater plume impacts, there is a need to understand the role of the SZ-field on the fate of small plumes.

Wind is shown in both models and in observations to influence small plume transport in the far-field (Piñones et al., 2005; Warrick et al., 2007; Kniskern et al., 2011; Osadchiev et al., 2021; Romero et al., 2016; Baldoni et al., 2022; Basdurak, Largier, 2022; Lemos

et al., 2022; Vundavilli et al., 2024; Speiser, Largier, 2024). Wind advects small plumes in the alongshore direction through the direct stress in the alongshore direction imparted at the air-sea boundary. Cross-shore winds can also directly influence the cross-shore plume extent (Romero et al., 2016). At times with relatively strong winds, even mid- to large plumes can have an alongshore momentum balance dominated by alongshore wind stress (Hickey et al., 1998; Kakoulaki et al., 2014). Surface-advected plumes respond relatively quickly to dynamically changing wind conditions, like the quasi-rotational Maipo River plume in Chile responding to diurnal wind variability with a 7 hour lag (Piñones et al., 2005). Additionally, for a small system in the non-tidal Black Sea, a study shows plume speeds respond linearly to changing wind speeds within 10-20 minutes (Osadchiev et al., 2021). In our study region of southern California, small plumes following rain events show far-field transport in the direction of wind forcing (Warrick et al., 2007; Kniskern et al., 2011; Romero et al., 2016). Winds that accompany cyclonic storms in this region typically blow northward before the precipitation, and then southward near the time of peak discharge and for many hours following (Warrick et al., 2007; Kniskern et al., 2011). Therefore, far-field transport of small plumes is expected to be southward in the alongshore direction resulting from southward alongshore wind forcing at and after peak discharge in the study region (Warrick et al., 2007). While wind and advection have previously been shown to dominate in the far-field, no studies have considered the combined influences of wind, buoyancy, and wave processes on the far-field.

3.1.3 Outline

In this paper, we explain how freshwater from small plumes transports through the surf zone to the inner-shelf and far-field. The aims of this study are: to inform the time-dependent formation of small plumes; assess the combined roles of wind, buoyancy, and surf zone processes on far-field plume transport; and present a conceptual framework that outlines the dynamic regions a small plume possesses under varying environmental

conditions.

We use observations collected in Los Peñasquitos Lagoon and across a $\sim$ 10-km alongshore stretch of the inner-shelf. The experiment study site and methodology are described in Section 3.2 along with the details of data collection, processing, and quality control. Three months of observations are presented and summarized in Section 3.3. Next, in Section 3.4 we explore source region plume formation by introducing a dimensionless parameter that distinguishes between two formation regimes. Then in Section 3.5, the plumes resulting from the three largest storm events are each explored in detail. First, the general plume behaviors and conditions are explained (Section 3.5.1), then the relative contributions of the surf zone, wind, and buoyancy processes are detailed in Sections 3.5.2, 3.5.3, and 3.5.4 respectively. Generalized conceptual takeaways for small plume transport are outlined in Section 3.6.1. The results are then discussed in the context of their: applicability to ebb tide plumes (3.6.2), connection to a surf zone trapping parameter space (3.6.2), and implications for plume mixing (3.6.3). Conclusions are given in section 3.7.

3.2 Data and Methods

3.2.1 Study Region

In this study we focus on Los Peñasquitos Lagoon (hereafter referred to as LPL), a small plume system located in San Diego, California (Figure 3.1). This system can be described as a low-inflow estuary (LIE) (Largier, 2023), a bar-built estuary with a constricted mouth, and an intermittently closed estuary (ICE) (Williams, Stacey, 2016; McSweeney et al., 2017; Harvey et al., 2023). Los Peñasquitos serves as an example for the numerous estuaries that have similar classifications and dynamics across the globe (Largier, 2023; McSweeney et al., 2017). LIEs in Mediterranean climates have highly variable and infrequent rainfall (Dettinger et al., 2011), often experiencing atmospheric rivers (Gershunov et al., 2019). Southern California precipitation totals vary greatly year-to-year

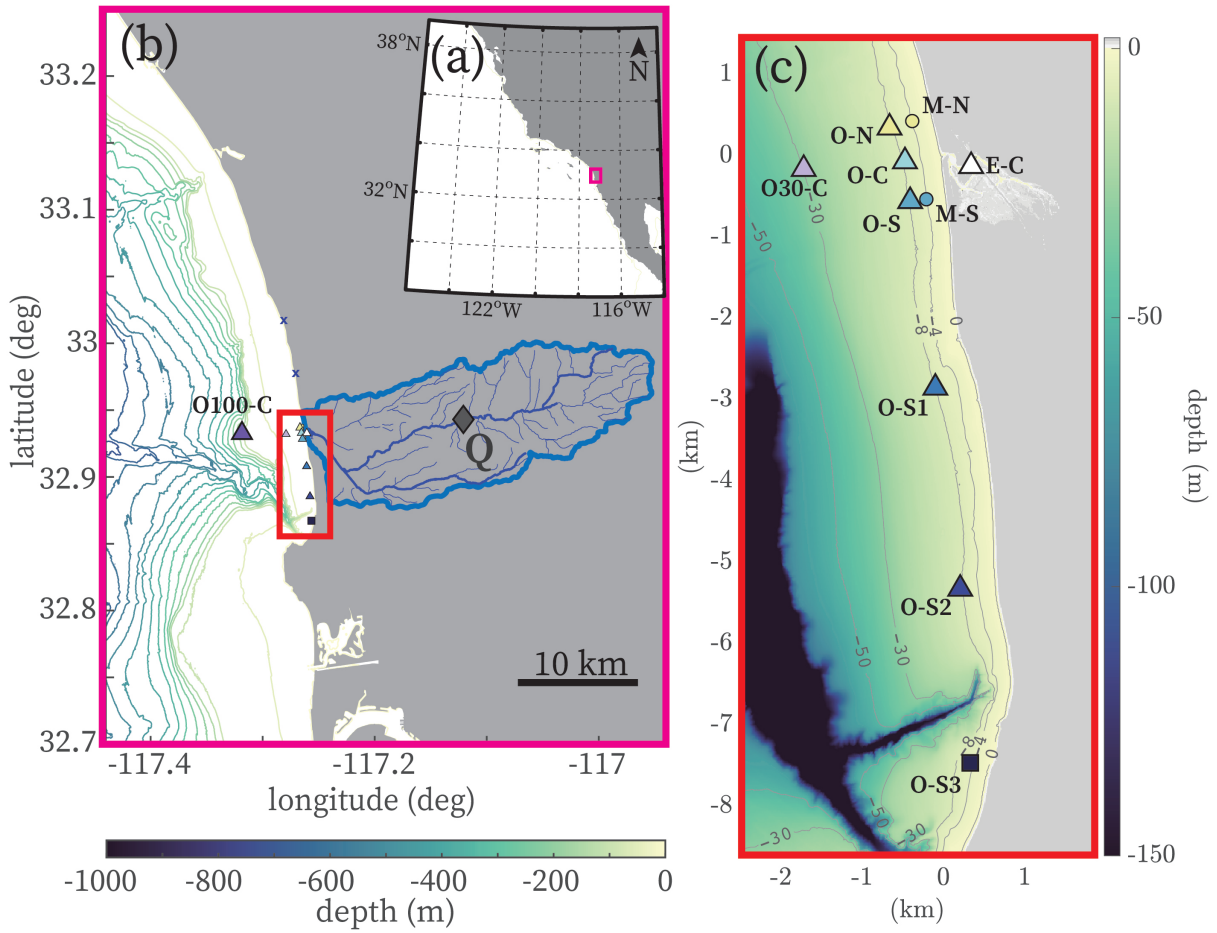


Figure 3.1. (a) U.S. west coast. (b) River watershed, contoured bathymetry, and moorings. 'Q' (diamond) is the USGS gauge where Q_{river} is recorded and O100-C is a mooring maintained by the Ocean Time Series Group. 'x' denotes two northern river mouths. (c) Zoom in of red box in (b) showing moorings deployed during study period on the bathymetry (shading and gray contours). Moorings are colored darker blue to the south, yellow to the north, darker purple going offshore along the mouth centerline, and white inside of the estuary. Triangles mark moorings with ADCPs and top/bottom salinity, circles mark moorings with ADCPs and bottom salinity, and the square marks the Scripps Pier with mid-water column salinity only.

and depend on climate oscillations like El Niño Southern Oscillation and Pacific Decadal Oscillation (Ropelewski, Halpert, 1986; Gershunov, Barnett, 1998; Cayan et al., 1999). As a result, the occurrence and far-field transport of rainfall-enhanced plumes also varies with these climate oscillations (Byrne et al., 2023).

The study region's coastline is oriented nearly north-south, with an average shore-normal angle of 262° true north. The bathymetry is largely alongshore uniform except for a submarine canyon located 6.5km south of LPL's mouth. The canyon could indirectly influence the propagation of a surface-advected river plume by modulation of the currents near the canyon head, though these effects are not expected to change the results of this study.

LIEs adjacent to LPL exist 4.6-km and 9.3-km to the north (San Dieguito and San Elijo Lagoons) and 22-km to the south (Mission Bay). It is common for small plumes from multiple rivers to coalesce (Arnau et al., 2004; Warrick, Farnsworth, 2017) which impacts the total freshwater budget of a region and can modify plume patterns and extent (Mazzini et al., 2014; Osadchiev et al., 2020; Salcedo-Castro et al., 2020; Rojas et al., 2023; Collins, Macdonald, 2025). The freshwater plume(s) explored in this study during certain conditions, is likely the result of not just LPL outflow, but with contributions from adjacent LIEs. Plume coalescence in the study region is most likely to occur with plumes from the two closest sources, San Dieguito Lagoon (SDL) and San Elijo Lagoon (SEL) (shown with 'x' marks in Figure 3.1b) when southward currents are present. The watersheds of SDL and SEL combined represent effectively 1.4x the area of LPL, thus it is unlikely that they represent the primary source of freshwater offshore of LPL, but it is reasonable that they contribute some freshwater to the region.

3.2.2 Observations

Observations were collected as part of the NSF-funded Plumes in Nearshore Conditions (PiNC) experiment focused on tracking plumes exiting LPL, which included

longer-term moorings, and dye tracer studies. For the three intensive dye release days, there were a host of short-term in-situ and remote measurements taken that are not detailed or used in this work. Rather, here we focus on the longer-term experimental components. Instruments deployed over the winter (see Figure 3.1c) included five moorings at the 8-m isobath (O), two moorings at the 4-m isobath (M), one mooring inside the estuary (E-C), and one mooring at the 30-m isobath offshore of the mouth (O30-C). Moorings measured surface and bottom salinity and temperature (using CTDs, conductivity temperature depth sensors), and vertical velocity profiles (using ADCPs, acoustic Doppler current profilers). The 'O-' and 'O30-' moorings were deployed from Dec 12, 2022- Feb 21, 2023. The 4-m depth moorings (M-N and M-S) were deployed for 1 month (Jan 09 - Feb 09, 2023) and had an ADCP and bottom CTD. Additional near-surface salinity measurements were used from the Scripps Pier at a depth of ∼5-m as part of the Automated Shore Stations Program (https://data.caloos.org/#metadata/120738/station/data, mooring O-S3) and at the surface of the Del Mar Mooring in 100-m water depth (operated by the Ocean Time-Series Group, http://mooring.ucsd.edu/delmar1/, mooring O100-C).

The mooring naming convention (Figure 3.1) is as follows: 'O-', 'M-', and 'E-' denote ocean inner-shelf, mid-depth (near and sometimes within the surf zone), and estuary moorings respectively. '-C' is centered on the estuary's mouth. 'O-' are all near the 8-m isobath, whereas O30 and O100 are deeper, at 30- and 100-m water depth respectively, where O100 is the Del Mar mooring. '-N' is north of the estuary, '-S' is south, with each number '-S1', '-S2', etc. representing how many additional moorings away from the estuary centerline it is. O-N and M-N (O-S and M-S) are ∼ 500-m north (south) of LPL's mouth. The Scripps Pier is referred to as 'O-S3'.

3.2.3 Data Processing

Velocity time series are rotated to be alongshore (v) and cross-shore (u) with respect to the shoreline angle, low-pass filtered by convolving with a 30 minute Gaussian, and

sub-sampled at 2 min intervals unless otherwise stated. Individual wave impacts on the velocities are minimized by finding wave troughs, removing the surface layer bias by wave orbital motion above those troughs, and by the aforementioned averaging scheme. Near-surface inner-shelf velocities (v_{IS}) refer to the shallowest velocity bin retained after quality control, which is typically 1-2 m below the instantaneous water surface location. Depth average inner-shelf velocities are represented here as $\bar{v}_{IS}$. The O-C ADCP was buried under sediment from Jan 14-27, causing a data gap. Velocity from the in-estuary ADCP ($\bar{v}_e$) is a temporally (10 minute) and depth-averaged along-channel flow as defined by a principle axes analysis. Salinity (S) outliers are removed via a threshold of $|\frac{dS}{dt}| > 0.5$ psu for CTDs with a $dt = 2$ min and > 15 psu for CTDs with a $dt = 30$ sec. S measurements before and after CTD sensor cleaning inspections are checked and any offset corrected as needed. CTDs sampling at 30 sec are subsampled to 2 min. Freshwater fractions ($F = 1 - \frac{S}{S_0}$) are calculated using instantaneous surface salinity (S) and background salinity ($S_0 = 33.3$ psu) (Nash et al., 2009).

Alongshore surf zone currents are calculated from a balance of alongshore wave forcing to bottom stress (Bowen, 1969; Longuet-Higgins, 1970; Thornton, Guza, 1986) following simplifications discussed in Thornton, Guza (1986) and detailed below. This uses a cross-shore gradient ($\frac{\partial}{\partial x}$) of the shear component of wave radiation stress (S_{xy}) (Longuet-Higgins, Stewart, 1963, 1964). The alongshore bottom stress is simplified by assuming no mean cross-shore flow, the alongshore current (v_{SZ}) is weak compared to the wave orbital velocity (u_o), and the small angle approximation applies. This gives an alongshore bottom stress $\tau_b \approx \rho c_f \frac{2}{\pi} u_o v_{SZ}$ where c_f is a drag coefficient and $u_o = a\sqrt{\frac{g}{h}}$, with g as gravity, a as wave amplitude ($a = \frac{H_s}{\sqrt{8}}$), H_s as significant wave height, and h as water depth. The wave amplitude equation results from $a = \frac{H_{rms}}{2}$, where H_{rms} is root-mean-square wave height, and $H_{rms} = \frac{H_s}{\sqrt{2}}$, such that $a = \frac{H_s}{\sqrt{8}}$. Equating the wave forcing to bottom stress and solving for alongshore velocity gives the following equation

for surf zone currents:

$$v_{SZ} = \frac{-1}{\rho}\frac{\partial S_{xy}}{\partial x}\frac{\pi}{2c_f}\frac{1}{a\sqrt{g/h}} \ . \tag{3.1}$$

We use wave hindcasts from the Coastal Data Information Program (CDIP) wave MOnitoring and Prediction (MOP) system to extract the quantities needed to calculate v_{SZ} (O'Reilly et al., 2016). O'Reilly et al. (2016) calculate $\frac{S_{xy}}{\rho g}$ (with units m^2, hereafter referred to just as S_{xy}) using integrals of the second directional moment of a given incident wave spectrum. The depth of wave breaking (h_{wb}) is calculated from the 9.5-m depth hindcast as $(\frac{H_s c_g^{1/2}}{\gamma g^{1/4}})^{4/5}$ with $\gamma = 0.42$ and wave group speed $c_g = \sqrt{gh}$ (Thornton, Guza, 1982). At each CDIP transect for each timestep a H_s and S_{xy} value are extracted from the depth closest to h_{wb}. The surf zone width (∂x) is computed as the horizontal distance between h_{wb} and the 0.5-m isobath along each transect as determined by CDIP's reference bathymetry. Note the bathymetry is fixed and does not account for changing tides. For v_{SZ}, we assume density is constant, $c_f = 0.003$ (Feddersen et al., 1998), and that the gradient in S_{xy} is constant between the depth of wave breaking and the shoreline. While here v_{SZ} is the surf zone current estiamte near the point of wave breaking, there is cross-shore variability in alongshore surf zone currents (Longuet-Higgins, 1970). This estimate is greater than a mean current, but not necessarily reflective of the maximum current. To estimate v_{SZmax}, the maximum alongshore surf zone current, we invoke an empirical relationship derived for a beach in Santa Barbara, CA from Guza et al. (1986): $v_{SZmax} \approx 64.1 S_{xy}$ with S_{xy} in units of m^2 and velocity in m/s. Surf zone current estimates span from O-N to 700-m south of O-S2; the presence of the canyon head interferes with hindcasts farther south and are neglected in this study. Median S_{xx} values are presented for each case in Section 3.5.2 for comparison of relative wave conditions.

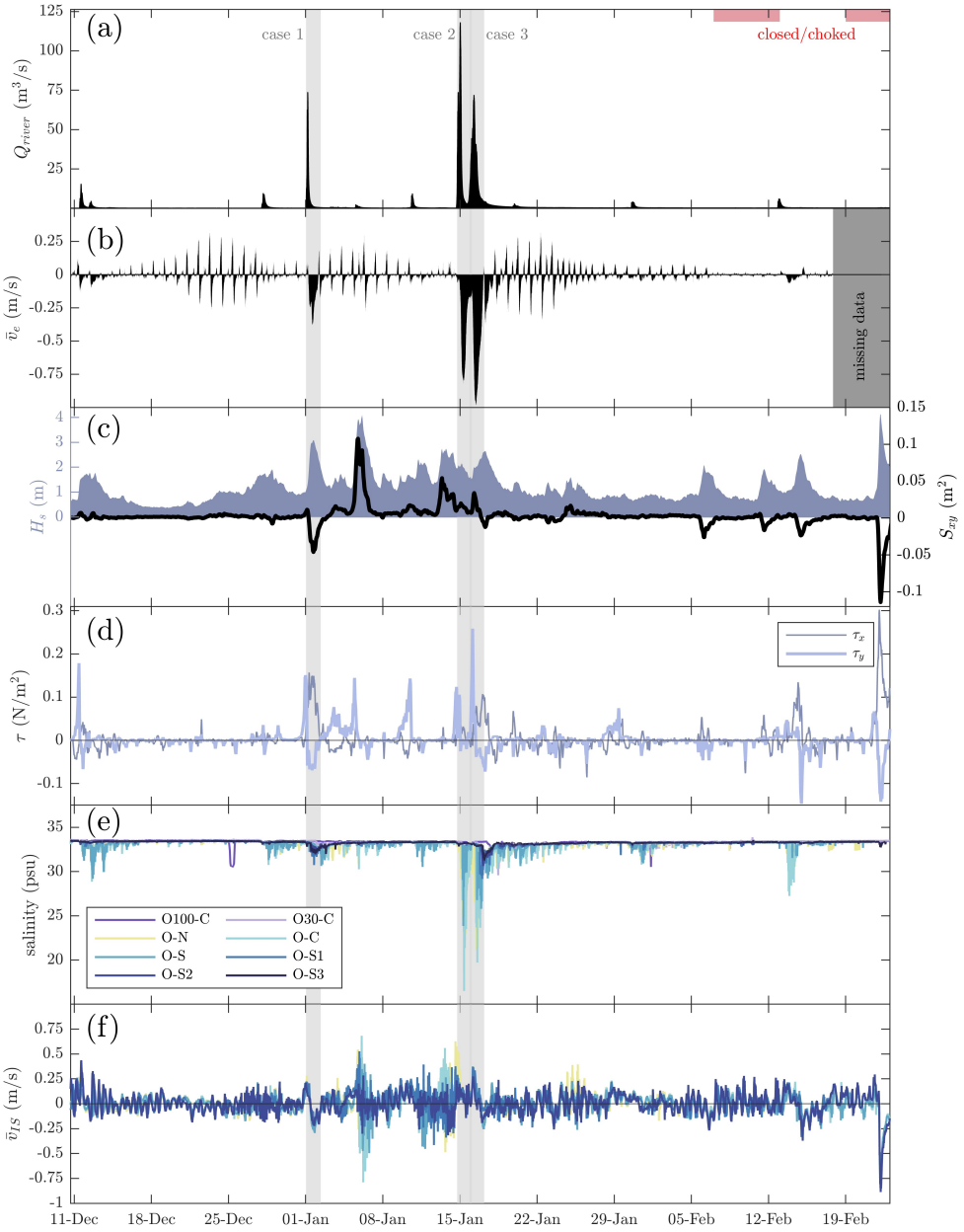


Figure 3.2. (a) Q_{river} from Los Peñasquitos. (b) E-C depth-averaged along-channel velocity $\bar{v}_e$ where positive values indicate flow into the estuary. The dark gray shaded area towards the record end is when the mooring was recovered and has no data. (c) Significant wave height (H_s, shaded) and S_{xy} (line) from CDIP estimates at LPL's mouth. Note that here $S_{xy} > 0$ indicates northward surf zone velocities, v_{sz} (d) Cross-shore (τ_x, dark purple) and alongshore (τ_y, light purple) wind stress. (e) Surface salinity from moorings (colors match the icons on the map in Figure 3.1. (d) Depth-averaged alongshore velocities $\bar{v}_{IS}$ for the 8-m isobath moorings. Cases 1-3 are shaded across panels in light gray and red shaded bars in panel (a) indicate periods of closed or choked estuary mouth conditions.

3.3 General Conditions

Between Dec 01, 2022- Mar 01, 2023, the average river discharge from Los Peñasquitos Creek (Q_{river}, measured upstream of tidal influence) is $\sim$1 m^3/s but occasionally peaks upwards of 50 m^3/s (Figure 3.2a). Q_{river}, as presented throughout this paper, is multiplied by a factor of 1.58 as determined by Elwany (2011) for this watershed to adjust for the ungauged watershed area between the upstream gauge location and where the river reaches the estuary. The estuary velocity ($\bar{v}_e$) measured at mooring E-C is < 0.1 m/s during neap tides, and reaches 0.25 m/s during spring tides (Figure 3.2b). $\bar{v}_e$ reverses consistently on a tidal timescale responding to the mixed semidiurnal tides unless a large rain event occurs or the estuary mouth closes, disconnecting the estuary from the ocean (Figure 3.2b). Large rain events cause $\bar{v}_e$ to exceed tidal velocities on numerous occasions during the three months. The estuary mouth closes on February 6 and $\bar{v}_e$ stagnates. The mouth remains closed or choked (allowing some ocean exchange during large tide or river discharge events) until the end of the study period (Figure 3.2b).

Inner-shelf currents are usually depth-uniform and stronger in v, the alongshore direction. The five 8-m isobath $\bar{v}_{IS}$ records typically range between +/− 0.3 m/s and are coherent (Figure 3.2f). Prominent semidiurnal (period $\sim$12-hr) oscillations are seen across the winter, except a few occasions. The $\sim$12-hr oscillation propagates northward in our mooring array and is not in phase with the surface tide. This could be explained by coastally trapped waves, which have been shown to induce M_2 semidiurnal variability alongshore on the inner-shelf region in Southern California (Okun et al., 2025). High-frequency variability in $\bar{v}_{IS}$ on February 6th is caused by atypically large waves, with up to 4-m sustained significant wave heights near LPL. This is the only occasion where wave-driven currents contribute to the recorded $\bar{v}_{IS}$.

The average inner-shelf salinity is 33.3 psu with freshening events associated with plume arrivals (Figure 3.2e). Ebb tide plumes consistently reach the 8-m isobath (450-m

offshore) near the estuary, whether that be north (O-N), centered on (O-C), and/or south (O-S) of the estuary mouth (Figure 3.2e). Plumes following rain events exhibit lower salinity pulses that extend farther offshore and alongshore. For ∼5-7 days following a storm, with the increased amount of freshwater in the estuary, plumes can reach the 30-m isobath (O30-C, 1.7-km offshore).

During the study period, eleven winter precipitation events occur in LPL's watershed. Eight of these events result in river discharge $\leq$ 16 m^3/s. The winter precipitation accumulation in water year 2023 is above average for the San Diego hydroclimate, with 400-mm total rainfall, compared to the average of 245-mm (https://www.weather.gov/sgx/Cliplot). The three largest events are all land-falling atmospheric rivers. They cause Q_{river} to peak at 73.8, 118.2, and 72.1 m^3/s on January 1, 15, and 16 and will be referred to as cases 1, 2, and 3 respectively (gray shaded regions in Figure 3.2). All three cases disrupt the estuary's tidal currents and generate outgoing $\bar{v}_e$ of up to -0.38, -0.82, and -0.99 m/s respectively that persist beyond a tidal cycle (Figure 3.2b). The estuary water column is completely fresh (<1 psu) from top to bottom (which is <5-m deep) during the majority of the times with estuary outflow and creates an active source region during these cases. In contrast, the smaller discharge events reduce but do not entirely freshen water at depth, and exhibit strong vertical stratification within the estuary (not shown).

3.4 Regimes of Plume Formation

3.4.1 Creation of Plume Formation Parameter Q^*_{reg}

Low-inflow systems like LPL have a plume source region that turns on and off, not consistently forming plumes. In order to model plume transport accurately, we must first know when plumes occur. In this section, we quantitatively define two regimes of small plume formation: the tidal regime and the river regime. The tidal regime is when plume formation is tidally pulsed, and the source region is only active during ebb tide. The river

regime is when plume formation can occur regardless of tidal phase, and the source region is active over one or more full tidal cycles. These represent the extreme events for the system with the highest outgoing freshwater flux.

To estimate when plume formation occurs in small river systems, the discharge regime parameter (Q^*_{reg}) is created where the * indicates it is non-dimensional. Q^*_{reg} represents the ratio of outgoing river transport (Q_{river}) to the total volume transport (Q_{total}) at the estuary mouth:

$$Q^*_{reg} = Q_{river} \ / \ |Q_{total}| \tag{3.2}$$

Q_{river} is directly measured, upstream of tidal influences, at USGS-11023340 (see Availability Statement) and represents the influx of terrestrial freshwater to the estuary. Q_{total} is an estimate of volume transport at the mouth due to the pressure gradient between offshore ocean and near-mouth estuary water levels (Figure 3.3a). The offshore water level is primarily influenced by tides, and has a smaller contribution from wave setup (see Appendix 3.A). The estuary water level oscillates primarily due to tides, but can also increase from elevated river flow after rain events. Therefore, this approach for Q_{total} generates an estimate inclusive of tidal, wave, and river contributions to the total volume transport at the mouth. When Q^*_{reg} is greater than or equal to 1 it indicates the river regime, and when it is less than 1 it indicates the tidal regime. When $Q^*_{reg} < 1$, the river discharge is relatively low and the total volume transport is dominated by the tidal contribution of Q_{total}, i.e., the source region is in the tidal regime. The source switches to the river regime when the volume transport is dominated by river discharge (Q_{river}) and occurs at Q^*_{reg} values around 1 when Q_{river} is close in magnitude to Q_{total}, hence a threshold of 1 is taken to be the transition point between regimes. In the river regime, plume formation can occur anytime during a tidal cycle because the river discharge has the greatest contribution to the total volume transport ($Q^*_{reg} \geq 1$) and the direction of net

transport is out of the estuary. In the tidal regime, plume formation only occurs during ebb tide. The Q^*_{reg} parameter can be used to estimate the river discharge necessary to shift a system out of the tidal regime, given the estimated opposing forces. If Q^*_{reg} is applied to a mid-size or large plume system it would represent when the tidal or river forcing dominates, but the tidal regime would not necessarily imply a stoppage of plume formation at the source region as it does in small plumes.

The parameter Q^*_{reg} is derived in detail in Appendix 3.A. The derivation of Q_{total} is done with publicly accessible data to ensure this approach could be used without having an ADCP deployed within the estuary and may be applicable to other low-inflow systems. Key components of the derivation include applying a pressure-friction momentum balance to obtain the mouth velocity (v_{mouth}) and thus the total mouth discharge (Q_{total}). The momentum-based approach for the Q_{total} estimate bolsters our understanding of the prevalent dynamics in this LIE and encourages reproducibility of this approach to other systems. Other important details of the Q^*_{reg} calculation include lagging Q_{river} (Figure 3.3b), and accounting for the changing sill height at the mouth impacting the mouth area to estimate Q_{total} (Figure 3.3c). Here we show a comparison between the observed value ($Q_{total,o}$), calculated by adjusting the upstream ADCP observed velocities to the mouth, and Q_{total} estimated from publicly accessible data using this momentum balance which performs moderately well with an $r^2 = 0.61$ and RMSE = 8.75 m^3/s (Figure 3.3c). The resulting Q^*_{reg} uses $|Q_{total}|$ and is averaged to one value per tidal phase (Figure 3.3d). Parameter inputs are estimated using continuous, publicly available data and include a nearby ocean tide gauge, wave information, estuary water level, and upstream river discharge (sources listed in the Open Research Section). The following results do not change if $Q_{total,o}$ is used in place of Q_{total} in the calculation Q^*_{reg}, see Supplementary Figure 3.B.1.

The definition of Q^*_{reg} is such that it can be greater than 1 during times where outgoing river discharge is competing with incoming tides and waves. Q^*_{reg} reaches values

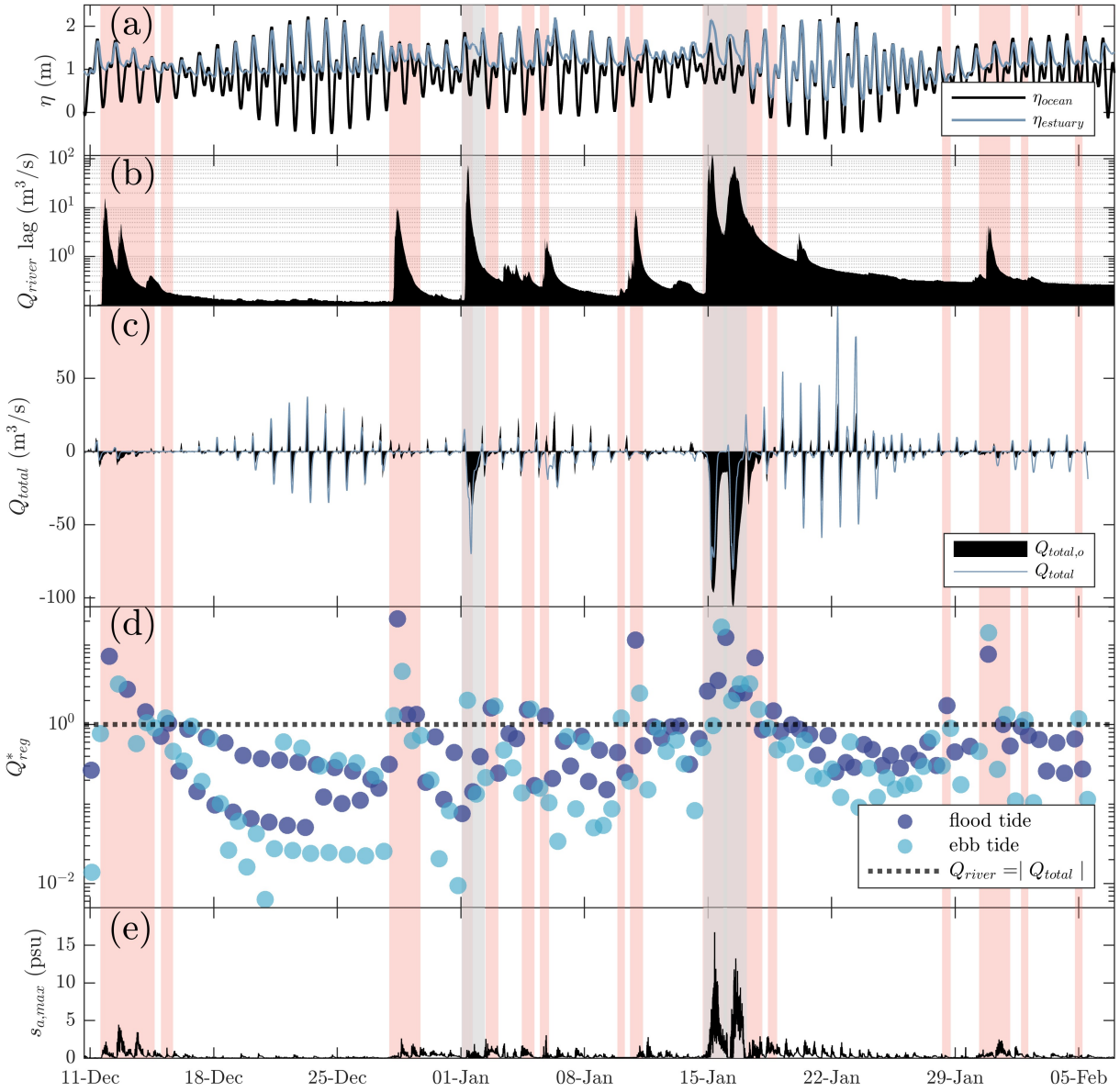


Figure 3.3. (a) Water level in the ocean (η_{ocean} in black) and estuary ($\eta_{estuary}$ in gray). (b) Q_{river}, with y-axis in log scale, lagged by 5.2 hrs to better match when river discharge measured at the gauge reaches the estuary. (c) Q_{total} estimate is shown with a gray line and $Q_{total,o}$ is shown in black shading. (d) Q^*_{reg}, y-axis in log scale, averaged over each ebb (light blue) and flood tide (dark blue). The dashed black line is $Q^*_{reg} = 1$ where $Q_{river} = |Q_{total}|$. (e) the maximum salinity deficit between the freshest surface salinity from any 'O-' moorings and O-S3's near-surface salinity ($s_{a,max}$). Instances where $Q^*_{reg} \geq 1$ and indicates a river regime are shaded in pink across all panels. Cases 1-3 are shaded across panels in light gray. Note this time series is shorter than that on Figure 3.2 and ends just before the first estuary closure on Feb-06.

up to ∼10 regardless of whether it is calculated with Q_{total} or $Q_{total,o}$ (Figure 3.3d and Supplementary Figure 3.B.1) due to exceptionally low values of Q_{total} with respect to those of Q_{river}. To prohibit parameter values from approaching infinity, a cutoff of $|Q_{total}| > 0.15$ m^3/s is required for the corresponding Q^*_{reg} to be included in the tidal phase averages shown in Figure 3.3d.

3.4.2 Parameter Implications

LPL exhibits both tidal and river regime plumes. Times of plume formation, i.e. with an active source region, can be predicted with Q^*_{reg}; plumes can form anytime when $Q^*_{reg} \geq 1$ and only during ebb tides when $Q^*_{reg} < 1$. LPL usually is within the tidal regime where the plume source region is only active on ebb tide ($Q^*_{reg} < 1$, light blue dots under the dashed line in Figure 3.3d). This is how the system predominantly operates since the river contribution to the flow is small in the absence of rain events $Q_{river} < 1.5$ m^3/s, and the tidal component can be as strong as ~ 30 m^3/s (Figure 3.3b and c). Most rain events can transition the system to the river regime where plumes can form over one or more full tidal cycles ($Q^*_{reg} \geq 1$). The river regime is often followed by a tidal regime with enhanced freshwater volumes lasting for ∼5-7 days (Figure 3.2e).

The relative timing of river discharge and tides impacts when a plume will form. Even small rain and discharge events can move this system into the river regime if they occur during weak enough tides (see pink highlighted regions on Figure 3.3d). The river regime even occurs occasionally when there is no precipitation (Figure 3.3d) because Q_{total} is nearly zero during an entire tidal phase (very weak neap tides and/or choked mouth estuary conditions), and therefore even the background Q_{river} is sufficient to produce a plume. On the other hand, not all rain events cause a shift to the river regime especially when they coincide with stronger spring tides. This emphasizes the necessity of having a dynamic ratio like Q^*_{reg} to predict plume formation, and why a static Q_{river} threshold would not work for this purpose.

The three case studies all occur during the river regime (shaded areas in Figure 3.3). Case 1 reaches the estuary just as the large ebb tide begins. This timing, combined with Q_{total} overestimating the observed volume transport, results in a short one ebb tide point in the river regime. This contrasts cases 2 and 3 which are better estimated by Q_{total} in magnitude and result in multiple consecutive tidal cycles in the river regime as would be expected. One limitation of this approach is the representation of incoming freshwater volume transport with a lagged Q_{river}, where the lag is fixed. The evolution of freshwater through the watershed into LPL is not straightforward and the hydrologic processes impacting this process are beyond the scope of this study. This highlights the complexity of these systems and emphasizes their sensitivity to the precise timing of discharge pulses to the mouth.

While Q^*_{reg} considers the relative influence of river, tidal, and wave processes on the source region and shares some similarities with small plume trapping parameterizations (Wong et al., 2013; Rodriguez et al., 2018; Kastner et al., 2019; Lou et al., 2025) and with an analysis in Orescanin, Scooler (2018) to examine mouth morphology, it is not used here to identify near-field plume trapping nor morphological change. A proxy for plume presence on the inner-shelf (near-field escaping) is calculated as $s_{a,max} = s_{min} - s_{ref}$ where s_{min} is the freshest surface salinity from any of the 8-m isobath moorings and s_{ref} is O-S3's near-surface salinity (Figure 3.3e). Most river regime periods do see escaped inner-shelf freshwater (larger $s_{a,max}$ when $Q^*_{reg} \geq 1$), although there is not a consistent trend between the magnitude of Q^*_{reg} with that of $s_{a,max}$. This emphasizes the importance of processes that occur after the source region that influence plume trapping.

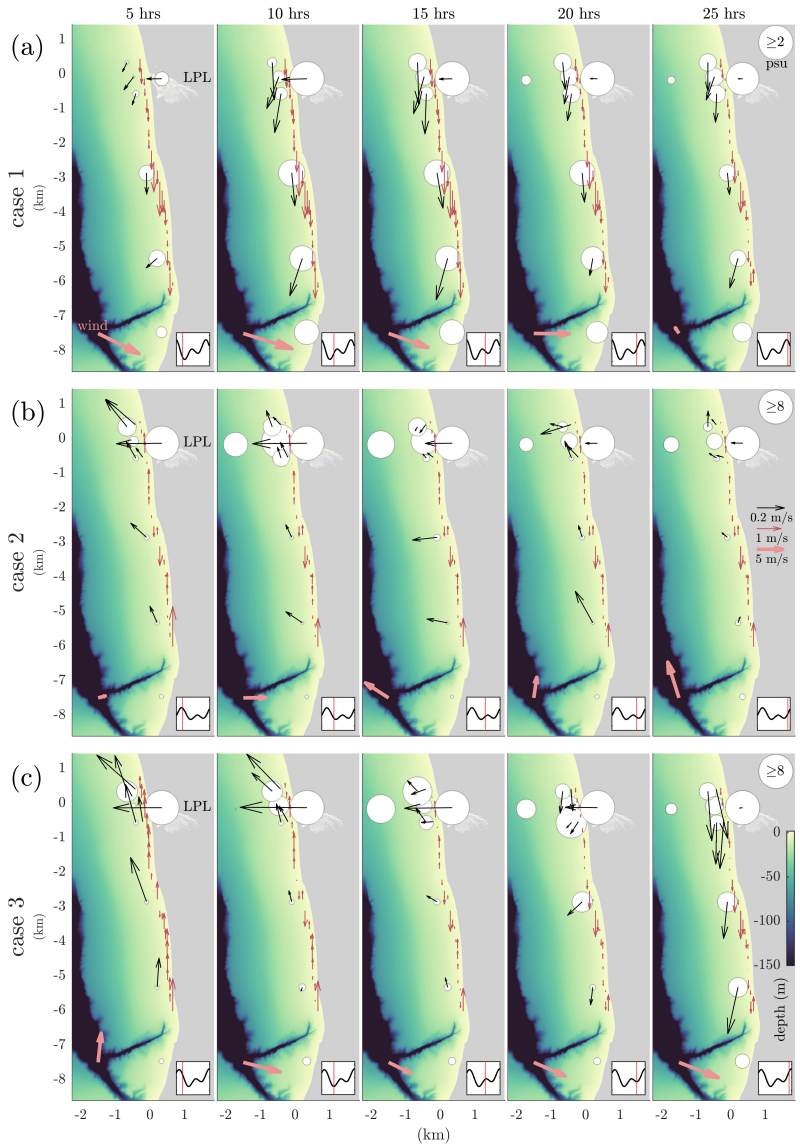


Figure 3.4. Snapshots of data during cases 1, 2, and 3 (rows a, b, c) at 5, 10, 15, 20, and 25 hrs (columns) after plume start. Black arrows show v_{IS} near-surface velocity, red arrows show v_{SZ}, and white markers show negative salinity anomaly from a 33.3 psu mean at the surface CTDs. The salinity anomaly scales differ between row 1 and rows 2 and 3. Wind is shown with thicker pink arrows in the bottom left corners. The scale for the wind and velocity vectors (offshore, in the surf zone, and in the estuary) differ. All scale vectors are shown in the last panel for case 2, except the estuary velocity scale which is twice that of the offshore vectors, 0.4 m/s for the same black scale arrow shown. Tides are shown in the bottom right corner of each map with y-limits of -0.33 to 2.21 m, and with the red line denoting the snapshot time. Note that O100-C is not shown on this map and only sees a salinity anomaly in case 2.

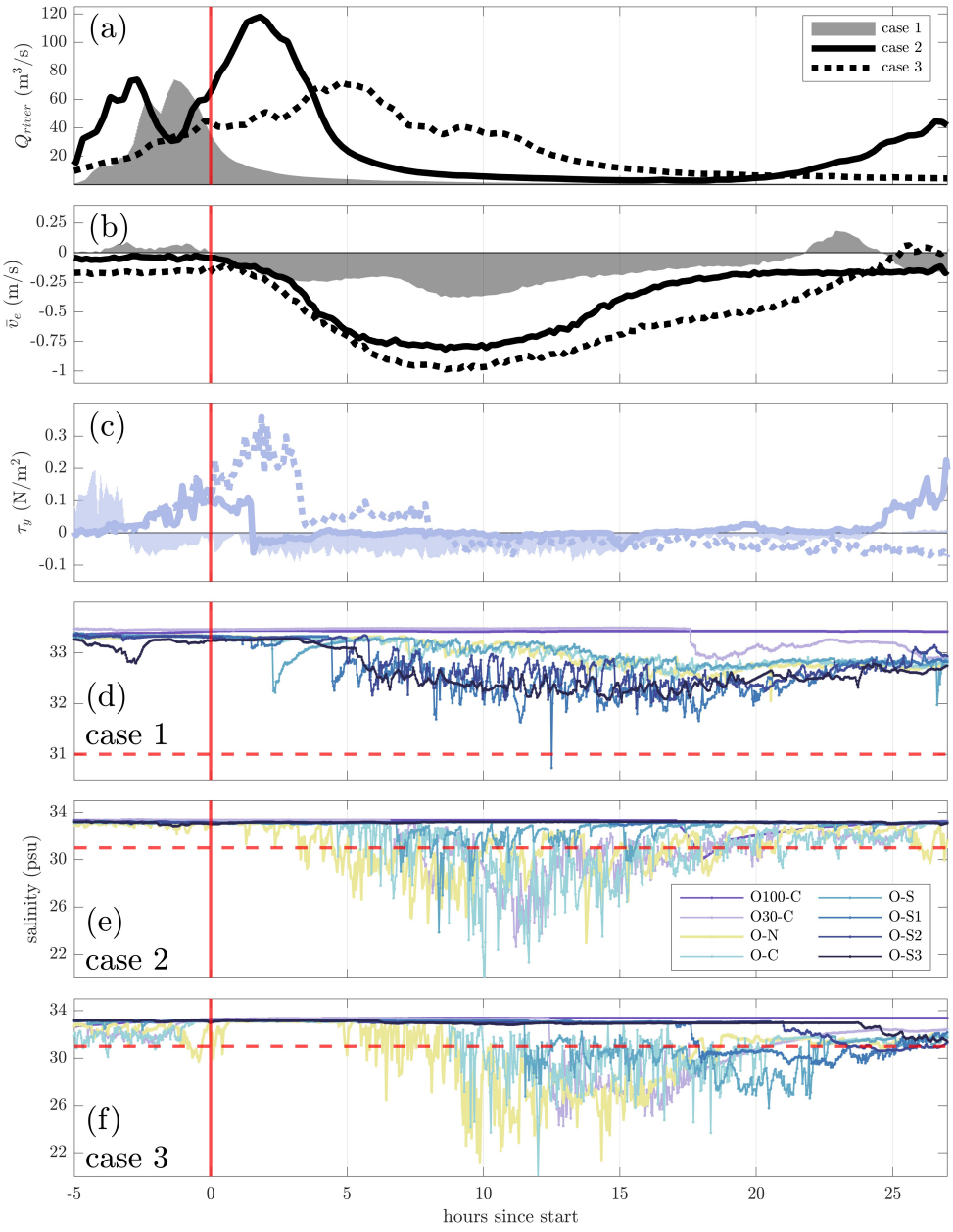


Figure 3.5. Comparison of three case studies with discharge (a), estuary velocity (b), and alongshore wind stress (c). Case 1 is shown with shading, case 2 with a solid line, and case 3 with a dotted line. Salinity for cases 1-3 is shown in d-f, respectively, and colored by mooring location. Hour zero refers to the start of plume formation for each case and is denoted with a vertical red line. The end of case 2 (hours 22-27) is the same as the beginning of case 3 (hours -5 to 0) because they occur sequentially. On panels (d)-(f) the red dashed horizontal lines indicate 31 psu, note the differing y-axis limits between case 1 (d) and cases 2-3 (e-f).

3.5 Case Studies: Plume Transport

3.5.1 General Conditions

We use low-salinity signals to track the three case study plumes through the study region and create a picture of each one's transport (Figure 3.4). These plumes dynamically respond to varying environmental conditions, as seen in snapshots of the available data at 5 hr intervals for each case starting 5 hrs after the plume starts (Figure 3.4). Each case's start time (referred to as hour zero) is referenced to the start of the strengthening in the outgoing estuary flow ($\bar{v}_e$) immediately following river discharge, denoting the beginning of plume formation. Potential times of plume coalescence are calculated using stream gauge data and maximum inner-shelf and typical surf zone currents, to provide a low-end estimate for how long a plume from a northern estuary would take to reach any mooring following its discharge.

Case 1 does not initially reach the inner-shelf at any of the near-estuary moorings, aside from a quick pulse passing O-S. It moves southward in the surf zone and reaches the inner-shelf via surf zone to inner-shelf exchange processes at multiple points southward through the end of the domain, past O-S3 (Figure 3.4a, Figure 3.5d). Diluted plume water that arrives at the near-estuary moorings around hr 7 could originate directly from LPL or from San Elijo Lagoon coalescing with LPL's plume. Case 2 moves straight offshore of the estuary, reaching O30-C at the 30-m isobath and O100-C at the 100-m isobath. It travels with a slight preference for northward transport but primarily moves offshore (Figure 3.4b, Figure 3.5e). Case 3, similar to case 1, does not immediately reach the inner-shelf. After $\sim$5 hrs it reaches the inner-shelf north of the estuary mouth at O-N, then proceeds to move offshore and southward, ultimately reaching the southernmost mooring O-S3 (Figure 3.4c, Figure 3.5f). After 13-16 hrs, plumes from San Dieguito and/or San Elijo could coalesce with that of LPL and contribute to the observed plume salinity signals. In all cases, the freshwater content decreases with distance from the mouth due to spreading and

mixing. All cases eventually move offshore despite predominantly onshore wind conditions (Figure 3.4).

Table 3.1. Physical parameters for each case.

Parameter	**Case 1**	**Case 2**	**Case 3**
T_Q (hrs)	21.8	26.8	25.3
Q_{river}^{max} (m^3/s)	73.8	118.2	72.1
Q_{river}^{sum} (m^3)	960,085	2,674,272	3,257,069
$\bar{v}_e$ (m/s)	0.20 [0, 0.38]	0.40 [0.04, 0.82]	0.59 [0, 0.99]
U_w (m/s)	8.69 [5.6, 11.6]	3.95 [0.5, 10.7]	7.21 [2.1, 15.3]
D_w (°)	283.8 [246, 303]	208.0 [3, 357]	257.7 [164, 330]
H_s (m)	2.7 [1.6, 3.1]	1.8 [1.5, 2.2]	2.1 [1.5, 2.6]
T_p (sec)	9.7 [7.1, 14.3]	14.1 [11.1, 15.4]	12.4 [11.1, 13.3]
D_p (°)	265.6 [252.3, 270.7]	258.4 [255.5, 261.5]	261.6 [259.8, 263.5]

The average value is shown at the front, followed by the range (square brackets). T_Q is outflow duration, Q_{river}^{max} is maximum river discharge, Q_{river}^{sum} is cumulative river volume discharged, $\bar{v}_e$ is depth-averaged estuary velocity, U_w is total wind speed, D_w is wind direction, H_s is significant wave height, T_p is peak wave period, and D_p is peak wave direction.

Incident wave conditions vary between each of the three cases (Table 3.1). Case 1 experiences the largest waves with an average significant wave height (H_s) of 2.7 m coming from an average angle of 266°. Case 2 has the calmest waves with average H_s of 1.8 m from 258°. Case 3 has the most variable wave conditions during the time of formation, with an average H_s of 2.1 m and direction of 262°. The shore-normal direction at the river mouth is 262° but varies slightly along-coast. Coriolis is negligible in all three cases, as is expected from low Q, low Kelvin number plumes (Warrick et al., 2007; Garvine, 1995). The following sections delve into the impacts of waves (Section 3.5.2), wind (Section 3.5.3), and buoyancy (Section 3.5.4) on the transport of these case studies. We show that these three components can largely explain the behavior of river regime plumes in the far-field.

3.5.2 Surf Zone Impacts

Here, we designate whether a SZ-field exists for the three cases and show how it controls the delivery of plume waters to the far-field. Specifically, we show that the

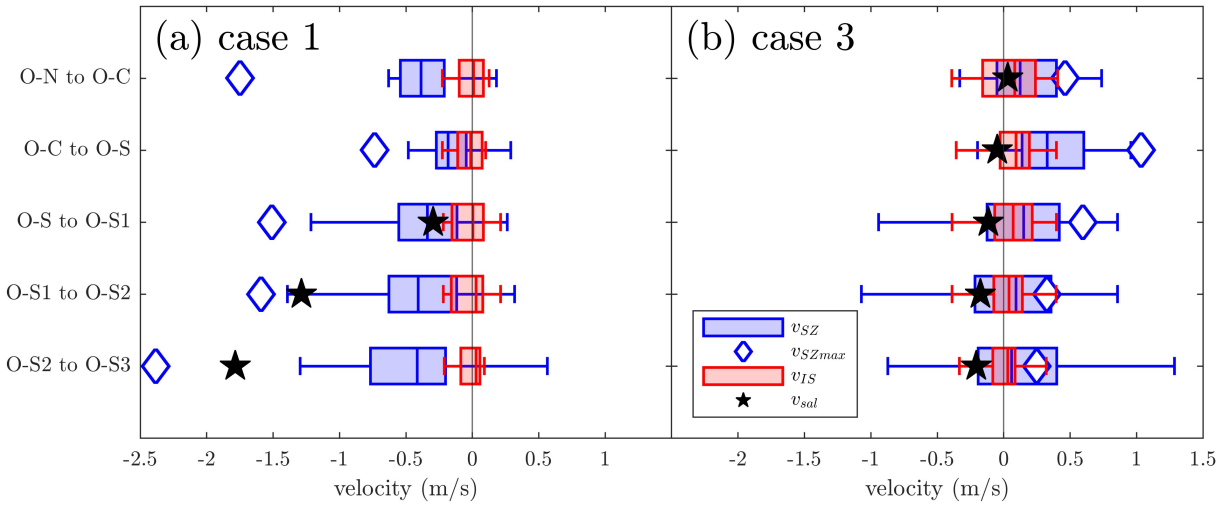


Figure 3.6. Comparison of plume arrival speed (v_{sal}, black stars) with the estimated surface currents in the surf zone (v_{SZ}, blue box and whiskers and median v_{SZmax}, blue diamonds) and those observed on the inner-shelf (v_{IS}, red box and whiskers) between each mooring pair for (a) case 1 and (b) case 3. Note the calculation of these box plots is described in the text. Case 2 is omitted as it did not travel predominantly alongshore.

SZ-field can exist in place of, or in addition to, the near-field, and before the far-field for small plumes. We can assess the role of the SZ-field in delivering plumes to the inner-shelf in the far-field by comparing surf zone and inner-shelf currents to the plume speed. Specifically, estimated alongshore surf zone currents (v_{SZ} and v_{SZmax}) and near-surface inner-shelf velocities (v_{IS}) are compared to the plume speed (v_{sal}) determined by salinity front propagation. For v_{sal}, when applicable, one value is calculated as the distance between moorings divided by the time difference for the salinity to initially drop between moorings (black star, Figure 3.6). Surf zone current estimation methods for v_{SZ} and v_{SZmax} are described in Section 3.2.3. Because Lagrangian transport reflects an integration of velocity along the path, we consider a range of velocities between each alongshore mooring pair over multiple hours from the start of plume formation. For surf zone currents, this range includes estimates from every 100-m transect between each mooring pair (v_{SZ}, blue boxes and median v_{SZmax}, blue diamonds, Figure 3.6). An exception is between O-S2 to O-S3 which only has v_{SZ} and v_{SZmax} estimates for the northernmost 700-m (of the

total 2300-m). The range of values in v_{SZ} and v_{SZmax} do not account for buoyancy or changes in bathymetry (which is measured by v_{IS}). For inner-shelf currents, this v_{IS} range includes both moorings' near-surface velocities when possible, or only one mooring's when two were not available (v_{IS}, red boxes, Figure 3.6). Surf zone plume transport, before its delivery to the inner-shelf, is confirmed if a plume's arrival speed is faster than the inner-shelf currents but equal to, or slower than, the surf zone currents.

The case 1 plume primarily transports in the SZ-field to the far-field. Its freshwater first appears briefly at O-S ∼2 hours after the outflow begins (for <2 hrs in duration; Figure 3.5). Between hours 4-7, it arrives at O-S1, O-S2, then O-S3 after it is no longer at O-S (Figure 3.4a). The arrival of case 1 to these southern moorings (O-S through O-S3) is faster than the inner-shelf currents but it is similar to the speed of the surf zone's alongshore currents (v_{SZ} and v_{SZmax}). v_{sal} is roughly -1.3 m/s between O-S1 and O-S2, and -1.8 m/s between O-S2 and O-S3. Only the surf zone, with v_{SZmax} up to -2.5 m/s could be responsible for this rapid alongshore transport (Figure 3.6a). Even the smaller pulse at O-S arrives with $v_{sal} = 0.29$ m/s, which is well within the range of the surf zone current speeds (v_{SZ}) but faster than the inner-shelf currents. S_{xx} is also strongest at the mouth during case 1, median $S_{xx} = 0.40$ m^2, relative to the other two cases. The strong wave forcing and the rapid v_{SZ} that result are sufficient to trap the plume and advect it alongshore in a SZ-field.

After case 1 advects in the SZ-field away from the mouth into the far-field, it must escape to the inner-shelf at multiple exit points. v_{IS} between O-S2 and O-S3 is too slow to explain a plume completely ejecting from the surf zone and only traveling on the inner-shelf (Figure 3.6a). The large magnitude of v_{sal} suggests this case at least partially continues with a SZ-field past mooring O-S2 and ejects from the surf zone again nearer to O-S3. It is also worth noting that the salinity deficit observed over the inner-shelf is less for case 1 than the other two cases (note the different y-axes on Figure 3.5d compared to e and f). This could be due to a relatively lower freshwater input (Table 3.1) or it could be a

result of its SZ-field transport because the surf zone is a location of significant mixing due to gradients of wave momentum flux and of wave energy flux (Thornton, Guza, 1983, 1986; Feddersen, Trowbridge, 2005; Feddersen, 2012; Hally-Rosendahl et al., 2014; Spydell et al., 2019; Kastner et al., 2023). While plume mixing is not a focus of the present work, implications for mixing based on these observations are discussed in Section 3.6.3.

Case 2 plume transport is not significantly altered by wave processes; this case appears similar to what is predicted by models that ignore surface gravity waves, or have very small waves relative to the river discharge. If it has a SZ-field, it is small and results in minimal impact on the overall plume transport. The case 2 plume forms during the weakest and least variable wave conditions. With a lower $S_{xx} = 0.3$ m^2 coupled with the highest river discharge, as well as relatively low $S_{xy} < 0.02$ m^2 and hence near zero surf zone alongshore currents (Figure 3.4b); it is unlikely that waves influence the transport of the plume in this case. If some amount of freshwater advects in the surf zone, it would move north in the estimated direction of wave-driven flow (Figure 3.4b). Case 2 is not shown in Figure 3.6 given that the plume transport is predominantly in the cross-shore direction and surf zone currents are not important to its transport.

The case 3 plume advects via the surf zone and/or inner-shelf; v_{sal} between all mooring pairs can be explained by either the inner-shelf or the surf zone currents (Figure 3.6b). The case 3 plume forms when the surf zone has fast northward alongshore currents (Figure 3.4c). A component of the plume likely travels north within the surf zone outside of our sampling domain. The plume first arrives at O-N $\sim$5 hrs after the plume start, suggesting it could experience northward surf zone transport before moving offshore $\sim$5 hrs later (Figure 3.4c). The wave conditions rapidly change to favor southward surf zone flow, creating a much more variable S_{xx} than case 2 and an S_{xy} that decays to zero as it switches sign and then continues to grow in strength. As a result, median v_{SZmax} appear near zero (Figure 3.6) despite having medians in each direction that are close to the whisker limits. This weakening and then lapse in surf zone alongshore currents, plus

the weaker S_{xx}, could suggest the plume is initially trapped and advecting in the surf zone, but later directly escapes to the inner-shelf from the mouth. This plume could also shift directions once on the inner-shelf, initially exiting the surf zone north of the mouth (moving northward) but later switching to move southward on the inner-shelf. This could bring older plume water to the south from LPL or cause coalescence with plumes from the two northern estuaries. It is uncertain whether this is true or if a near- and mid-field plume form at the mouth when conditions slacken. While the latter is more likely since the plume moves farther cross-shore than may be expected from a surf zone ejection ($\sim$1.7-km to O30-C, Figure 3.4c), the exact pathway is unknown. This highlights the complex and dynamic spatial and temporal distribution of small plumes; plume waters can advect via various paths within different dynamic regions, especially as conditions change.

These results show that waves and surf zone processes impact transport of small river plumes through a SZ-field into the far-field. Knowing the surf zone conditions in the near-field is useful for anticipating a plume's initial behavior, but if a plume has a SZ-field, the wave conditions along the entire trajectory are necessary to explain its ultimate fate (case 1). Conditions can also change during the time of plume formation (case 3), hence a plume with a SZ-field may also develop a prototypical mid-field near the mouth later on, or vice versa. This shows how the far-field can be reached through either a near- and mid-field, and/or through the SZ-field and elucidates the variable spatial distribution of small plumes. Models that do not include wave processes could not have accurately described the transport of two of these case studies. Additionally, models must properly represent surf zone to inner-shelf exchange processes to anticipate the timing and strength of plumes within the surf zone and in the far-field. This echoes previous findings (Wong et al., 2013; Rodriguez et al., 2018; Kastner et al., 2019; Lou et al., 2025) that the surf zone is important for small plumes near the mouth, and we add that understanding the entirety of the SZ-field is critical to predicting the fate of small plumes.

3.5.3 Wind Impacts

Once a plume reaches the inner-shelf, wind becomes important. Strong winds can drive ambient inner-shelf currents that are coherent over the full water column in the direction of wind forcing due to the direct stress (Lentz, Fewings, 2012). Storm events are often associated with strong winds in the study region. Cases 1, 2, and 3 had average wind speeds of 8.7, 4.0, and 7.2 m/s, respectively, during the time of plume formation (Table 3.1) but often change during each case (Figure 3.5c). Small plumes have been shown to respond to direct wind forcing, as opposed to Ekman wind dynamics, due to a minimal contribution of Coriolis to these transient plumes (Warrick et al., 2007; Romero et al., 2016; Basdurak et al., 2020; Basdurak, Largier, 2022). In this section, we explore the role of direct wind forcing on the inner-shelf transport of the three case studies. First, we compare observed plume behavior to the strength and direction of wind forcing. Then, we estimate wind-driven alongshore current speed and compare to observed plume speeds.

Case 1 has entirely southward wind and the plume moves southward (Figure 3.4a, Figure 3.5c). While this plume primarily moves in the surf zone, the inner-shelf currents are southward such that any freshwater exiting the surf zone would continue a southward trajectory along the inner-shelf. The case 2 plume forms during relatively weak and variable winds that are directed offshore at times (Figure 3.5c). As a result, the alongshore inner-shelf currents are weak and the resulting plume is not primarily moving alongshore, but instead quickly travels cross-shore (Figure 3.4b). Case 3 has winds to the north that promptly reduce and then change direction to southward ∼4-8 hours after the plume start (Figure 3.5c). This case follows the same path on the inner-shelf, initially going north of the mouth but then switching to southward propagating (Figure 3.4c).

Next, we consider how much of each plume's speed is explained by alongshore wind. An estimate for how much of the observed alongshore inner-shelf velocity could be explained by the alongshore wind (v_{wind}) is computed assuming a balance between surface

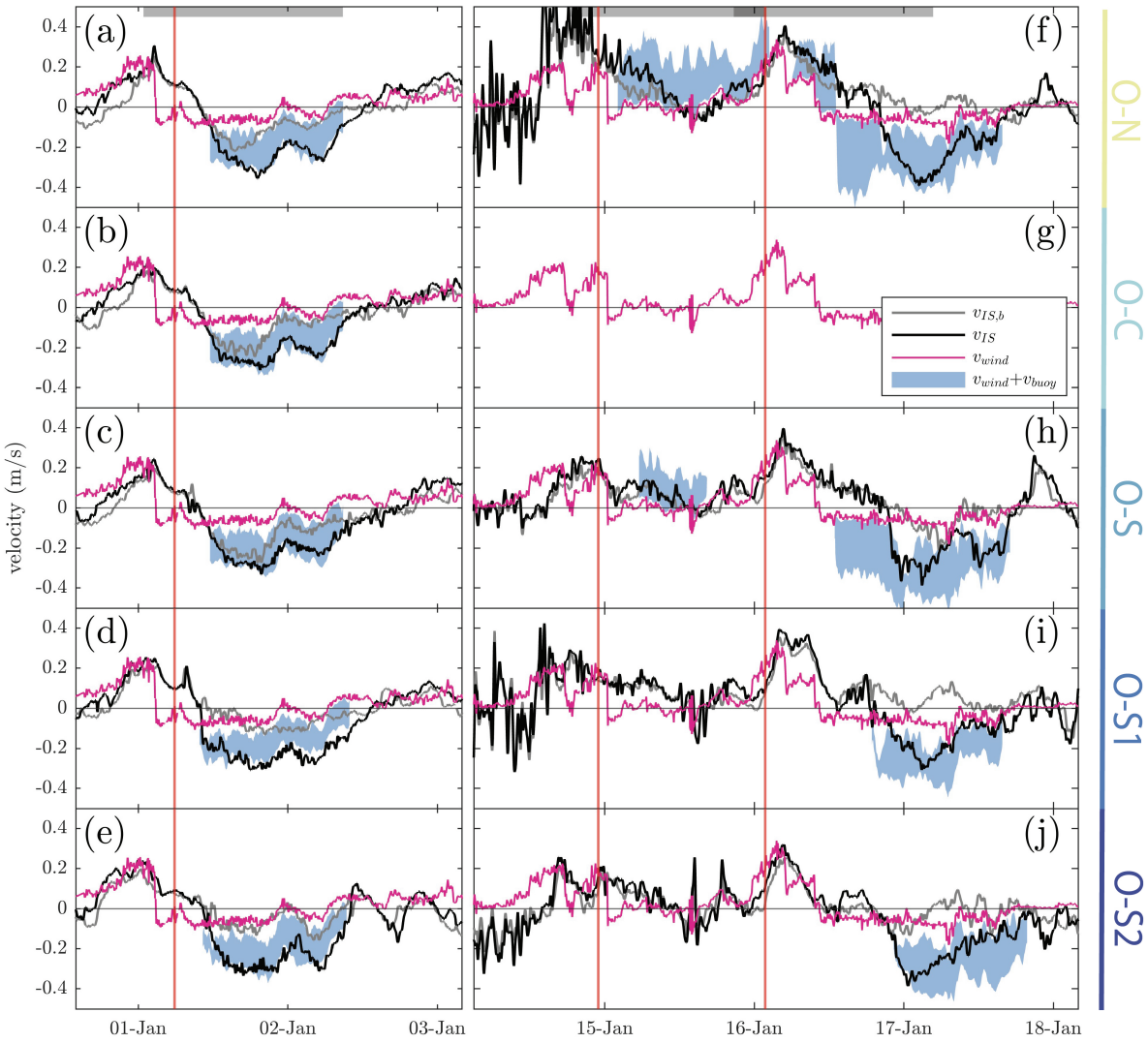


Figure 3.7. Cases 1-3 observed near surface (v_{IS}, black) and near bottom ($v_{IS,b}$, gray) inner-shelf velocities compared to the estimated v_{wind} (magenta) and $v_{wind} + v_{buoy}$ (blue shading) for each mooring (rows) for case 1 (left column) and cases 2-3 (right column). Vertical red lines denote hour 0 of each event. Horizontal gray bars at the top show hours -5 to 27 as plotted in prior figures. Note O-C was buried during cases 2-3 and velocity data is unavailable.

stress and bottom stress (Whitney, Garvine, 2005). This gives the equation:

$$v_{wind} = \sqrt{\frac{\rho_{air}}{\rho_{ocean}} \frac{C_{10}}{C_D}} * V_w \tag{3.3}$$

where ρ is density, C_{10} is the drag coefficient between the air and sea, C_D is the bottom drag coefficient, V_w is the alongshore wind speed (measured at 8.2-m above the water surface, see Open Research Section), and v_{wind} is the resulting depth-averaged wind-driven current speed. Constant values are used for $\rho_{air} = 1.225$ kg/m^3, $\rho_{ocean} = 1025$ kg/m^3, $C_{10} = 0.00125$, and $C_D = 0.003$. We take C_D to be a constant value derived in prior literature (Feddersen et al., 1998), and show that the resulting v_{wind} compares well with the observations. However, the role of bottom friction is stratification dependent and therefore dynamic in time (MacDonald, Geyer, 2004). If our approach is altered to use the MacDonald, Geyer (2004) estimate of interfacial drag ($C_D = 0.0005$), or to use the relationship between wind and plume front speed from Osadchiev et al. (2021), the resulting v_{wind} is 2.2- 2.5x larger than that of Figure 3.7 but the interpretation of the results does not change. We will continue with the commonly used Whitney, Garvine (2005) approach using $C_D = 0.003$ for the calculation of v_{wind}.

Figure 3.7 shows estimates for v_{wind} in the magenta lines on each panel compared to observed near surface (v_{IS} in black) and near bottom ($v_{IS,b}$ in gray) inner-shelf velocities. If the entire water column is wind-driven with no plume, both v_{IS} and $v_{IS,b}$ are close together and nearly equal to v_{wind}. Before the arrival of each plume, v_{IS} and $v_{IS,b}$ closely track the estimates for v_{wind} in all cases, indicating a wind-driven ambient current and that C_D is reasonable (Figure 3.7). Once the plume arrives, in cases 1 and 3 we see a deviation of v_{IS} from $v_{IS,b}$ indicating vertical shear (Figure 3.7). In these cases, $v_{IS,b}$ continues to track closely with v_{wind}, while v_{IS} is larger in magnitude, suggesting the full water column is wind-driven but that the surface plume speed (here represented by v_{IS}) has an additional component not explained by wind.

Case 1 has strong northward winds before the plume begins forming. During this time, estimates of v_{wind} match well to the inner-shelf currents at each mooring (Figure 3.7a-e). Note v_{IS} and $v_{IS,b}$ are close together implying a well-mixed water column. As Warrick et al. (2007) showed, southern California low-pressure systems typically have a northward wind preceding a plume, and then a southward wind when the plume is forming. v_{wind} sharply jumps at the start of January 1 when the winds switch southward and v_{IS} and $v_{IS,b}$ respond by gradually decreasing, passing through zero, then generating southward v_{IS}. At the far-field moorings (O-S1 and O-S2) v_{wind} remains approximately equal to the near-bottom velocities while the plume is present. This suggests a wind-driven ambient flow that the plume is traveling within. The surface has a higher velocity and cannot be entirely explained by v_{wind}. Case 3 (Figure 3.7f-j) features similar trends to case 1, an ambient wind-driven flow sets the direction of propagation but cannot match those observed within the surface plume layer. Case 3 forms while the winds are still northward (as opposed to case 1 winds which switch to southward before its formation begins). As a result, the far-field plume in case 3 switches directions from northward to southward coincident with the winds (Figure 3.4c).

Case 2 occurs with weak alongshore winds (hence a weak v_{wind}) and weak inner-shelf alongshore currents (Figure 3.7f,h). As a result, v_{wind} and v_{IS} and $v_{IS,b}$ correlate very well during this time when they are all near zero, with a slight northward direction. In this case, the lack of alongshore or onshore wind (combined with the weak waves) results in a weak ambient flow alongshore and contributes to a predominately cross-shore transport. The weak, variable, and occasionally offshore-directed winds promote a relatively large cross-shore plume extent (Figure 3.2d; Romero et al., 2016). Case 2 occurs just one day before case 3, as did the corresponding rain event. This emphasizes how the timing of one storm with respect to another and the timing of winds relative to river outflow may influence the wind patterns and hence the plume transport.

3.5.4 Buoyancy Impacts

Wind forcing can explain much of the inner-shelf velocities when the plume is not present and it indicates the direction of alongshore inner-shelf plume movement, but cannot fully explain the observed propagation speeds. This section will consider the contribution of buoyancy-driven flow to plume transport. Although not always considered a dominant driver of small plumes, we find buoyancy explains a significant portion of the observed transport.

Buoyancy forcing spreads a plume outward, often radially (Garvine, 1984). While cross-shore plume propagation is important, due to data limitations, here we focus on the buoyancy acting in the alongshore direction. To examine the impact of buoyancy on transport, first a plume depth (h_p) must be found. Vertical shear squared ($S^2 = \frac{\partial u}{\partial z}^2 + \frac{\partial v}{\partial z}^2$) is calculated at each mooring (Figure 3.8) using the cross-shore and alongshore velocities measured at each discrete depth (0.25 m spacing). There is strong vertical shear on the inner-shelf when a plume is present (Figures 3.7 and 3.8). This is not due to strong winds; the strongest water column shear is only seen in the presence of plumes and when wind-driven inner-shelf flow is nearly depth-uniform (see smaller pre-plume shear when winds are strong; Figure 3.8). The surface-intensified buoyant flow associated with a plume, due to the density difference between the plume and the ambient water, creates the observed strongly sheared layer (Figure 3.8). The quality controlled depth of maximum vertical shear (S^2) is used to estimate plume depth (h_p) at each mooring (black lines overlaid on S^2 in Figure 3.8). Upper and lower bounds for the plume depth are found using the width of the maximum shear peak at each time step.

The three case studies show different behaviors in plume depth. The case 1 plume, which arrives to the inner-shelf moorings from an energetic and wide surf zone, is able to mix all the way to depth at initial arrival at all moorings (Figure 3.8). Although the plume does not initially reach moorings O-N and O-C as it quickly moves southward in

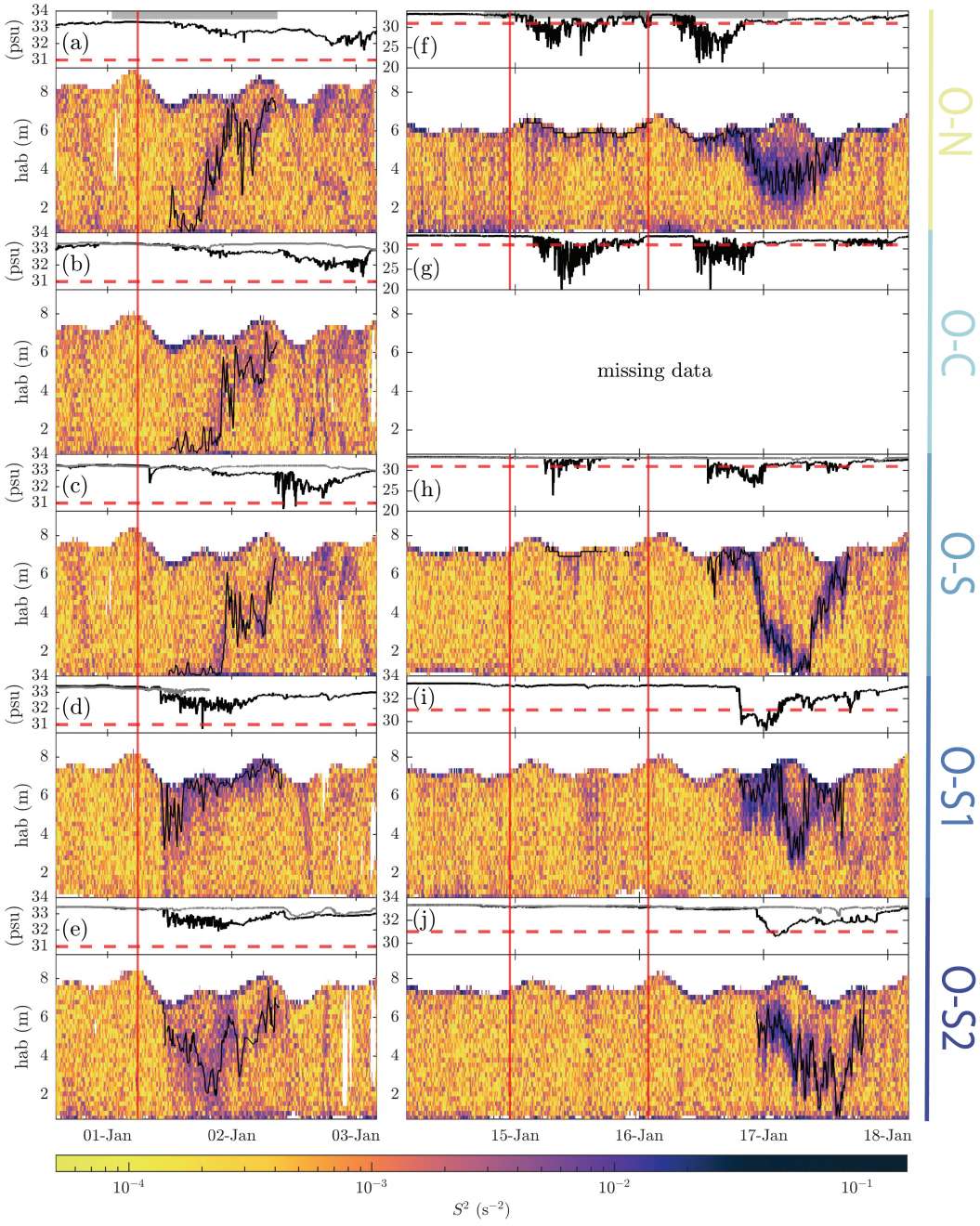


Figure 3.8. Vertical velocity shear squared (S^2) for case 1 (left column) and cases 2 and 3 (right column). Top panels of each subplot show surface salinity (black) and bottom salinity (gray), when available, and the bottom panels show the vertical profile of S^2 for each mooring. Horizontal dashed red lines mark 31 psu on each salinity panel for inter-comparison. Plume depth (h_p) is plotted in black over the shear. Vertical red lines mark hour 0 for cases 1-3 (from left to right). Horizontal gray bars at the top show hours -5 to 27 for each case as plotted in prior figures.

the surf zone, it does reach the inner-shelf moorings closer to the estuary mouth $\sim$ 3 hrs after reaching O-S1 and O-S3 (Figure 3.5d). The case 2 plume is shallower than the nearest-surface velocity measurement recorded, limiting the possible plume depth bounds to a range between near surface (0.05 m) and the depth of the top velocity bin (1-2 m, time dependent). The case 3 plume starts shallower than the velocity measurements on the inner-shelf at moorings O-N and O-S, producing a range of possible depths between the near-surface and top velocity bin. It then deepens and has the most strongly sheared plume base of any of the three cases across all moorings (max $\sim$ 0.03 s^{-2}, Figure 3.8). Near bottom salinity (gray lines, Figure 3.8) show fresh anomalies that correspond with times when the maximum shear (and h_p) reaches the bottom of the water column during cases 1 and 3, additionally supporting the use of the plume depth estimates from shear. Potential mechanisms for the differences in initial plume depth and strength of shear at the plume base between cases 1 and 3 are explored in Section 3.6.3.

Using the calculated plume depth and density anomaly, the contribution of buoyancy to the plume propagation speed is computed by $v_{buoy} = \sqrt{g' h_p}$ where g' is reduced gravity ($g' = g\frac{\Delta\rho}{\rho_0}$) with $\Delta\rho$ being the difference between plume density (ρ) and ambient seawater density (ρ_0). An upper bound on $\Delta\rho$ is found by assuming ρ_0 is equal to the highest salinity from that mooring (a constant value across time). A lower bound on $\Delta\rho$ assumes ρ_0 is a moving average over the prior 2 hrs from that same mooring. Instantaneous density from each mooring is used for ρ. A range of v_{buoy} is calculated using the upper and lower bounds of both plume depth and of $\Delta\rho$.

We examine the contribution of buoyant gravity current propagation, using the alongshore wind direction as the direction of gravity current propagation. The bounds of v_{buoy} are combined with v_{wind} and then averaged with a running mean over 30-min to represent a flow driven by both wind and buoyancy (blue shading in Figure 3.7). Buoyancy is added in the direction of wind forcing to represent an ambient wind-driven alongshore flow that is enhanced by an alongshore component of the gravity current. The case 1

plume speed is well described by a combination of wind-driven and buoyant propagation speeds (Figure 3.7a-e, black lines and blue shading overlapping). Even the well-mixed plume waters reaching the near-estuary moorings ($F \approx 0.01 - 0.03$ at O-N through O-S) contributes significantly to the inner-shelf surface velocity because of the large plume depth. Case 2 has little alongshore movement as it primarily propagates cross-shore, and it travels at least 5.2-km offshore (to mooring O100-C). This case has the most rapid arrival of salinity to the inner-shelf, likely due in part to the minimized role of the surf zone. To investigate the role of buoyancy in its cross-shore transport we look at v_{sal} between cross-shore oriented moorings O-C, O30-C, and O100-C and compare these values to v_{buoy} estimates. Case 2 has a v_{sal} of 0.18 m/s between O-C and O30-C, and 0.08- 0.13 m/s between O30-C and O100-C, and a v_{buoy} of ∼0.07- 0.17 m/s between O-C and O30-C, and 0.15- 0.37 m/s between O30-C and O100-C. This v_{buoy} assumes a range of $h_p = 1 - 5$ m between O-C and O30-C, and of $= 1 - 6$ m between O30-C and O100-C, where exact depths are unknown. These estimates come from temperature and salinity data (not shown) that bound case 2 h_p shallower than 2 m at O-C, shallower than 6 m at O30-C, and shallower than 7 m at O100-C. The plume in case 3, like case 1, is well described by $v_{wind} + v_{buoy}$ on the inner-shelf except for when the currents change direction from north to south (Figure 3.7). This mismatch around 0 m/s may be an artifact of this approach handling changes in direction too sharply, because in reality there is a spin-up time associated with the development of v_{wind}. Once the plume is moving southward, this approach works well and again matches a realistic range of speeds. Despite only having a freshwater fraction $F \approx 0.02 - 0.03$ by the time the plume reaches moorings O-S1 and O-S2 in case 3, the plume depth has increased causing it to maintain a notable buoyant speed.

These results suggest that buoyancy is an important dynamic in the far-field transport of these case study plumes. The wind-driven inner-shelf sets the direction that the plume will travel and transports the plume, while buoyancy contributes additional

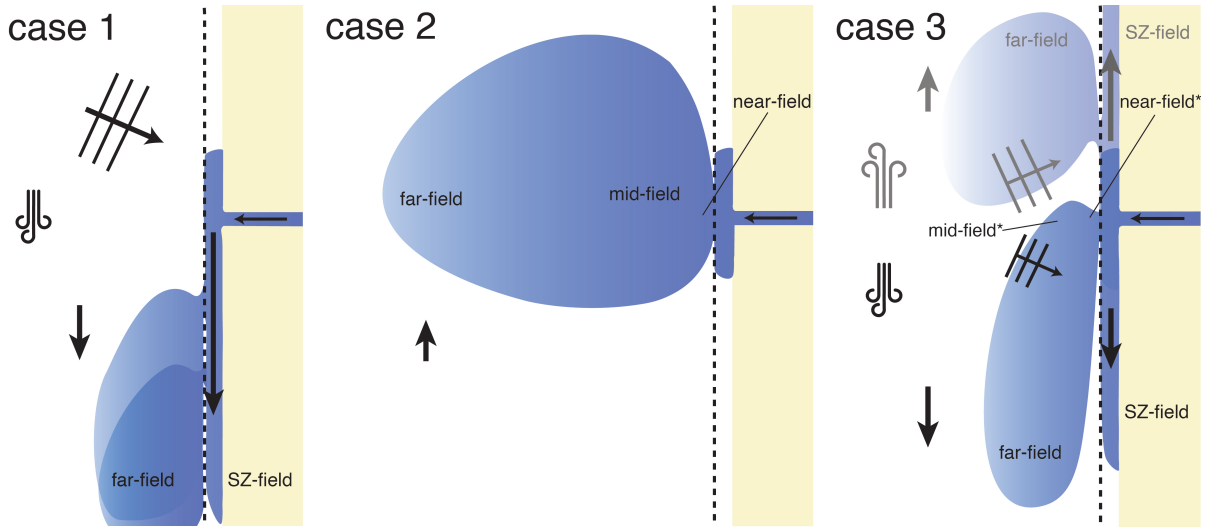


Figure 3.9. Schematic representation of observed plume transport for cases 1, 2, and 3. The black dashed lines indicate the surf zone edge. The dynamic regions present in each case are labeled. Asterisks indicate an uncertain but potential dynamic region. Arrows indicate current velocities, arrows with cross-hatching indicate prominent wave conditions, and the wind symbol indicates prominent wind conditions. Gray icons and lighter shading show early plume movement in cases 1 and 3 before conditions change. In case 1, rip currents likely exist at multiple points along the surf zone, but only 2 are shown for simplicity. Additionally, rip currents may remain active for longer periods of time than illustrated here.

speed (Figure 3.7). This emphasizes the importance of buoyant forcing in these small plumes in the far-field, and emphasizes that plumes can be clearly identified at very low freshwater fractions. We add to the findings of Basdurak, Largier (2022), that show buoyancy is important in limited cases (low or rising tide with weak northward winds), to explain that buoyancy contributes to far-field transport under a diversity of wind and tide conditions. Future studies could investigate the magnitude of buoyant contributions to plume speed using higher resolution observations to narrow the gravity current estimation's uncertainty.

3.6 Discussion

3.6.1 Conceptual Overview & Dynamical Plume Regimes

In this study, we look at the dynamics behind both the occurrence and the transport of small plumes. The occurrence of small plumes in low-inflow systems is typically driven by tides. However, after sizable rain events, plumes can form regardless of tidal phase. We create the parameter Q^*_{reg} that defines how strong of river discharge is needed to produce a plume given the tide and wave conditions. These are labeled the tidal and river regimes, respectively. The tidal regime only has an active source region during ebb tide whereas the river regime has an active source region for one or more full tidal cycles.

Once a plume forms, it can have a number of dynamical regions (Garvine, 1984; Horner-Devine et al., 2015). These regions are distinguished as areas of the plume where the governing dynamics are distinct. However, small plume regions are not always categorized clearly into this existing framework. Through three case studies, we show that not every small plume will have the same dynamic regions and moreover, these plumes are clearly impacted by the surf zone. While previous work (Wong et al., 2013; Rodriguez et al., 2018; Kastner et al., 2019; Lou et al., 2025) has looked at the near mouth surf zone properties to determine if a plume is surf zone trapped near the mouth, we instead consider the influence of the surf zone on plume transport with implications for its ultimate fate. We investigate the SZ-field dynamical plume region, which encompasses the conveyor belt of surf zone currents that move plumes alongshore, mix them vertically, and can deliver them to the inner-shelf/ far-field away from the mouth. In case 1, SZ-field processes play a critical role in far-field plume fate, spreading the plume alongshore more quickly than otherwise possible and likely contributing to mixing. This surf zone region has dominant dynamics that differ significantly from the near- mid- or far-field as previously defined by Garvine (1984). The SZ-field likely has a momentum balance dominated by gradients in the wave radiation stresses and by bottom stress, and it can be influenced by wave-driven

processes such as Stokes drift and strong vertical mixing (Feddersen et al., 1998; Lentz, Fewings, 2012; Spydell et al., 2019). The role of buoyancy, channel mouth bathymetry/ angle, wind, and river momentum in the SZ-field is unknown and the subject of future work.

The different dynamic regions present in the three case studies illustrate the strong event-by-event variability in the transport of even the most strongly forced small plumes from this period. The case 1 plume has a SZ- and far-field (Figure 3.9). The case 2 plume has a near-, mid-, and far-field. Lastly, the case 3 plume has all four regions, with the dominant transport pathway changing over time with the wind, wave, and discharge conditions (Figure 3.9). The schematics in Figure 3.9 simplify the cases down to their main transport pathways, but it should be noted that the spatial structures of these plumes are often more variable and inhomogeneous than portrayed here.

Once a plume is in the far-field region on the inner-shelf, the transport is influenced by winds and its own buoyancy. Typically, winds are strong following a rain event and dominate the inner-shelf alongshore currents that advect river regime plumes (Warrick et al., 2007). When alongshore winds are strong, the far-field transport is in the direction of wind forcing. When alongshore or onshore winds are weak, the far-field plume transport is primarily cross-shore and is influenced by buoyancy. Unlike large plume systems, rotational effects including Ekman wind balances are not dominant in small plumes on these shorter spatial and temporal scales (Garvine, 1995).

Ultimately, the precise timing of the river discharge exiting the mouth with regards to the tide, wind, and waves will influence both plume formation and transport. Small plumes dynamically respond to changing conditions, following the dominant direction set by waves (in the SZ-field) and by wind (in the far-field). A component of plume speed in the far-field is due to a buoyancy-driven frontal propagation speed in the direction of the ambient current. In situations with weak ambient inner-shelf currents in the near- and mid-fields, the buoyancy will enhance propagation in the direction of river momentum

until the river momentum is no longer felt, and then it will spread the plume radially (Pritchard, Huntley, 2006; Yuan, Horner-Devine, 2013; Horner-Devine et al., 2015).

3.6.2 Applicability to Other Systems

Implications for Tidal Plumes

While this study investigates transport of the typically energetic river regime of small plumes, the results have implications for the more weakly-forced tidal regime as well. We distinguish when the tidal regime is present via the Q^*_{reg} parameter and see that it occurs with a range of environmental conditions. It features a tide-dependent source region that produces plumes only during ebb tide. In the context of the drivers explored in this study, this regime has weaker buoyancy forcing than the river regime and a plume can coincide with energetic waves and/or strong winds, or neither of those. The three case studies presented here from the river regime provide insight into how the tidal regime may behave in a range of conditions.

In general, weaker buoyancy (due to the smaller quantities of freshwater per plume) means a tidal regime plume will not travel as far or as fast as river regime plumes. If the waves are energetic and/or obliquely incident even with weak winds, the plume could behave like case 1, rapidly transporting in the surf zone then feeding out to the inner-shelf via rip currents or surf zone diffusion. If the alongshore wind is energetic but the waves are weak, the plume could behave like the inner-shelf component in case 3, dynamically following changes in wind conditions as it moves alongshore. If both the wind and waves are weak, the plume could behave similar to case 2 with a predominantly cross-shore or radially spreading bulge. This behavior is dependent on how strong the buoyant forces are in competition with the wave radiation stresses (as is explored in various previous studies; Wong et al., 2013; Rodriguez et al., 2018; Kastner et al., 2018, 2019). In the likely case where the strength of the forcings from buoyancy, waves, and wind are a similar strength (and are weak), various other factors can alter the transport of the tidal regime.

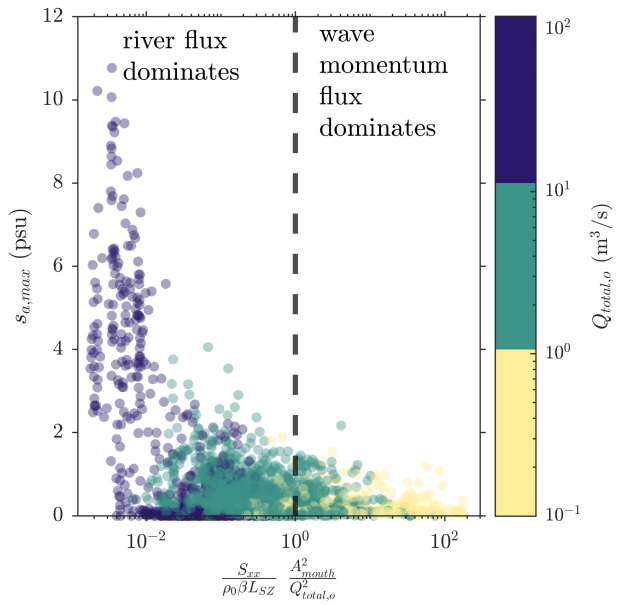


Figure 3.10. Performance of the Rodriguez et al. (2018) parameter space in showing the tendencies for LPL plumes to be river momentum dominated (escaped) or wave momentum flux dominated (surf zone trapped). The y-axis is a proxy for inner-shelf plume presence $s_{a,max}$, the maximum salinity deficit between the freshest surface salinity from any 'O-' moorings and O-S3's near-surface salinity. One scatter point, colored by estuary mouth discharge, $Q_{total,o}$, is shown for every 10 min of data, and only for times of estuary outflow. Note the log-scale $Q_{total,o}$ color bar used to highlight smaller events.

It can be altered by the bathymetry, presence of engineered structures (Kastner et al., 2019), and channel angle (Wong et al., 2013). The background surf zone to inner-shelf cross-shore exchange mechanisms (without plumes present) can be overlapping and difficult to generalize to one process (Grimes et al., 2021). Hence, understanding this exchange when weakly buoyant plumes are present likely requires a complicated combination of processes. The strength and timing of the ebb tide combined with the strength and timing of diurnal winds, internal tides, and other factors that drive inner-shelf flow must be taken into account. This absence of strong forcing makes generalizing the drivers of transport for small plumes in the tidal regime significantly more challenging.

Parameter Space Comparison

In this section, we explore the trapping versus escaping conditions of LPL's winter plumes by using an existing parameter space defined by Rodriguez et al. (2018). Their non-dimensional scaling is calculated as $\frac{S_{xx}}{\rho_0 \beta L_{sz}} \frac{A_{mouth}^2}{Q_{total,o}^2}$ where β is seafloor slope, L_{sz} is the surf zone width, A_{mouth} is the cross-sectional area at the mouth, and $Q_{total,o}$ is the observed volume transport out of the mouth. Calculations and values for β, A_{mouth}, and $Q_{total,o}$ are explained in Appendix 3.A. Here $v_{mouth,o}$ and hence $Q_{total,o}$ are smoothed over a 30 min running average and are also set to zero when the 30 min average water depth at the sill (h_{sill}) is < 0.1 m. The sill is located close to the estuary mouth and hence h_{sill} represents water depth at the estuary mouth. The surf zone length is calculated as $L_{sz} = \frac{H_s}{\alpha \gamma}$ where α is tide dependent beach slope, and $\gamma = \frac{H_s}{h_{sz}}$ with h_{sz} as the depth at the offshore surf zone edge. Values for this are taken from the CDIP wave information at LPL's mouth (MOP line 590). We compare this parameter to the maximum salinity deficit ($s_{a,max}$), a proxy for plume presence on the inner-shelf (Figure 3.10). While we do not have surf zone salinity measurements, nor measurements right near the river mouth, we use $s_{a,max}$ as a proxy for inner-shelf plume presence. When $s_{a,max}$ is large (small), there is more (less) freshwater on the inner-shelf indicating an escaped (surf zone trapped) plume.

The Rodriguez et al. (2018) parameter space seems to delineate when LPL plumes are trapped versus escaped (Figure 3.10). Rodriguez et al. (2018) cite a transition between wave momentum flux (trapping) and river flux (escaping) dominance at a parameter value of 1 (Figure 3.10). The greatest $s_{a,max}$ values occur when the scaling <1 and river flux dominates, indicating plumes that escape from the surf zone. The opposite is true for trapping conditions; a scaling >1 corresponds well with when the $s_{a,max}$ proxy indicates no/low freshwater presence on the inner-shelf. However, a limitation of the Rodriguez et al. (2018) scaling is that it did not collapse for different values of H_s; however, further analysis of that work has suggested a few ways to collapse their results. Despite this limitation,

this parameterization shows promise to collapse different sites to one parameter space, providing a clear direction for future research. Additional future work could investigate these and other observations and models in the context of different parameter spaces that consider near-field plume length (Wong et al., 2013; Kastner et al., 2019; Lou et al., 2025) and explore the potential usefulness of Q^*_{reg} as an indicator of surf zone trapping. Future observations that include the SZ-field, near-field, and the far-field regions across a range of plume formation regimes would also be greatly helpful in understanding the connections between the SZ-field, trapping/escaped conditions, and the ultimate far-field plume fate.

3.6.3 Plume Mixing

Although not a focus of this study, these plumes are turbulent and the role of mixing and eddy diffusion is important. While some turbulence measurements may be possible with our dataset, they are very limited in spatial/temporal extent. Nevertheless, there is a qualitative difference between the far-field plume's vertical structure from the surf zone advected case 1 versus the likely inner-shelf advected portion of case 3.

Case 1 has a less defined plume base and the vertical shear has a similar magnitude from top to bottom of the water column at times in the far-field (Figure 3.8), suggesting the plume is arriving relatively well mixed to the inner-shelf. When the shear reaches the seafloor, there are low (but detectable) concentrations of freshwater present at the bottom. This happens right at the beginning of the plume in case 1 and appears pulse-like in time. This same pulse-like structure and inhomogeneity is seen in the salinity at the far-field moorings (Figure 3.5d). The salinity oscillates ∼0.5-1 psu (out of a total anomaly of ∼1 psu) on a timescale of roughly 20-45 minutes which suggests this plume is highly variable in space and time (Figure 3.5). Rip currents can have very low-frequency pulsations on the order of 15-30 minutes (Bruneau et al., 2009), which provides a possible explanation for the inhomogeneity observed in case 1; it continually pulses with rip currents out of the surf zone into the far-field creating salinity oscillations of a similar frequency to those of

the rip currents.

This contrasts the southward propagating far-field plume of case 3, which has a well defined maximum shear layer that does not reach the bottom or oscillate in its initial stages (Figure 3.8). The estimated total volume of freshwater in case 1 was 30% that of case 3 (Table 3.1) which could influence these stratification differences. Case 3 plume stratification is stronger and more consistent as the plume propagates past each mooring. This same trend is present in the salinity at the far-field moorings; when the plume arrives, initially the salinity drops, then it maintains a near constant value, and eventually it increases as time goes on, with minimal higher-frequency oscillation (Figure 3.5f). The salinity for the case 3 plume is less variable in time than the case 1 plume in the far-field at O-S1 and O-S2 (Figure 3.8).

The comparison of these two far-field plume structures may provide insight into the potential role of the surf zone or of varied freshwater inputs on plume mixing. Case 1 transports in the SZ-field to the far-field and contains significantly less freshwater by volume than case 3. The primary southward transport for case 3 likely happens on the inner-shelf from a near-and mid-field at the mouth directly, although it is possible the far-field is reached through SZ-field export at any point in the domain. If a plume transports in the surf zone, i.e. has a prominent SZ-field region, and then ejects via rip currents or other surf zone processes (like case 1), it may arrive to the far-field deeper, less concentrated, and well-mixed. Whereas a plume that enters the far-field through a near- and mid-field (possibly case 3) may experience less initial turbulence which could result in a plume that has a more defined plume base and is more horizontally homogeneous in the far-field. Plumes that advect southward from San Dieguito or San Elijo Lagoon could coalesce with LPL's plume in case 1 after $\sim$hr 7 near the estuary, which could have contributed to the inhomogeneous plume structure. While plume coalescence impacts the freshwater budget of a region and can introduce variability in far-field plume properties, the conclusions of this study are valid regardless of the river source.

Differences in plume structure suggest that a plume's fate may be impacted by whether the primary alongshore transport is in the SZ-field or the far-field because of both mixing and transport processes. However in the present study with limited data, we cannot disentangle the variable total freshwater fluxes from the surf zone's influence on far-field plume structure. Therefore, this hypothesized role of the surf zone's impact on overall plume mixing and vertical structure is an area for future research, as is a comprehensive freshwater budget accounting for plume coalescence.

3.7 Conclusions

In this study, we show that the drivers of both small plume formation and transport need to be understood in order to properly predict the fate of small plumes. We illustrate how variable conditions impact whether a plume source region is activated or not depending on the timing of discharge with tidal and wave forcings. Once formed, a plume can enter the surf zone or go directly to the inner-shelf. We show the necessity of understanding a plume's SZ-field, the region impacted by surf zone dynamics, as it can influence not just the near-field plume, but also the far-field transport and eventual fate of small plumes.

To our knowledge, this study is the first observational evidence that small plume transport following a storm can be described by regional waves and winds, and with a direct contribution from the plume's buoyancy. The variability seen in transport across three case studies emphasizes the dynamic nature of these plumes. Differences in the timing, direction, and strength of wind and wave forcings associated with storms can alter a plume's trajectory and eventual fate. This emphasizes the importance of considering the time-evolution of these drivers in order to explain where a plume transports and why. Properly predicting a river regime plume's transport will rely on accurately representing the strength and timing of the winds and waves with respect to the precipitation and discharge.

Acknowledgments

Chapter 3, in full, is a reprint of the material as it appears in *Journal of Geophysical Research: Oceans*: Byrne, S.M.; Giddings, S.N.; Merrifield, M.A.; Horner-Devine, A.R.; Spydell, M.S.; Simpson, A.J.; and O'Reilly, W.C. (2026). Processes impacting the fate of small river plumes following storms. *Journal of Geophysical Research: Oceans*, 131, e2026JC024342. https://doi.org/10.1029/2026JC024342. The dissertation author was the primary investigator and author of this paper.

Thanks to 3 anonymous reviewers and the editor who provided substantial feedback which improved this manuscript. The authors thank the SIO Coastal Processes field crew (B. Woodward, K. Smith, R. Grenzeback, L. Parry, S. Finnerty, and C. Black) for assistance planning and deploying the in-situ instruments, and M. Okihiro for planning and permitting assistance. PiNC was possible thanks to: over 50 volunteers, the Tijuana River National Estuarine Research Reserve (TRNERR), Los Peñasquitos Lagoon Foundation, the City of Del Mar, the City of San Diego, the Torrey Pines Docent Society, and California State Parks. National Science Foundation (NSF) Graduate Research Fellowship Program Grant numbers DGE-2038238 and DGE-2545911 provided support for materials related to this work and for SMB. NSF Award OCE-1924005, provided support for materials related to this work and for SNG and AS. AHD is grateful for funding support from NSF grant number OCE-1923941. Any opinions, findings, and conclusions or recommendations expressed in this material are those of the authors and do not necessarily reflect the views of the National Science Foundation or any other funding institution. MM was funded by California Department of Parks and Recreation, Natural Resources Division Oceanography Program (C19E0026). Complementary measurements were supported by grants from California State Parks and Recreation Natural Resources Division, Oceanography Program (C21820002); the National Estuarine Research Reserve System Science Collaborative; and NOAA's National Centers for Coastal Ocean Science Competitive Research Program.

Finally, inspiration for this work came from our wonderful colleague Nirnimesh Kumar, who left us too early and with whom we would have enjoyed pouring over these observations.

Availability Statement

Data and code from this study are available at https://zenodo.org/records/20516969. Los Peñasquitos streamflow/discharge (Q_{river}) is recorded and made available by the U.S. Geological Survey (USGS, gauge 11023340). LPL estuary water levels are recorded and made available in real time by the Tijuana River National Estuarine Research Reserve (TRNERR, http://torreypines.trnerr.org/) and Los Peñasquitos Lagoon Foundation. Salinity from the Scripps Pier (O-S3) is from the Automated Shore Stations program and made available by the Southern California Coastal Ocean Observing System (SCCOOS, https://thredds.sccoos.org/thredds/catalog/autoss/catalog.html). Salinity from the Del Mar mooring (O100-C) is collected and provided by the Ocean Time-Series Group, http://mooring.ucsd.edu/delmar1/. Offshore water level (tide gauge) and wind measurements are recorded at the Scripps Pier and made available by the National Oceanic and Atmospheric Administration (NOAA) Center for Operational Oceanographic Products and Services (CO-OPS, https://tidesandcurrents.noaa.gov/waterlevels.html?id=9410230) and the National Data Buoy Center (NDBC, https://www.ndbc.noaa.gov/station_history.php?station=ljac1) respectively. Barometric pressure is recorded at the San Diego International Airport and made available by NOAA NDBC (https://www.ndbc.noaa.gov/station_history.php?station=sdbc1). Wave information is from a buoy-driven spectral refraction model, created and made available by the Coastal Data Information Program (CDIP, http://thredds.cdip.ucsd.edu/thredds/catalog/cdip/model/MOP_alongshore/catalog.html). Wave hindcasts used for surf zone current calculations can be found here: https://thredds.cdip.ucsd.edu/thredds/catalog/cdip/model/misc/PiNC/surfzone/catalog.html.

3.A Q^*_{reg} Derivation and Calculation

To estimate Q_{total} and ultimately Q^*_{reg}, we first use an approach based on the assumption of frictional control in the inlet channel to calculate v_{mouth}:

$$v_{mouth} = -g\frac{\Delta\eta}{\Delta x}\frac{h_{sill}}{r} \tag{3.4}$$

where g is gravity, $\Delta\eta$ is the difference in water level between the estuary $\eta_{estuary}$ and the ocean η_{ocean}, Δx is the cross-shore distance between the estuary and ocean measurements, h_{sill} is the water depth at the sill, and r is a linear friction coefficient. The sill is located at or near the estuary mouth. This equation is the result of a depth-averaged momentum balance between a barotropic pressure gradient and linear friction. Water depth at the sill is calculated using $h_{sill} = \eta_{estuary} - d_{sill}$, where the estuary's sill height d_{sill} is found by connecting the lower low water minima of $\eta_{estuary}$ (Harvey et al., 2020). Flow into the estuary is blocked once the offshore tide drops lower than the sill height, creating a disconnect between the estuary and the ocean (Williams, Stacey, 2016). Velocity v_{mouth} is directly proportional to h_{sill} which appropriately causes $v_{mouth} \to 0$ as $h_{sill} \to 0$. Equation 3.4 does not account for hydraulic effects, which are likely present, particularly during high discharge events. This approach follows on the work of Williams, Stacey (2016) and Orescanin, Scooler (2018).

To calculate $\Delta\eta$, $\eta_{estuary}$ is used directly from its source and η_{ocean} is comprised of two parts:

$$\eta_{ocean} = \eta_{tide} + \eta_{wave} \tag{3.5}$$

where η_{tide} is the water level due to barotropic tidal wave propagation measured directly by a nearby tide gauge (7.5-km south of the mouth) and η_{wave} is water level elevation increase due to wave setup (Figure 3.3a). Wave setup is the increase in water level due to breaking waves that generates cross-shore gradients in wave radiation stress (Longuet-Higgins,

Stewart, 1963, 1964; Stockdon et al., 2006). Calculation of η_{wave} from setup follows the Dalinghaus et al. (2022) parametrization $\eta_{wave} = 0.355\beta^{1/2}H_0^{3/4}L_0^{1/4}$ where β is the ocean bottom slope in the surf zone, H_0 is the deep water wave height, and L_0 is the deep water wave length. In this study period, $\beta = 0.014$ according to bathymetric survey measurements from January of 2023 and H_0 and L_0 are time dependent and sourced from the CDIP wave hindcasts computed at 25-m depth for a transect at the estuary mouth (O'Reilly et al., 2016). The Dalinghaus et al. (2022) formula provides the best correlation ($r^2 = 0.65$) to wave setup calculated from in-situ pressure sensors deployed at LPL over the study period (data not shown), improving upon the Stockdon et al. (2006) estimate which had an $r^2 = 0.43$.

The role of friction varies between ebb and flood tide, especially during times of estuary-ocean disconnect once the offshore tide is lower than the sill height and ocean water does not enter the estuary mouth. Our approach estimating velocity across all tidal phases for these bar-built systems adds to the work of Williams, Stacey (2016) and creates one continuous time series of flow that is the result of a pressure gradient-friction balance. This is possible because of the introduction of linear friction with a $\frac{1}{h_{sill}}$ dependence and with a time varying linear friction coefficient (r) that captures the increased frictional effects that occur during ebb tide. While Williams, Stacey (2016) use quadratic friction, linear friction with the above modifications performs just as well on average across the study period. The strength of the frictional coefficients could change across the winter as the estuary dynamically changes to improve $Q_{total,o}$ but there is no clear functional relationship and hence it would not be reproducible without in-situ data. For the sake of simplicity and reproducibility, and because the difference was not statistically significant, we use linear friction with one coefficient for ebb and another for flood tide for this analysis. Linear friction coefficients of $r = 0.0011$ m/s for flood tide and $r = 0.0019$ m/s for ebb tide are found using a linear regression of the estimated and observed velocity. The average of the flood and ebb r (0.0015) is close to the linear friction coefficient $r = 0.0016$ m/s used

by Whitney et al. (2014) in their work in the eastern Long Island Sound, a large estuary with a large sill.

The estimate of v_{mouth} is turned into Q_{total} (total volume transport between the LIE and the ocean) by:

$$Q_{total} = A_{mouth} v_{mouth} \tag{3.6}$$

where A_{mouth} is the time-varying mouth cross sectional area calculated as $A_{mouth} = h_{sill} * b_{mouth}$, where b_{mouth} is the width of the mouth and is taken as a constant. It is worth noting that while the maximum estuary mouth width is fixed (constrained by a bridge), the actual estuary width near the mouth does change over the tidal cycle and throughout our observational period due to morphological changes, however not in a predictable manner. Moreover, h_{sill} is not representative of the cross-sectionally changing water depth. Thus, this simplification in the calculation of A_{mouth} (both in h_{sill} and b_{mouth}) is likely a source of error in this calculation.

For validation and comparison, the observed $Q_{total,o}$ is calculated as $A_{mouth} v_{mouth,o}$. Observed estuarine velocity (mooring E-C), $\bar{v}_e$, is adjusted to represent the velocity at the sill by assuming that discharge at E-C is equal to discharge at the mouth: $v_{mouth,o} = \bar{v}_e \frac{h_{EC} b_{EC}}{h_{sill} b_{sill}}$ where h_{EC} and b_{EC} is the water depth and width respectively at E-C. As with near the mouth, h_{EC} is time varying while b_{EC} is fixed, although a fixed b_{EC} is more reasonable at E-C where the channel is closer to rectangular and experiences minimal morphological changes. Comparison of Q_{total} with $Q_{total,o}$ gives a statistically significant correlation $r^2 = 0.61$ with $RMSE = 8.75$ m^3/s (Figure 3.3c). The inclusion of wave setup slightly improved the correlation and RMSE of the calculated Q_{total} to the observed $Q_{total,o}$ and greatly reduced the mean offset between η_{ocean} and $\eta_{estuary}$ from 0.2 m to 0.06 m.

Q_{river} (Figure 3.3b) is measured upstream of tidal influence and represents only the freshwater input due to river flow. For this parameter calculation, an average lag of 5.2 hrs is applied to Q_{river} to match when river discharge measured at the gauge reaches the

estuary. This lag is determined by taking the average time between the initial arrival of the 3 cases between Q_{river} upstream and $\bar{v}_e$ at mooring E-C. The true lag time changes by multiple hours between events and reflects the complex hydrology impacting the freshwater arrival to the estuary from its upstream sources.

We expect that Q^*_{reg} could be useful for other estuarine dynamics of interest such as mouth sediment accretion/erosion and possibly stratification. Similar approaches have been used to investigate sediment erosion/accretion at LIE mouths with sills that can experience mouth closure (Orescanin, Scooler, 2018). Our approach is similar to Orescanin, Scooler (2018); however, we use a linear friction $\sim$ pressure gradient balance (Williams, Stacey, 2016) to find volume transport at the mouth. We also use a wave setup parametrization to find $\Delta\eta_{wave}$ and add the wave contribution to the volume transport. These approaches could be compared and evaluated for their use in finding drivers of sill erosion/accretion, including identifying mouth closures and breaches. This approach can be calculated in near real-time, meaning Q^*_{reg} could be used almost predictively to find the start time of beach water quality alerts when the plume source region activates as the system transitions into the river regime, or with ebb tide in the tidal regime.

3.B Supplementary Information

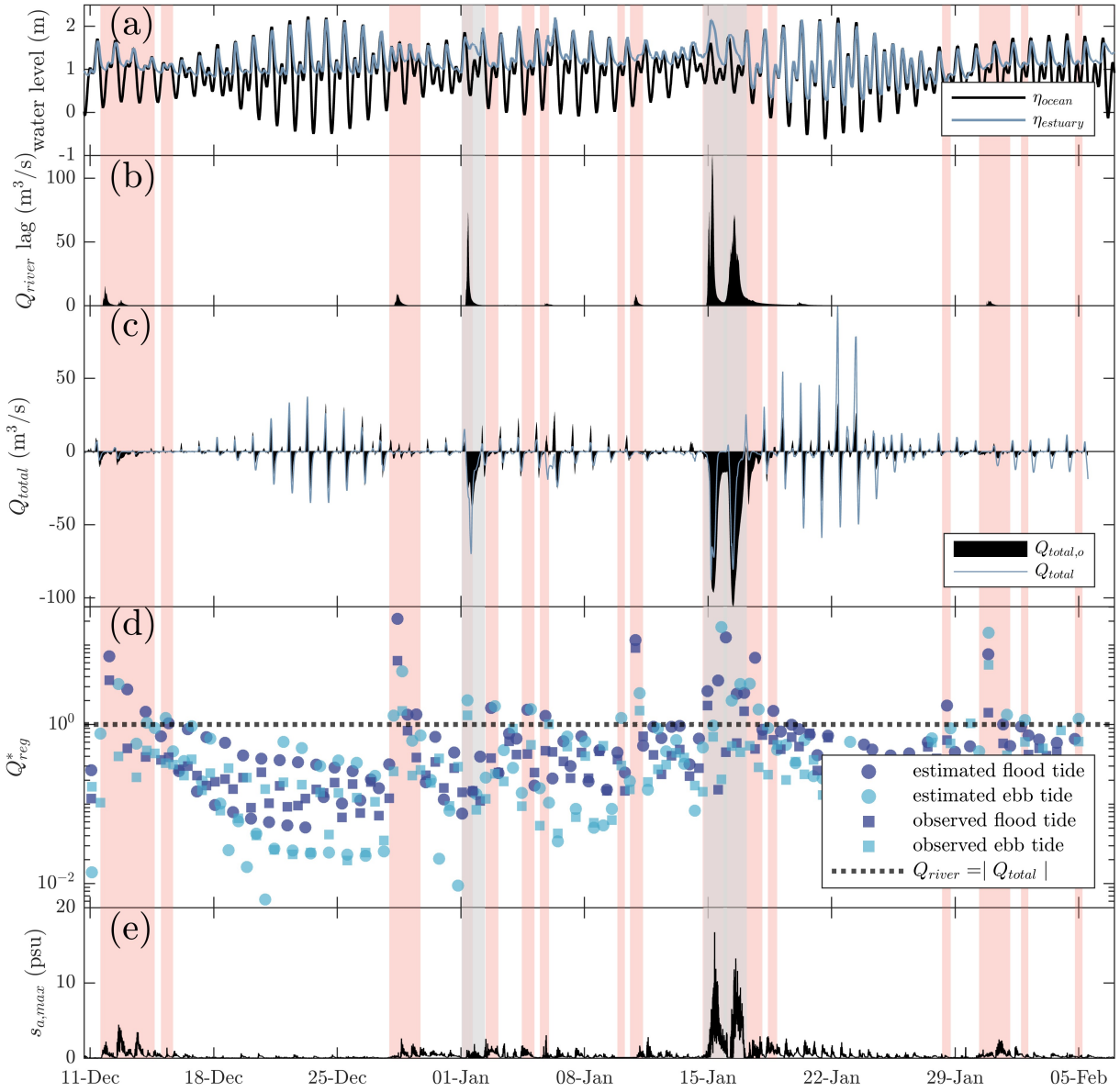


Figure 3.B.1. (a) Water level in the ocean (η_{ocean} in black) and estuary ($\eta_{estuary}$ in gray). (b) Q_{river}, with y-axis in log scale, lagged by 5.2 hrs to better match when river discharge measured at the gauge reaches the estuary. (c) Q_{total} estimate is shown with a gray line and $Q_{total,o}$ is shown in black shading. (d) Q^*_{reg}, y-axis in log scale, averaged over each ebb (light blue) and flood tide (dark blue). The dashed black line is $Q^*_{reg} = 1$ where $Q_{river} = |Q_{total}|$. Circles show Q^*_{reg} as in main text using $|Q_{total}|$, whereas squares show Q^*_{reg} calculated with $|Q_{total,o}|$. (e) Maximum salinity deficit between the freshest surface salinity from any 'O-' moorings and O-S3's near-surface salinity ($s_{a,max}$). Instances where $Q^*_{reg} \geq 1$ (using $|Q_{total}|$) are shaded in pink across all panels. Cases 1-3 are shaded across panels in light gray.

Chapter 4

Surf zone influence on inter-estuary connectivity and river plume coalescence from low-inflow estuaries

4.1 Introduction

Terrestrial freshwater influences ecological and biogeochemical processes in estuaries and in the ocean, through river plumes, by carrying dissolved and particulate matter, debris, sediment, larvae, nutrients, and pollutants (Garvine, 1974; Grant et al., 2005; Syed et al., 2010). This outflow can shape coastal ecosystems, from the surf zone to regions kilometers offshore (Vargas-Fonseca et al., 2016; Roegner et al., 2002; Swieca et al., 2020). For example, the Columbia River plume has increased prey fish concentrations compared to surrounding offshore waters (Swieca et al., 2020). Even near smaller rivers, estuaries and their river plumes can impact coastal biology. For example, one study shows that the distance between a surf zone location and the nearest estuary has a greater impact than the wave conditions or degree of urbanization on the distribution of fish species in the surf zone (Vargas-Fonseca et al., 2016). There is also evidence of larvae accumulation in the Maipo River plume front, impacting the species distribution in the nearshore (Vargas et al., 2006). Small rivers in southern California have been shown to influence nutrients and alkalinity in the coastal ocean (Paulsen et al., 2018; Howard et al., 2014; Ho et al.,

2023). Thus, understanding these connective pathways between estuaries and the coastal ocean is critical for informing sediment, nutrient, larval, and pollutant transport in the coastal regions.

Small estuaries and their outflow are understudied compared to large ones, despite their ability to host important ecosystems, and their significant influence on coastal ocean hydrodynamics, geomorphology, and biogeochemistry (Milliman, Syvitski, 1992; Warrick, Fong, 2004; Wetz et al., 2006; Sutula et al., 2021). Here we are specifically investigating small low-inflow estuaries (LIEs) (Largier, 2023) which occur globally in Mediterranean climates with highly variable and infrequent rainfall, including the study region in southern California, USA (Dettinger et al., 2011; Largier, 2023; McSweeney et al., 2017). Intermittently closed estuaries (ICEs) (Williams, Stacey, 2016; McSweeney et al., 2017; Harvey et al., 2023) are a subset of LIEs which are defined by intermittent disconnection of the estuary with the ocean due to sediment accretion at the mouth (Williams, Stacey, 2016; Orescanin, Scooler, 2018; Harvey et al., 2023). The study region contains three estuaries that are considered both LIEs and ICEs (Harvey et al., 2023). While these small, low-inflow estuaries have an important but spatially and temporally limited impact on the coastal ocean, multiple small rivers can collectively impact a greater cumulative ocean area when measured against a single large river of comparable watershed size (Warrick, Fong, 2004; Mazzini et al., 2014). Thus, understanding the transport, mixing, and fate of small river plumes from these systems collectively is critical to understanding an important source of freshwater flux into the ocean.

In regions with multiple small rivers, the interaction of different plumes is more common than in larger river watersheds (Warrick, Farnsworth, 2017). This is referred to as plume coalescence, and it can alter the fate of coastal plumes (Warrick, Farnsworth, 2017; Saldías et al., 2012; Salcedo-Castro et al., 2020; Rosa et al., 2022; Vundavilli et al., 2024; Collins, Macdonald, 2025). Inner-shelf plume coalescence in small plumes can occur when direct wind forcing drives adjacent plumes to intersect (Vundavilli et al., 2024; Romero

et al., 2016). In larger plumes, wind impacts are often rotational such that plumes will transport in the Coriolis deflected wind direction (Geyer et al., 2000; Fong, Geyer, 2001), as opposed to small plumes that transport in the direction of wind forcing directly (Warrick et al., 2007; Osadchiev et al., 2021; Basdurak, Largier, 2022; Lemos et al., 2022; Vundavilli et al., 2024; Byrne et al., 2026). Thus, the drivers of inner-shelf plume coalescence vary with the sizes of the plumes involved. Warrick, Farnsworth (2017) outline scenarios where unique hydrologic, geographic, or oceanographic conditions can increase the chances of plume coalescence. These include coastlines with angled inflow, irregular river mouth spacing, rotational plumes, wind or currents, and variable watershed sizes. In this study, we introduce the surf zone as a new pathway by which there can be plume coalescence that alters plume fate.

River plumes can transport alongshore and consequently intrude into adjacent estuaries (Roegner et al., 2002; Wong, Lu, 1994; Sousa et al., 2014; Iglesias et al., 2024). This connectivity between estuaries specifically occurs in large river systems with consistently strong outflow (100-1000+ m^3/s) and smaller neighboring estuaries, such as the Columbia River plume intruding into nearby estuaries (Roegner et al., 2002; Banas et al., 2004; Giddings, MacCready, 2017), the Minho River plume intruding into the Rias Baixas (Sousa et al., 2014; Des et al., 2019), the Douro Estuary plume intruding into the Ave Estuary (Iglesias et al., 2024), and the Delaware River plume intruding into the Indian River Inlet (Wong, Lu, 1994), but this has not been documented on coastlines with only low-inflow estuaries. River plumes, in both large and small rivers, can contain elevated levels of larvae and plankton (Vargas et al., 2006; Axler et al., 2020), nutrients, etc. Thus, plume intrusion into an adjacent estuary can have implications on the transport of one estuary's biota, nutrients, sediment, or pollutants to an adjacent estuary (Roegner et al., 2002). In this study, we show that there can be plume intrusion in small LIEs from adjacent LIEs and elucidate the conditions that drive this inter-estuary connectivity.

Small river plume transport also differs dynamically from that of large plumes

because of the influences of the surf zone (Garvine, 1995; Wong et al., 2013; Horner-Devine et al., 2015). A small plume discharging into the ocean can be retained within the surf zone if the onshore-directed wave momentum is stronger than the offshore-directed river momentum (Wong et al., 2013; Rodriguez et al., 2018; Kastner et al., 2019; Lou et al., 2025). This differs from large river plumes that are mainly unaffected by surf zone processes, often outflowing farther offshore than the surf zone (Hickey et al., 1998). Large plumes have been more rigorously studied than small plumes, and only recent literature is beginning to investigate the transport and fate of small plumes (Wong et al., 2013; Rodriguez et al., 2018; Kastner et al., 2019; Osadchiev et al., 2021; Basdurak et al., 2020; Basdurak, Largier, 2022; Lou et al., 2025; Byrne et al., 2026). While our understanding of near-field processes is increasing, there remains a gap in understanding the fate of surf zone plumes. Recent observations find that the surf zone can transport plumes multiple kilometers alongshore and then export them to the inner-shelf (Byrne et al., 2026), but the exact pathways for this are largely unexplored. Bathymetric rip currents are one mechanism for cross-shore transport of a surf zone plume to the inner-shelf (Kumar, Feddersen, 2017; Bruneau et al., 2009; Moulton et al., 2017; Lou, 2025). In the present study, we introduce another mechanism where surf zone plume export occurs due to the interaction with an adjacent estuary.

In this work, we explore both the role of the surf zone on estuary and plume connectivity, and the role of adjacent estuaries on altering the transport and fate of far-field surf zone plumes. We use 14 months of output from a two-way coupled ocean and wave model to investigate dynamics that are difficult to measure observationally due to the temporally and spatially-varying nature of both the surf zone and of river plumes from LIEs. We show that the surf zone plays a role in plume coalescence and in establishing inter-estuary connectivity in small plumes. Further, we explain how the fate of a surf zone plume is altered by the presence of an adjacent estuary mouth during both flood and ebb tide by either pumping the plume inside the estuary or by forcing the surf

zone plume offshore at the mouth. The model used and relevant methods are detailed in Section 4.2. The full record's spatial and temporal trends in plume impact (Section 4.3.1) and plume coalescence (Section 4.3.2) are explored in detail. Next, two types of surf zone coalescence behaviors near estuary mouths are described in Section 4.3.3. Then, the cross-shore structure of a surf zone and inner-shelf plume in the far-field following surf zone coalescence are presented in Section 4.3.4. Lastly, the occurrence and behavior of a plume intruding into an adjacent estuary is shown in Section 4.3.5. The results are synthesized and contextualized in the discussion sections that follow. The role of the surf zone in plume coalescence is discussed in Section 4.4.1, followed by implications of results on far-field surf zone plume interactions (Section 4.4.2). Then the importance of the surf zone for connecting adjacent estuaries is discussed in Section 4.4.3. Implication for coastal water quality are explored in Section 4.4.4. Conclusions are given in Section 4.5.

4.2 Materials and Methods

4.2.1 Numerical Model

Here we employ a high resolution, realistic, 3D regional ocean numerical simulation which telescopes inward via nested grids from the Southern California Bight to very fine resolution in order to resolve small LIEs and the surfzone focusing on the coastal region around Los Peñasquitos Lagoon (LPL) in San Diego, CA (Figure 4.1). The three parent grids (LV1, LV2, and LV3) use the Regional Ocean Modeling System (ROMS) to simulate ocean circulation (Shchepetkin, McWilliams, 2005) with spatial resolution that varies from 2 km to 600 m and then 200 m respectively (Figure 4.1a). The parent run set-up is described in Wu et al. (2020) and Pan et al. (2025). The highest resolution LV4 run, the focus of this study, includes surface gravity waves through a coupling of ROMS with the Simulating Waves Nearshore model (SWAN, Booij et al. (1999)) via the Coupled Ocean-Atmosphere-Wave-Sediment-Transport modeling system (Kumar et al.,

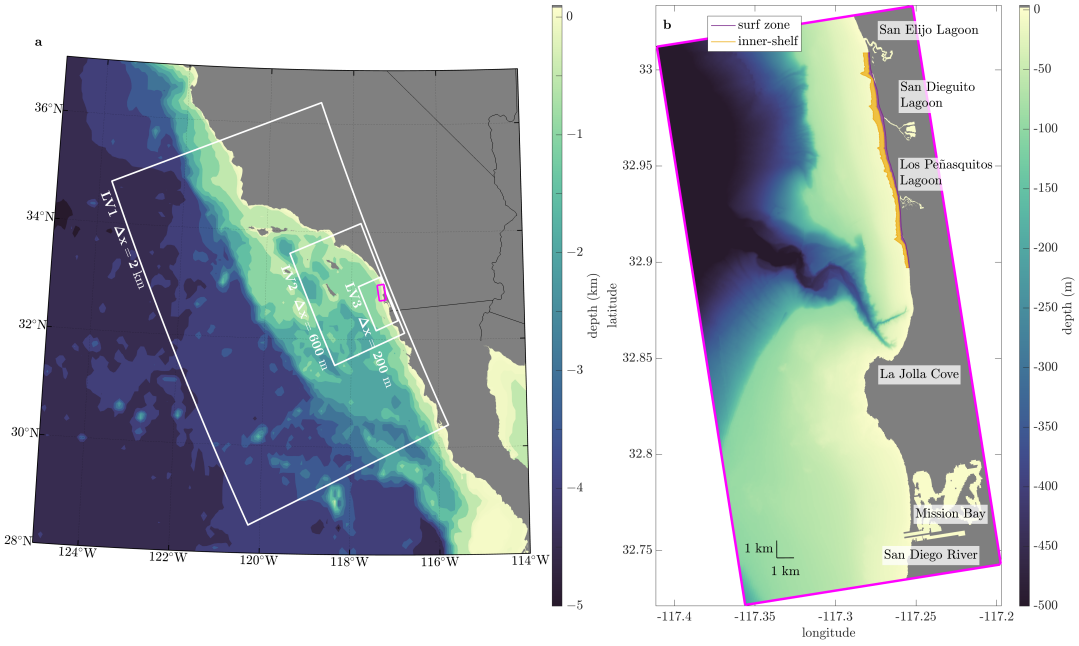


Figure 4.1. (a) COAWST model domains for LVs 1-3 in white boxes and LV4 in pink box. (b) Zoomed in LV4 domain, with labeled features and contoured bathymetry. Example surf zone (purple) and inner-shelf (yellow) boxes, that are used in the percent plume area calculations presented in Section 4.3.1, are illustrated here for June 10, 2019 at 5:00 UTC. Note the different colorbars between (a) and (b).

2012; Warner et al., 2010). LV4 is a stretched grid with the highest resolution (<8m) focused near LPL stretching out to ∼110m at the offshore domain edges (Figure 4.1b). Due to this stretched grid, this study will focus primarily on processes occurring near LPL where the resolution is the highest. The details of the LV4 run are described in Pan et al. (2025) with some key highlights included below.

LV4 is two-way coupled with ROMS and SWAN at a 12 minute interval; SWAN receives ocean currents and water levels from ROMS, and ROMS receives wave-modified currents from SWAN due to the simulated surf zone vortex force and wave breaking within SWAN (Pan et al., 2025). The LV4 grid has 15 vertical s levels with enhanced resolution near the surface and the bed to capture plumes and the bottom boundary layer. The run spans June 1, 2019 through September 29, 2020 with hourly output. SWAN simulates wave conditions for 25 frequencies between 0.04 and 0.29 Hz, including wind wave generation, using boundary conditions provided by the Coastal Data Information Program's (CDIP) wave spectra model (O'Reilly et al., 2016). The open ocean boundary forcing for LV1 (including tides) and the atmospheric forcing for all levels is described in Pan et al. (2025).

Freshwater enters into the LV4 domain in 6 locations. This includes San Elijo Lagoon (SEL), San Dieguito Lagoon (SDL), Los Peñasquitos Lagoon (LPL), Mission Bay through Tecolote Creek and Rose Creek, and the San Diego River (SDR), listed from north to south (Figure 4.1b). The timing and strength of river discharge is the only difference in LV4 runs between the present study and Pan et al. (2025). River discharge (Q_{river}) from upstream river gauges are retrieved for SDR, LPL, SDL, and SEL, and scaled by a ratio of the watershed area downstream of gauge compared to the total watershed area. Q_{river} ranges from 0 to 150 m^3/s, where positive represents freshwater flow into the estuary. Values over 150 m^3/s, which only occurs once in two of the six rivers, is re-distributed over a longer period of time to avoid numeric instability. Tecolote and Rose Creek are ungauged so the SDR Q_{river} is scaled down to their respective watershed sizes to represent their discharge. SDL's incoming Q_{river} is complicated by the presence of the Lake Hodges

dam upstream. The total discharge received in SDL is a combination of watershed-scaled discharge from the Santa Maria river, the dam's regular leakage, event blow-offs, and prolonged water releases (see Availability Statement for data sources). Passive dye tracers are input for LPL (dye 1), SDL (dye 2), and SEL (dye 3) at the location of river input with an initial concentration of 1. The dyes are used in this analysis to differentiate freshwater sources.

Prior studies have validated these numerical simulations for LVs 1-3 (Wu et al., 2020) and for LV4 (Pan et al., 2025). For the LV4 run with the same wave and atmospheric forcings as ours in Pan et al. (2025), the SWAN wave height, period, and direction match bulk wave parameters well with root-mean-square error of 0.1 m, 1.7 s, and 9° respectively. ROMS modeled ocean conditions match the ocean tides at the Del Mar Mooring located at the 100-m isobath offshore of LPL (Pan et al., 2025). Compared with observations at this mooring, the near-surface and sub-surface sub-inertial velocities are weaker. The model's semi-diurnal velocity shows similar values but the diurnal velocity is much weaker (Pan et al., 2025). Lastly, the modeled buoyancy frequency (N^2) agrees well with the mooring at the surface, but is less temporally-variable and is only $\sim 80\%$ of the observed values at depth (Pan et al., 2025). The validation from Pan et al. (2025) is applicable to the current study because the two model runs are executed identically, with the exception of river outflow. The river plumes in these model runs do not reach the 100-m isobath where this validation mooring is located, thus the validation performed in Pan et al. (2025) is applicable here. Model runs in a similar LV4 domain focused on the Tijuana River Estuary nested within the same LV1-3 parent grids, and with the same wave coupling and scaled horizontal resolution, have been validated and utilized in numerous studies lending further support to this modeling approach (Wu et al., 2020, 2021a,b,c; Feddersen et al., 2021).

4.2.2 Coordinate Systems and Velocity

The LV4 grid has coordinates of (ξ, η), and the grid itself is angled $\sim 9°$ from true north. To get alongshore and cross-shore velocities, average local shoreline angles are calculated. All horizontal velocities presented in this study are alongshore (v) or cross-shore (u) and have been rotated from (ξ, η) to a shorenormal coordinate system ($+x$, pointing onshore, and $+y$, 90° counterclockwise of that) at each respective location. All cross-shore (u) velocities are Lagrangian and include both the Eulerian cross-shore velocity and the Stokes velocity, both rotated to shorenormal, which drives a surface-intensified flow due to waves (Kumar et al., 2012). Cross-shore (u) velocity is positive onshore and alongshore velocity (v) is positive 90° northward of u. Surface cross-shore and alongshore velocities are reported as u_{sfc} and v_{sfc}, and depth averaged velocities are reported as $\bar{u}$ and $\bar{v}$. If quantities are with respect to shorenormal, they will be referred to as cross-shore, but if values are taken along one η value spanning multiple ξ values they will be referred to as grid line transects. The grid line transects presented are not expected to differ notably from cross-shore transects at the same given location because η is within $\sim 10°$ of shorenormal in the focused study region. Note, because η is later used to describe sea surface height, we will refer to the (ξ, η) grid coordinates as (x, y) for the remainder of this paper.

4.2.3 Stratification

Stratification is inferred following the buoyancy frequency squared. This is calculated as: $N^2 = -\frac{g}{\rho_0}\frac{d\rho}{dz}$ where g is gravitational acceleration, ρ_0 is reference density, and $\frac{d\rho}{dz}$ is the density gradient (ρ) with depth (z). The N^2 presented here is calculated using the density gradient between the top and bottom of the water column.

4.2.4 Surf Zone Quantities

The maximum wave height at each grid line in the domain in the nearshore region is used to identify the surf zone's offshore edge for each time step. The surf zone length (L_{SZ}) is found as the distance between the surf zone edge and the shoreline location, the last water cell along the grid line before the land mask applies. Wave quantities are computed at each model run time step to force the physics; bulk properties are saved hourly while other quantities are not saved to output. Wave radiation stresses reported in this study are recalculated with bulk values using the following formulas. The cross-shore wave radiation stress (S_{xx}) is the onshore-directed depth-integrated wave momentum calculated as $S_{xx} = E\left[n\left(\cos^2\theta + 1\right) - \frac{1}{2}\right]$ and is reported in units of m^2 after dividing by density times gravity (ρg) (Longuet-Higgins, Stewart, 1964). Wave direction (θ) is relative to the shore normal, and wave energy (E) divided by ρg is $E = \frac{1}{16}H_s^2$ where H_S is significant wave height (Feddersen, 2004). The ratio of group speed to phase speed is $n = \frac{1}{2}\left(1 + \frac{2kh}{\sinh(2kh)}\right)$, where h is water depth and k is wavenumber (Longuet-Higgins, Stewart, 1964; Longuet-Higgins, 1970). The along-shore wave radiation stress (S_{xy}) is the shear component of the wave momentum calculated as $S_{xy} = E \cdot n \sin\theta \cos\theta$.

The cross-shore gradient of S_{xy} drives alongshore surf zone currents important for plume transport (Thornton, Guza, 1986; Guza et al., 1986; Rodriguez et al., 2018). Surf zone currents in the model are calculated with full directional wave information (Kumar et al., 2012). Comparing the maximum modeled surf zone currents in this work with near-wave breaking surf zone currents calculated following the simplified physics approach in Byrne et al. (2026) for the same time as model output shows decent agreement but with lower extreme values in this model (Supplemental Figure 4.11). The wave conditions in Byrne et al. (2026) range to higher wave heights than those seen in the modeled time frame in this study, adding to the difference in surf zone current magnitude between these studies. A similar comparison that investigates average surf zone currents compared to

the COAWST model shows good agreement in a 1D perspective (Brasseale et al., 2023).

4.2.5 Estuary Volume Transport (Q_{mouth})

The volume transport in and out of an estuary's mouth is calculated as

$$Q_{\text{mouth}}(t) = \iint_{A(t)} u_x(y,z,t)\,dA = \int_{y_1}^{y_2}\int_{-h(y)}^{\eta(y,t)} u_x(y,z,t)\,dz\,dy \tag{4.1}$$

where here u_x is velocity in the x direction which is coincidentally normal to the estuary mouths, and A is the mouth's cross-sectional area which is evaluated between two y grid points (y_1 and y_2) and the full water column from $-z$ to η. Outflow from the estuary to the ocean is denoted as negative Q_{mouth} in line with the ocean velocities that are also negative moving offshore.

4.2.6 Dye as a Plume Tracer

Three passive dye tracers are used to track the relative contribution of three adjacent estuaries to the observed freshwater content. Dye 1 is from LPL, dye 2 is from SDL, and dye 3 is from SEL with concentrations C_1, C_2, and C_3 respectively. If total dye concentration ($C = C_1 + C_2 + C_3$) equals one in a grid cell then it is entirely freshwater, if it equals zero then it is entirely saltwater. This is because the contribution of freshwater from sources other than the three estuaries is minimal to the region of interest (north of La Jolla Cove, see Figure 4.1). We consider a plume to be present at a location when the water properties are $\leq$99% their background value, which is when any dye has $C \geq 0.01$. Plume coalescence is identified when any grid cell has more than one dye (i.e. more than one river source) with $C \geq 0.01$ at a given time. Note that $C \geq 0.01$ is equivalent to a freshwater fraction, $F = (S_o - S)/S_o$, of $F \geq 0.01$ where S is salinity and S_o is background salinity (Nash et al., 2009). We use C instead of F in the following analysis to enable comparison between river sources.

To compare different location's dye content we calculate the depth-integrated dye content (C') and the surface average dye content (C_{sfc}). First, the threshold of $C \geq 0.01$ is applied to each respective dye. C' is calculated as the depth integral of dye from the static sea floor location ($-h$) to the oscillating free surface (η) that includes ocean and wave influences

$$C'(x,y,t) = \int_{-h(x,y)}^{\eta(x,y,t)} C(x,y,z,t)\, dz \tag{4.2}$$

and surface dye concentration (C_{sfc}) is calculated in the upper 1-m (Δz_{sfc}) of the water column as

$$C_{sfc}(x,y,t) = \frac{1}{\Delta z_{sfc}} \int_{\eta(x,y,t)-\Delta z_{sfc}}^{\eta(x,y,t)} C(x,y,z,t)\, dz\ . \tag{4.3}$$

When more than one dye is present in a given cell, each dye has the 1% threshold applied independently, and then the respective concentrations are added together ($C_1 + C_2 + C_3$) before they are integrated to get C' and C_{sfc}. To investigate each plume separately, these same calculations are followed instead using either C_1, C_2, or C_3 in place of the total dye content C. These produce C_1' and C_{1sfc} for dye 1, C_2' and C_{2sfc} for dye 2, and C_3' and C_{3sfc} for dye 3. We use C' as a proxy for freshwater content, and C_1', C_2', and C_3' to look at the relative contributions of each river source. Note that C' has units of kg/m^2 whereas C_{sfc} has units kg/m^3. However, the concentration and total freshwater content in the upper 1-m are mathematically identical such that C_{sfc} can refer to a concentration or total plume content in units of kg/m^2 or kg/m^3.

To find a percent plume coverage, a focused subdomain is selected that spans from 4-km north of SDL to 4-km south of LPL (see example in Figure 4.1b). One box bounds the surf zone between the shoreline and surf zone edge. The inner-shelf box is bounded by the surf zone edge to 2 additional L_{SZ} offshore. Percent plume coverage is computed by the horizontal area within the surf zone or inner-shelf that a plume is present at or above the 1% threshold at any depth, compared to the total horizontal box area.

Areas with active mixing of two plumes can be distinguished from areas with mixed

plumes using methods derived in Li et al. (2026). The present study's approach investigates when and where coalescence occurs using a binary system, but future work should apply the Li et al. (2026) methods to investigate patterns in production and mixing extent.

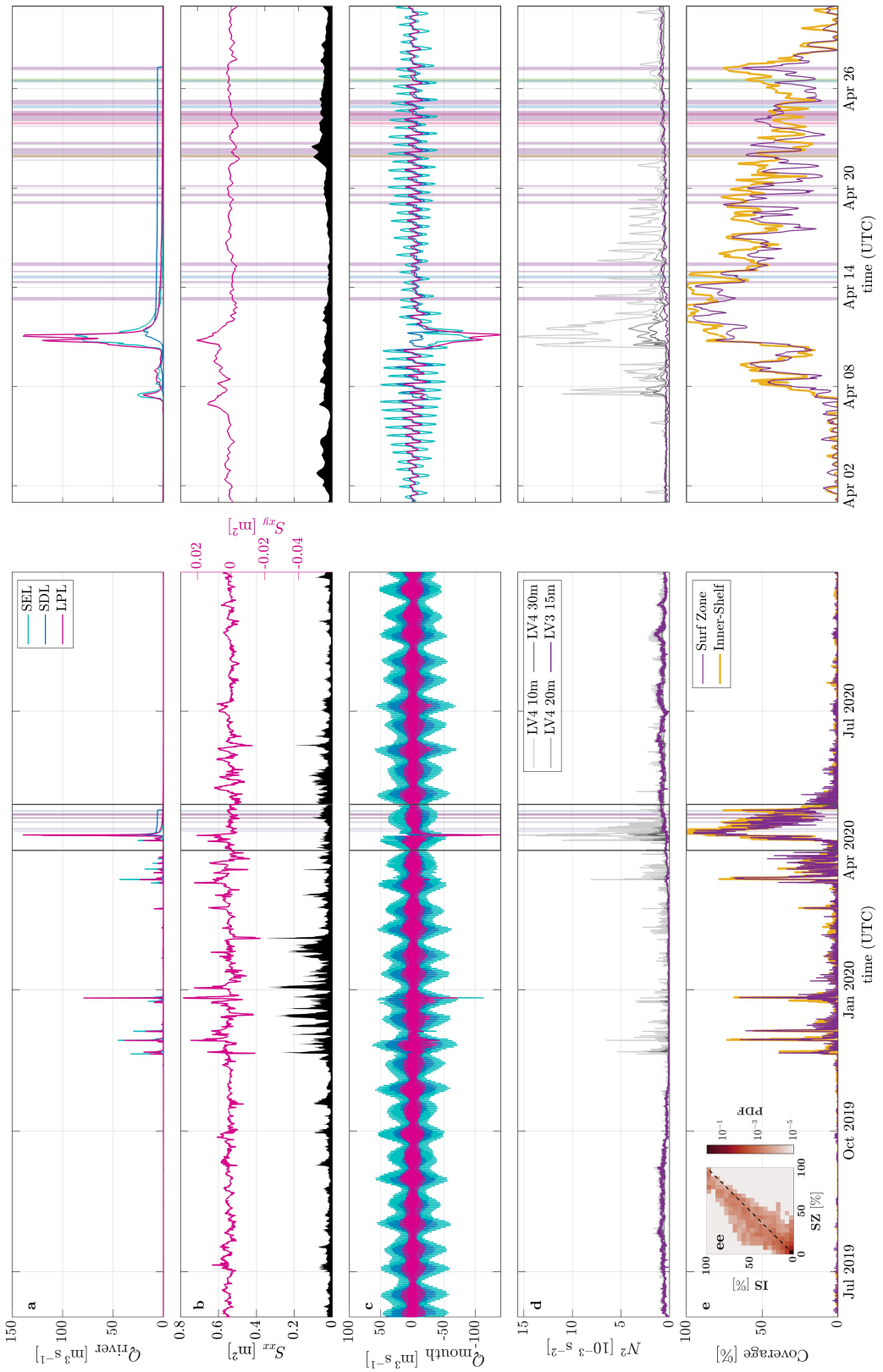
4.2.7 In-Estuary Plume Extent

The distance an incoming plume travels into LPL is found by taking a manual transect through the main channel and the side channel (see Figure 4.8a). Any time an adjacent estuary's dye is present in LPL, it begins the start of a plume intrusion event. The distance the plume travels in-estuary is the farthest upstream point, at any depth, where incoming dye C is greater than or equal to the 1% threshold.

4.3 Results

4.3.1 Freshwater Input to the Ocean

Figure 4.2. 14-months of model results showing (a) upstream discharge (Q_{river}) and (c) discharge at the mouth (Q_{mouth}) for Los Peñasquitos Lagoon (pink), San Dieguito Lagoon (blue), and San Elijo Lagoon (cyan), (b) onshore (S_{xx}, black fill) and alongshore (S_{xy}, pink line) wave radiation stress offshore of Los Peñasquitos Lagoon, (d) stratification (N^2) near the 15-m isobath offshore of LPL in LV3 with no rivers (purple), and for LV4 with rivers at the 10-m, 20-m, and 30-m isobaths (darker shades of gray farther offshore), (e) plume area coverage in the surf zone (purple) and the inner-shelf (yellow) with inset subpanel (ee) showing the joint probability density function of surf zone vs. inner-shelf plume coverage. The cross-panel shading highlights events discussed in future sections including surf zone coalescence continuation (pink) and export (blue) cases (see Section 4.3.3), far-field sample events that follow surf zone coalescence (green; see Section 4.3.4), and estuary intrusion events into LPL (purple; see Section 4.3.5). The right column displays a zoom-in of April 2020, indicated by the gray box in the left column.


a
b
c
d
e
SEL
SDL
LPL
Q_{river} [m^3 s^{-1}]
S_{xx} [m^2]
S_{xy} [m^2]
Q_{mouth} [m^3 s^{-1}]
N^2 [10^{-3} s^{-2}]
LV4 10m
LV4 20m
LV4 30m
LV3 15m
Surf Zone
Inner-Shelf
Coverage [%]
IS [%]
SZ [%]
ee
PDF
Jul 2019
Oct 2019
Jan 2020
Apr 2020
Jul 2020
time (UTC)
Apr 02
Apr 08
Apr 14
Apr 20
Apr 26
time (UTC)

Temporal Trends

Over the 14-months of model simulation, each of the three watersheds have similar, but slightly varied, incoming river discharge (Q_{river}; Figure 4.2a). The study region has the largest waves, and the strongest cross-shore wave radiation stress (S_{xx}) in winter from November to February (Figure 4.2b). The alongshore wave radiation stress (S_{xy}) at the LPL mouth has the strongest values in winter and switches directions between promoting northward ($S_{xy} > 0$) and southward ($S_{xy} < 0$) surf zone currents (Figure 4.2b). All three estuaries have elevated incoming Q_{river} and stronger outflowing Q_{mouth} following rain events (Figure 4.2c). The average incoming river discharge (Q_{river}) is 0.61, 0.28, and 0.54 m^3/s for LPL, SDL, and SEL respectively. SDL receives elevated Q_{river} and discharge out of the estuary mouth (positive values of Q_{river} and negative values of Q_{mouth}, Figure 4.2c) in April due to increased discharge from an upstream dam.

River plumes form on every ebb tide or following heavy precipitation events ($Q_{mouth} < 0$ when Q_{river} spikes), and cease formation on flood tides when $Q_{mouth} \geq 0$ (Figure 4.2a,c). As described in Byrne et al. (2026), small plume formation follows two regimes, a tidal plume regime where outflow ($Q_{mouth} < 0$) occurs only on ebb tides during low discharge conditions, and a river-driven plume regime where outflow can persist across one or more tidal cycles when river discharge is large enough. During this study period, there are a few times when the mouth transitions to the persistent storm-driven plume regime, but more frequently it is in the tidal plume regime (right column of Figure 4.2c).

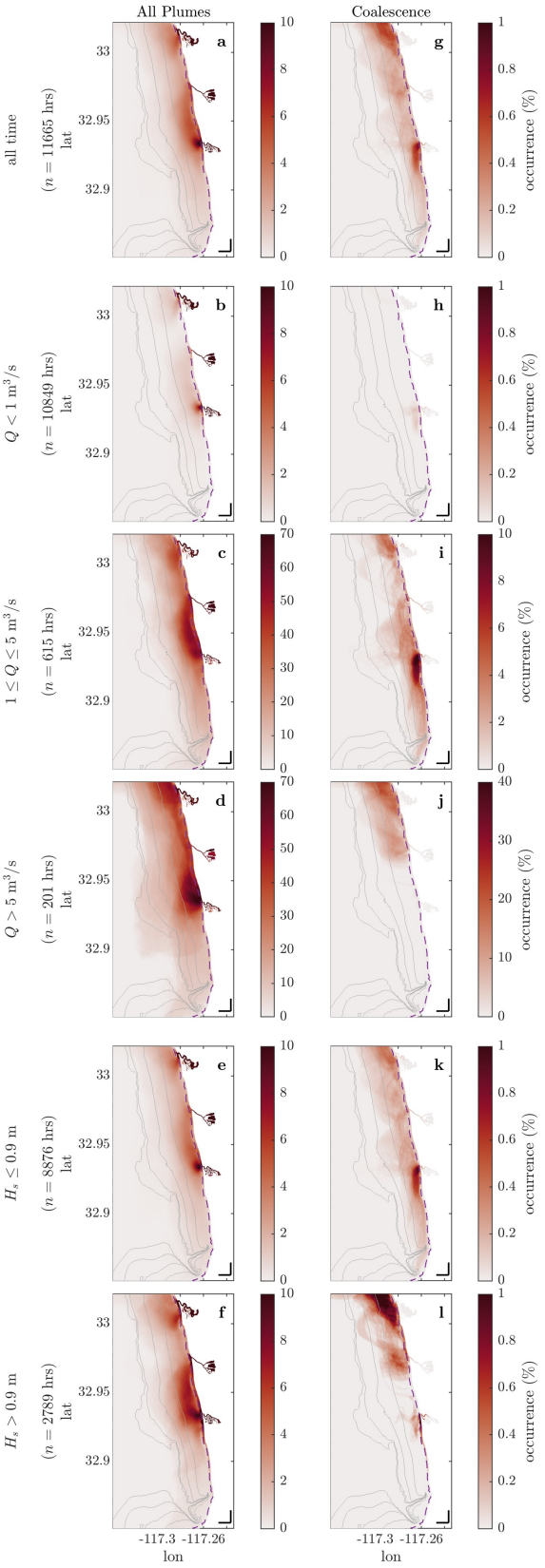
Inner-shelf stratification is higher due to river plumes in winter and spring (Figure 4.2d), although there is significant spatial variation. In the coarser LV3 parent grid, which has no river freshwater input, the inner-shelf N^2 ranges from 2.3×10^{-5} to 1.6×10^{-3} s^{-2} and follows a seasonal cycle with maximum values in summer (July to August) and minimum in winter (December to January) (Figure 4.2d). The river freshwater inputs in LV4 alter this cycle. While the summer N^2 in LV3 and LV4 follow closely, they diverge significantly

in the winter rainy season in accordance with the Q_{river}. Surface intensified low-density river plumes cause the inner-shelf stratification to increase to values up 1.4×10^{-2} s^{-2} during the otherwise low-to-moderate stratification seasons. The elevated stratification returns to base level (that of LV3) after the plumes mix out (Figure 4.2d). The impacts of river plumes on stratification are highest near the coast and near the estuary mouth where plumes are most common; impacts decrease with distance offshore (Figure 4.2d). Despite this offshore decay, events that occur in quick succession reach a more stratified shelf, whereas the first events after longer breaks in outflow events propagate into less stratified background conditions. This has implications for plume transport and mixing because they depend on vertical and horizontal density gradients.

Percent plume coverage highlights how much area a plume occupies within a subregion of this domain that spans from 4-km north of SDL to 4-km south of LPL in the surf zone and on the inner-shelf (shown for an example time in Figure 4.1b). Plumes occupy anywhere between 0 to 100% of the inner-shelf and 0 to 96% of the surf zone, with averages at 3.6 and 3.7% respectively (Figure 4.2e). After Q_{river} spikes following rain events, the percent plume coverage increases in both the surf zone and inner-shelf (Figure 4.2e). Following the initial rain event pulse, the elevated freshwater content in the estuaries is pulsed out tidally and the plumes continue to cover more area than pre-storm (Figure 4.2e). The surf zone and inner-shelf percent area coverage generally track each other closely, suggesting the co-occurrence of surf zone and inner-shelf plumes in both time and space (Figure 4.2ee). It is more common for a surf zone plume to exist with no inner-shelf plume than vice versa (values along the bottom row in Figure 4.2ee). The relationship between surf zone and inner-shelf plume percent coverage is slightly skewed (values above the 1:1 line in Figure 4.2ee), such that the inner-shelf plume often occupies a slightly larger relative area than the corresponding surf zone plume.

Spatial Trends

Figure 4.3. Maps of percent plume occurrence (column 1: a-f) and plume coalescence (column 2: g-l) under different conditions (rows). The conditions include: all time (a, g), low discharge (b, h), moderate discharge (c, i), high discharge (d, j), smaller waves (e, k), and larger waves (f, l). The dashed purple line represents the mean surf zone edge. Note the variable colorbar limits across the panels. The number of hours the representative condition is true is displayed in each row's label. 1 km scale bars are included as black lines in lower right corner of each panel. Bathymetry contours are shown at 25, 50, 75, and 100 m.


All Plumes
Coalescence
all time
$Q < 1$ m^3/s
$1 \leq Q \leq 5$ m^3/s
$Q > 5$ m^3/s
$H_s \leq 0.9$ m
$H_s > 0.9$ m
(n = 11665 hrs)
(n = 10849 hrs)
(n = 615 hrs)
(n = 201 hrs)
(n = 8876 hrs)
(n = 2789 hrs)
lat
lon
33
32.95
32.9
-117.3
-117.26
occurrence (%)
a
b
c
d
e
f
g
h
i
j
k
l

River plumes from LPL, SDL, and SEL collectively impact an area that extends cross-shore up to the 100-m isobath and greater than 20-km alongshore from the northern model boundary to the headland of La Jolla Cove (Figure 4.3a). Near the mouth of LPL, where this study will focus, plumes are present more than 10% of all time. There is an equal chance that the plume is on the inner-shelf just offshore of the mouth at LPL, or that it has traveled a relatively equal distance in the surf zone in either direction (Figure 4.3a). The plumes north of LPL often export to the inner-shelf south of the SDL or SEL estuary mouths and have an equal likelihood to be present on the inner-shelf and in the surf zone at a given latitude, except near the estuary mouths. Using the Q_{river} and H_s near our focus estuary (LPL), percent occurrences can be made to visualize how often, under different discharge and wave conditions, plumes are present. With low discharge ($Q_{river} < 1\ m^3/s$), plumes have a limited alongshore and cross-shore extent (Figure 4.3b). With moderate ($1 \leq Q_{river} \leq 5\ m^3/s$) and high discharge ($Q_{river} > 5\ m^3/s$), there is greater than a 40% chance of plume presence between SDL and LPL in both the inner-shelf and surf zone, and an average percent presence around 30% on the full alongshore strip in the region (Figure 4.3c and d). When waves are smaller ($H_s \leq 0.9$ m), there is an equal distribution of percent plume presence, ~5% in the far-field and upwards of 10% at the mouth offshore of LPL (Figure 4.3e). When waves are larger ($H_s > 0.9$ m), there is a higher chance of both surf zone and inner-shelf plume presence than in the case with small waves (Figure 4.3f).

4.3.2 Patterns of Plume Coalescence

Due to the overlapping spatial influence of the plumes, as seen in Figure 4.3a, plume-to-plume interactions or coalescence is likely to occur. Plume coalescence occurs for less than 1% of the 14-months of study (Figure 4.3g). In general, there is a similar likelihood that plumes will coalesce in the surf zone and on the inner-shelf. The surf zone has not previously been considered a pathway for plume coalescence, but we show that it

is just as common as inner-shelf coalescence across time in the domain (Figure 4.3g). The plumes from LPL, SDL, and SEL often coalesce when they are all moving north or when they are all moving south, thus coalescence is most common north of the northern estuary or south of the southern one. This is true on the inner-shelf and in the surf zone. South of LPL, there is a distinct gap at the surf zone edge where no coalescence occurs. We explore this more in Section 4.4.4. There is also 'coalescence' detected inside of LPL and SDL. This will be referred to as plume intrusion into an adjacent estuary and is discussed in Section 4.3.5.

Under low discharge conditions ($Q_{river} < 1\ m^3/s$), there is no plume coalescence (Figure 4.3h). Under moderate discharge ($1 \leq Q_{river} \leq 5\ m^3/s$), plume coalescence occurs in both the surf zone and inner-shelf, most commonly at LPL and farther south (Figure 4.3i). In this case, coalescence occurs up to 10% of the time. Under high discharge conditions at LPL, coalescence is the most common, occurring between 10-20% of time in both the surf zone and inner-shelf (Figure 4.3j), mostly towards the north. It is likely that coalescence at, or following, high discharge conditions can occur south of LPL but is not seen in this data due to the limited number of rain events. With smaller waves ($H_s \leq 0.9$ m), there is coalescence at and south of LPL, mainly on the inner-shelf (Figure 4.3k). Meanwhile with larger waves, coalescence is most common at and south of LPL in the surf zone (Figure 4.3l). In both wave cases, there is inner-shelf and surf zone coalescence north of LPL.

4.3.3 Surf Zone Plume Coalescence Near-Mouth

Surf zone coalescence often begins near one estuary's mouth when an incoming plume travels from a farther estuary and a local plume is discharging from an adjacent estuary (Figure 4.4). The two plume roles will be referred to with these titles, the 'incoming' and 'local' plume respectively throughout this paper. When river plumes coalesce in the surf zone at an estuary mouth, two behaviors can result: the incoming plume can be

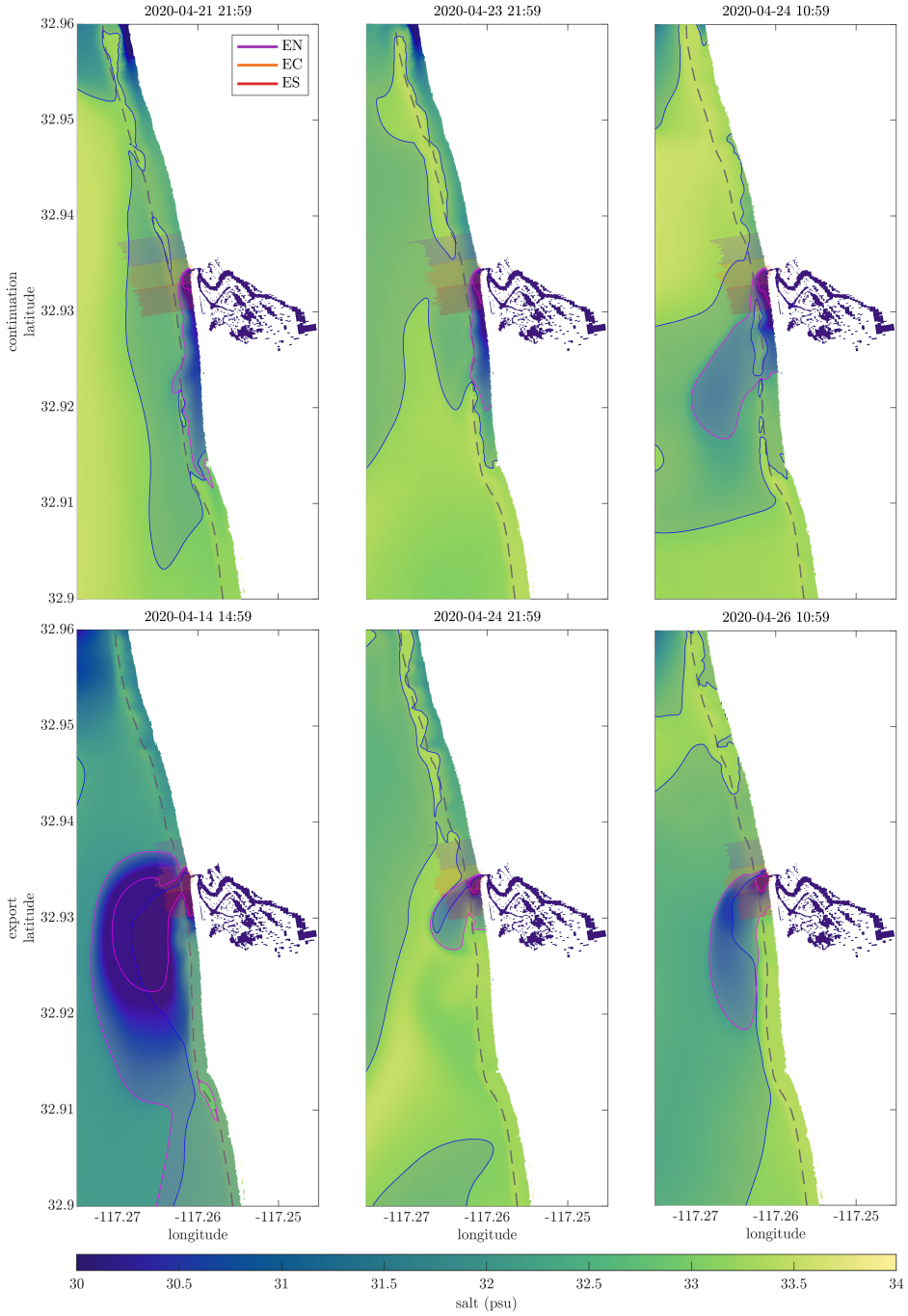


Figure 4.4. Snapshots of surface salinity (background color) and dye (contoured) for LPL (pink) and SDL (blue) for 3 continuation (row 1) and 3 export coalescence examples (row 2). Snapshots show the third hour after the coalescence example starts. The dashed line denotes the surf zone edge. The near-mouth transect regions EN (purple), EC (yellow), and ES (red) are lightly marked from the shoreline to $3L_{SZ}$. The first panel is an earlier stage of what becomes event 1 and the last panel is an earlier stage of what becomes event 2 discussed in Section 4.3.4. These maps are zoomed in to the region around LPL.

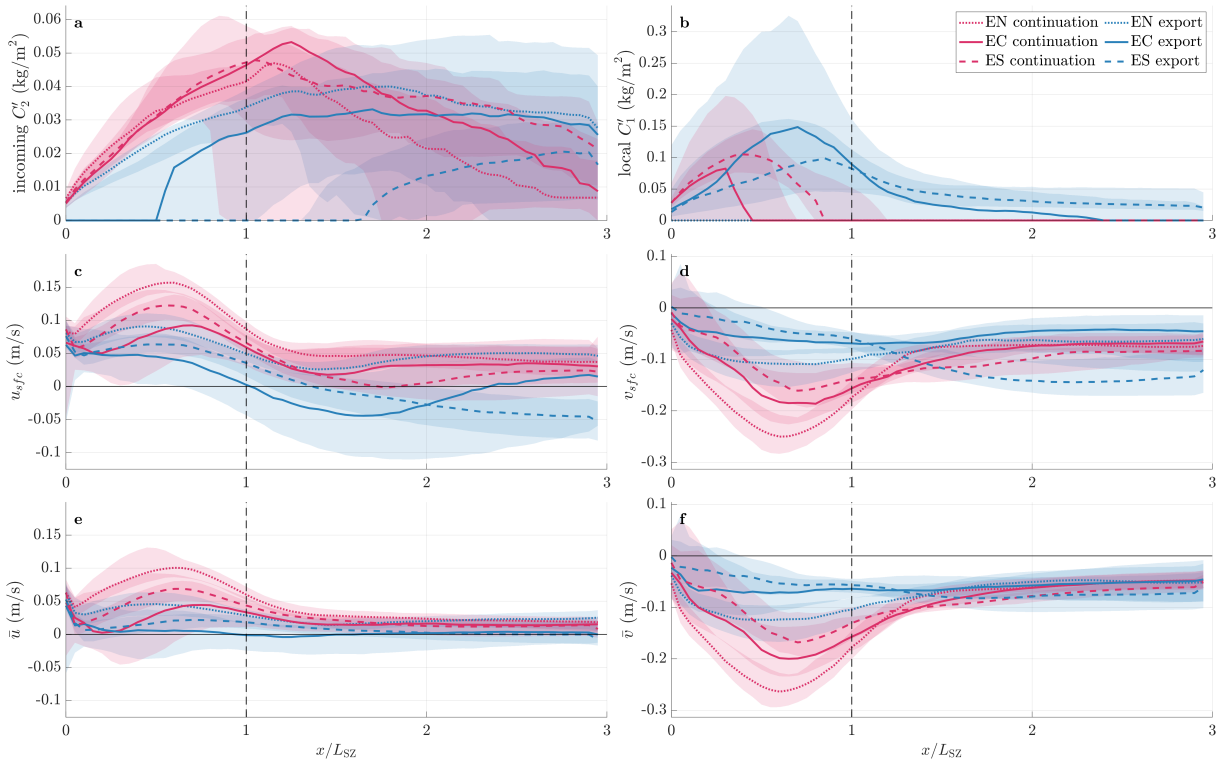


Figure 4.5. Comparison of grid line transects for 3 continuation (pink) and 3 export (blue) cases showing the temporal and spatial median of the transects north of LPL (EN, dotted line), at LPL's mouth (EC, solid line), and south of LPL (ES, dashed line). Shown for the incoming dye's depth integrated concentration (a), the local dye's depth-integrated concentration (b), the surface cross-shore (c) and alongshore (d) velocities, and the depth-averaged cross-shore (e) and alongshore (f) velocities. Dashed black vertical lines denote the surf zone edge. Solid black lines mark zero velocity on panels c-f. Shading around the median lines corresponds to the 25% to 75% quartile boundaries for the three examples for all transects within the region.

forced out of the surf zone by the local plume (export cases; Figure 4.4 row 2) and/or the incoming plume can continue alongshore in the surfzone with the local plume (continuation cases; Figure 4.4 row 1). We investigate how these behaviors differ using three cases for each behavior when the incoming SDL plume coalesces with the local LPL plume (Figure 4.4 and Figure 4.5). The frequency of occurrence of export cases is difficult to glean in Figure 4.3 because, while the coalescence begins in the surf zone at the mouth, the offshore export will appear similar to inner-shelf plume coalescence. However, the behaviors are easily differentiable when looking upstream (EN, dotted lines), directly at (EC, solid lines),

and downstream (ES, dashed lines) of the local estuary mouth (Figure 4.4) as in Figure 4.5. Along grid line distance is normalized to surf zone lengths (L_{SZ}), where 0-1 is the surf zone and 1-3 is a portion of the inner-shelf. Here the EC region is centered on the mouth of LPL spanning 150m north and 150m south, EN is north of the estuary starting from 150m north and spanning 300m up to 450m north, and ES is south of the estuary starting from 150m south and spanning 300m down to 450m south (Figure 4.4). Grid line transects are taken for every y index in those ranges from the shoreline (x=0) to 3 surf zone lengths (x=$3L_{SZ}$) offshore, using time-dependent locations for both bounds. For each example within a behavior, all transects are converted onto this uniform distance coordinate system. Each example lasts 5 hours (see shading in Figure 4.2 that marks the examples). The data presented in Figure 4.5 are the grid line normalized profiles of median values across all transects in a region (EN, EC, or ES) for all 5 hours of all 3 examples for a given behavior (continuation or export), with the 25% to 75% quartile boundaries shaded.

Export cases are characterized by an incoming plume that does not pass the estuary mouth and instead moves offshore with the local plume (Figure 4.4 row 2; shown in blue, Figure 4.5). Continuation cases are when an incoming plume continues past the estuary mouth along with the local plume within the surf zone (Figure 4.4 row 1; shown in pink, Figure 4.5). The far-field plume of the incoming plume has both surf zone and inner-shelf components by the time it reaches the local estuary (Figure 4.4), as also seen in the highly correlated surf zone and inner-shelf plume area percent (Figure 4.2ee). The incoming and local plumes retain a similar amount of freshwater across EN, EC, and ES in the surf zone and inner-shelf in the continuation case (pink lines in Figure 4.5a and b). The export cases have the most incoming plume water at EN, less at EC, and none at ES in the surf zone (blue lines in Figure 4.5a). ES has an inner-shelf incoming plume but of a lower concentration than that of EN or EC, implying the plume has either mixed and/or been redirected farther offshore than $3L_{SZ}$ (Figure 4.5a; Figure 4.4 row 2). However, in the continuation cases the amount of incoming freshwater on the inner-shelf does not change

significantly when passing the local estuary, suggesting the local outflow has little effect on the structure of the incoming plume (Figure 4.5a).

There is no northward plume transport across these examples, i.e. no local dye north of the estuary in all cases (Figure 4.5b). Export cases typically have more local plume freshwater in the surf zone and inner-shelf near the estuary mouth (EC) compared to the continuation cases which have less surf zone freshwater and none on the inner-shelf (Figure 4.5b). This suggests that the export cases have stronger river discharge and more local freshwater than continuation cases. In the export cases, there is a reduction in local surf zone freshwater between EC and ES because of the offshore plume export which likely directs more water offshore past $3L_{SZ}$ consistent with the trend in the incoming plume (Figure 4.5b). In the continuation cases, the freshwater content from the local estuary is relatively constant from EC to ES across the surf zone and inner-shelf (Figure 4.5b).

The continuation cases have stronger surf zone velocities, alongshore (Figure 4.5e and f) and cross-shore (Figure 4.5c and d), compared to the exporting cases. EN has stronger surf zone velocities compared to EC and ES across all cases (Figure 4.5 c-f). All continuation case velocities are strongest mid-surf zone, consistent with a typical cross-surf zone velocity structure (Guza et al., 1986). The continuation cases have onshore and southward surfzone velocity, including at the river mouth, and a weakly onshore inner-shelf and southward inner-shelf flow (Figure 4.5 c-f). The surf zone depth-averaged cross-shore velocities in the exporting cases are weakest and occasionally offshore or near zero at EC (Figure 4.5e). Despite having a surface-intensified onshore Stokes velocity, there is offshore surface plume velocity in the exporting case across the inner-shelf for most of EC and ES (Figure 4.5c). The surface alongshore velocities at ES are the weakest velocity in the surf zone and the strongest on the inner-shelf in the export cases (Figure 4.5d). Both of these facts allude to there being a weak surf zone with more energetic offshore and southward surface flows on the inner-shelf during the export cases.

4.3.4 Far-Field of Surf Zone Plume Coalescence

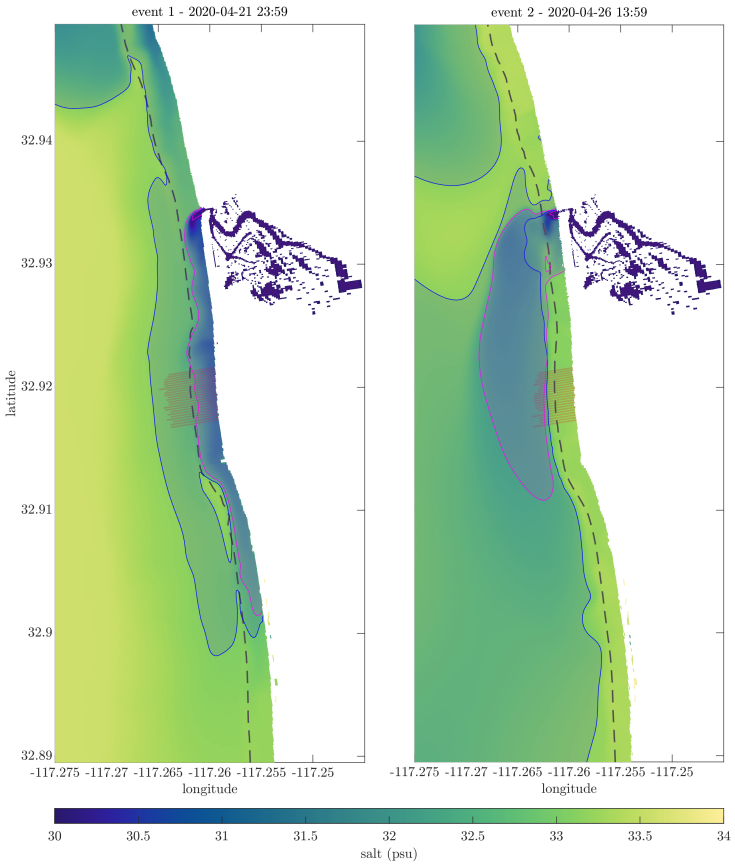


Figure 4.6. Snapshots of surface salinity (background color) and dye (contoured) for LPL (pink) and SDL (blue) for 2 events in the far-field region after 2 coalescence events (shown in Figure 4.4). The dye contours are shown between 0.01, 0.1 and 1 kg/m^3. The dashed line denotes the surf zone edge. The far-field transect locations used here and throughout this study are shown from the shoreline to $2L_{SZ}$ in light red.

We investigate the cross-shore structure along grid lines of two case studies, event 1 with coalesced LPL and SDL surf zone plumes and a SDL inner-shelf plume that follows after a continuation case, and event 2 with only LPL and SDL coalesced inner-shelf plumes that follows after an export case. The structure of coalesced plumes is explored in this section, and the connection to previous literature regarding surf zone to inner-shelf exchange is explored in Section 4.4.2. The two events are each averaged over a range of far-field transects (red lines in Figure 4.6) for 5 hours, starting at April 21, 2020 21:00

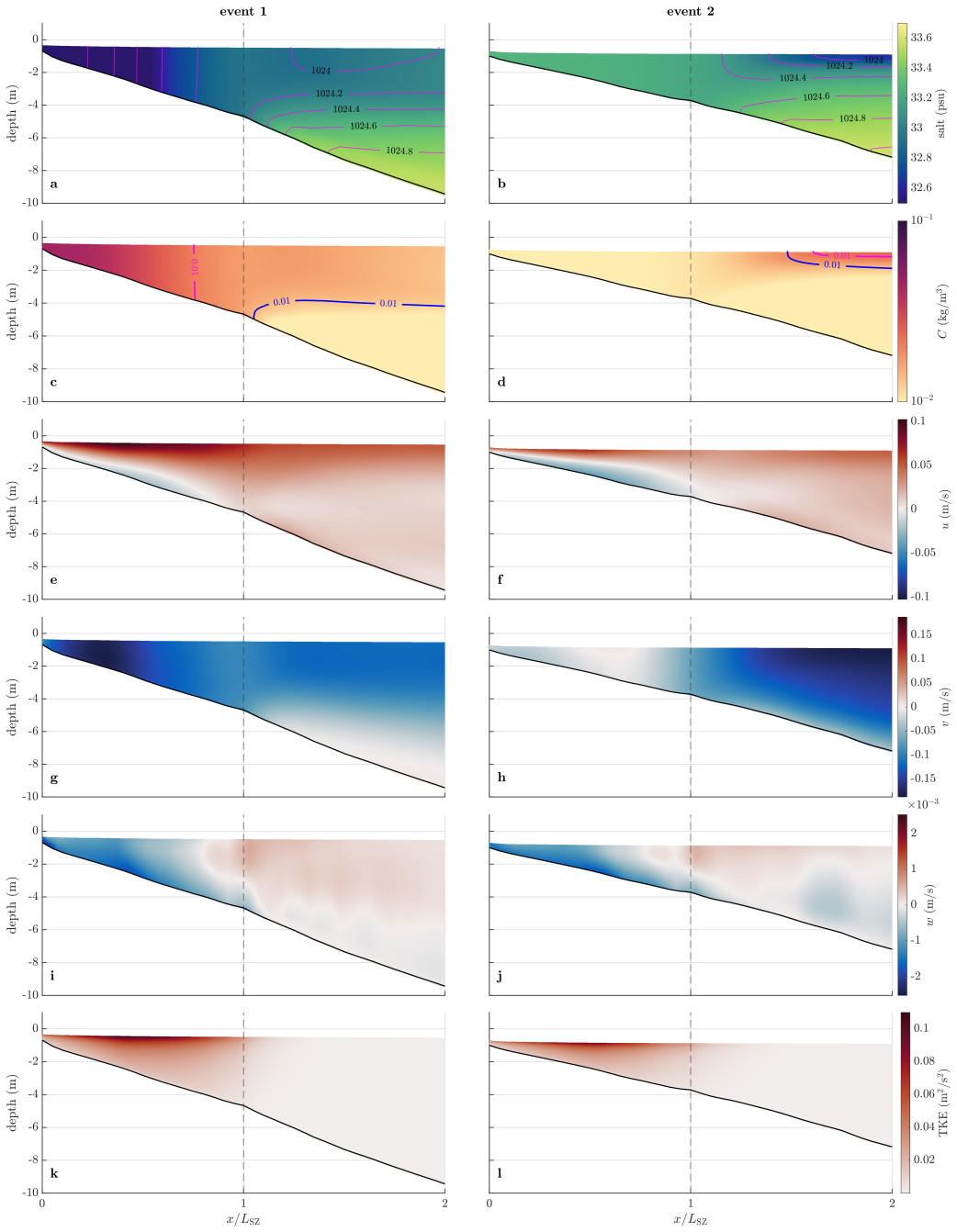


Figure 4.7. Grid line transects averaged over 2 events each lasting 5 hours, starting at April 21, 2020 21:00 UTC for event 1 and April 26, 2020 11:00 UTC for event 2. Each event has far-field transect averaged values of salinity with density contours overlaid (a,b), total concentration C with LPL (C_1, pink) and SDL (C_2, blue) 1% threshold contours overlaid (c,d), cross-shore velocity u (e,f), alongshore velocity v (g,h), vertical velocity w (i,j), and turbulent kinetic energy TKE (k,l). The dashed black line shows the position of the surf zone edge.

UTC for event 1 and April 26, 2020 11:00 UTC for event 2. Event 1 occurs following a continuation case (Figure 4.4 first panel) and event 2 occurs following an export case (Figure 4.4 last panel).

In event 1, there is a 0.2 kg/m^3 density difference between the plume at the surf zone edge and a surface stratified inner-shelf plume, and a difference of 1.0 kg/m^3 from the inner surf-zone to the outer surf zone (Figure 4.7a). The inner-shelf plume originates from SDL and has mixed to a depth of 4 m (Figure 4.7c). The surf zone has a pronounced horizontal density gradient and little stratification due to strong vertical mixing (Figure 4.7a,c). The surf zone plume is a mix of the more concentrated local LPL and the more diluted incoming SDL (Figure 4.7c). The cross-shore velocity structure has onshore velocity at the surface and offshore velocity at depth in the surf zone (Figure 4.7e), which follows an expected wave driven flow with return flow at depth called undertow (Shepard, 1936). The onshore velocity is weaker at the plume base on the inner-shelf (Figure 4.7e). The plume layer ($\leq$ 4 m depth) has southward surf zone and inner-shelf velocity, with the strongest velocities at 0.25 L_{SZ} and the weakest at L_{SZ} (Figure 4.7g). The vertical velocities are downward in the surf zone and upward on the inner-shelf (Figure 4.7i). At L_{SZ}, there is upward velocity at the surface but downward at depth.

In event 2, the wave driven flow is weaker than event 1 in both the cross-shore and alongshore (Figure 4.7f,h). In the cross-shore velocity, there is a weaker onshore surface flow and more pronounced undertow that extends just past the surf zone edge, which carries the denser surf zone offshore at depth (Figure 4.7f). Similar to event 1, there is a band with weak cross-shore flow at a depth similar to the undertow on the inner-shelf. While event 1 has peak alongshore surf zone currents mid-surf zone and weaker inner-shelf shelf currents (Figure 4.7g), event 2 has no alongshore flow mid- surf zone and the strongest alongshore velocities on the inner-shelf (Figure 4.7h). The turbulent kinetic energy in event 1 (Figure 4.7k) is stronger than in event 2 (Figure 4.7l), consistent with stronger waves in event 1.

4.3.5 Intrusion of Incoming Plume into Local Estuary

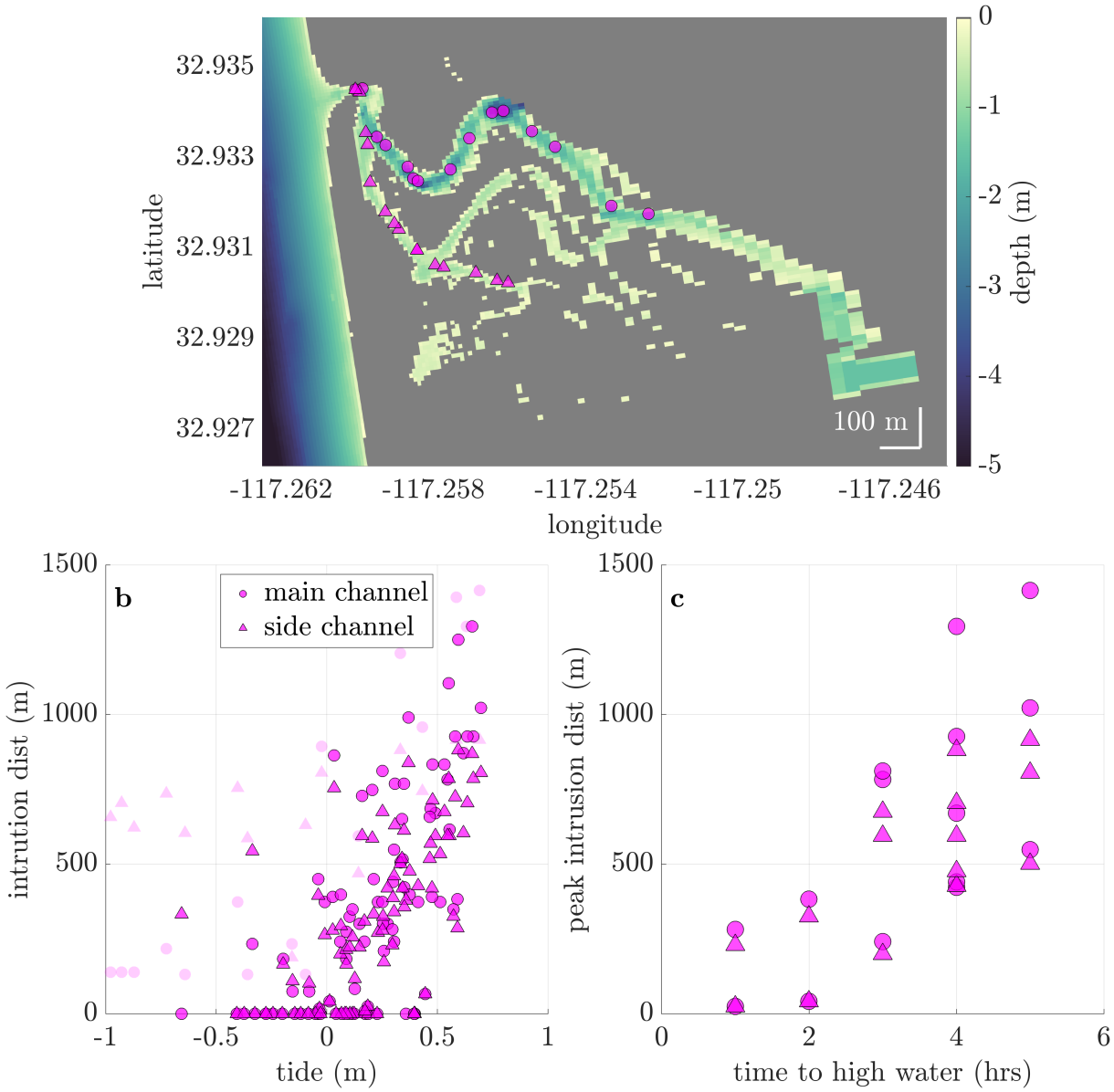


Figure 4.8. (a) LPL peak plume intrusion locations with depth as the background color. (b) Plume intrusion distance up-estuary compared with the tidal elevation and (c) peak intrusion distance compared to hours from plume entry to high tide. The main channel intrusions are shown with circles and the side channel intrusions are triangles. Points that are transparent and not outlined denote the hourly measurements during the event that remains in LPL longer than one flood tide.

While near-mouth surf zone coalescence occurs when an incoming plume meets a local ebbing plume, sometimes an incoming plume reaches an adjacent estuary during

flood tide. In these cases, the incoming plume will tidally pump into the local estuary (Figure 4.8a). There are fifteen occasions when the SDL plume intrudes into LPL and 16 cases of LPL plume intrusion into SDL. The intrusion events into SDL are not shown in the results because the grid's resolution is lower at SDL and SEL and the estuarine exchange flow is less resolved. Fourteen of the fifteen intrusion events into LPL stay in the estuary between 2-9 hrs. One intrusion event remains in both the main and side channels for longer than one flood and one ebb tide, persisting for 17 hours (transparent points in Figure 4.8b).

The plume's distance traveled up estuary increases with increasing tidal elevation (Figure 4.8b). The incoming plume intrudes a maximum distance of 1400 m into LPL's main channel and 900m into LPL's side channel during the time with the most overlap between flood tide and plume presence (Figure 4.8c). The maximum intrusion distance increases with duration of time between plume entry and high tide (when the currents will slacken and reverse directions back out of the estuary). The incoming plume typically reaches its farthest intrusion extent below the surface because it is more dense than the surface water in the estuary, especially farther into the estuary (not shown).

4.4 Discussion

4.4.1 Surf Zone Plume Coalescence

In this work, we introduce the pathway that the surf zone provides for coalescence, show where and how often coalescence occurs, and detail two types of surf zone plume coalescence that occur near an adjacent estuary mouth.

General Occurrence and Trends

We show that small river plume coalescence occurs in the surf zone, which is an interaction not described in prior literature. Surf zone coalescence occurs at similar frequencies and across similar alongshore extents as inner-shelf coalescence (Figure 4.3g).

Surf zone coalescence is more common than inner-shelf coalescence near-mouth when waves are larger (Figure 4.3l), but otherwise occurs across similar conditions as inner-shelf coalescence. This highlights the common nature of surf zone coalescence occurring alongside inner-shelf coalescence.

Plume coalescence does not occur during typical low discharge conditions. However, when there is elevated outflow, plumes occupy more area and coalescence is more common (Figure 4.3). As plume coalescence is more common in smaller watersheds than in larger watersheds (Warrick, Farnsworth, 2017), and small river systems produce plumes that often have a surf zone component (Wong et al., 2013; Rodriguez et al., 2018; Kastner et al., 2019; Lou et al., 2025), it is not surprising that surf zone plume coalescence occurs in these systems. It is important to note the model used here does not include transient rip currents, instead, mixing is elevated to simulate missing energy dissipation from the surf zone. This may impact the frequency of surf zone coalescence in this model compared to reality either by underestimating it if the model mixing is artificially high, or overestimating it if the lack of transient rip currents significantly increases surf zone export and decreases the chances of coalescence.

The conditions that promote surf zone plume coalescence are the same factors that drive alongshore flow in the surf zone, obliquely angled incoming waves. Just as direct wind is often a driver of inner-shelf small plume transport and therefore inner-shelf coalescence (Warrick et al., 2007; Osadchiev et al., 2021; Vundavilli et al., 2024), alongshore surf zone currents are the primary driver of surf zone small plume transport and therefore surf zone coalescence (Rodriguez et al., 2018). The direction and speed of alongshore surf zone currents are set by the wave height, wave angle relative to the shore normal angle, and the resulting alongshore component of the wave radiation stress S_{xy} (Longuet-Higgins, 1970; Guza et al., 1986). Therefore, surf zone coalescence occurs only when the S_{xy} and resulting alongshore surf zone current are driving flow in the direction of an adjacent estuary.

Connection of Surf Zone Coalescence with Near-Field Trapping

Surf zone plume coalescence near an adjacent estuary mouth can result in the incoming plume exporting to the inner-shelf, or the incoming plume continuing in the surf zone along with the local plume (Figures 4.4 and 4.5). The exporting behavior of a far-field incoming plume coalescing with a local ebbing plume occurs when there is a relatively high amount of freshwater in the local plume and when the waves are weaker (Figure 4.5). This is consistent with expected behavior for near-mouth plume escaping (Wong et al., 2013; Rodriguez et al., 2018). A locally formed river plume can have surf zone trapped waters if the wave momentum is stronger than the river momentum at the estuary mouth (Wong et al., 2013; Rodriguez et al., 2018; Kastner et al., 2019; Lou et al., 2025), which also promotes the retention of an incoming plume from an adjacent estuary in the surfzone. With an escaping near-field plume, river momentum dominates over wave momentum and the local plume exports to the inner-shelf, along with the incoming plume.

However, plumes are not always clearly only trapping or escaping over one ebb (Figure 4.4; Lou et al. (2025)). With the common co-occurrence of surf zone and inner shelf plumes (Figures 4.2e,ee, 4.3a, 4.9), it is often not straightforward to precisely identify the pathways for surf zone to inner-shelf exchange in the near- and far-field. Moreover, small plumes rapidly respond to changing environmental conditions, whether that be with regards to surf zone or inner-shelf drivers (Osadchiev et al., 2021; Byrne et al., 2026). Likely this same variability is present in the coalescence of small plumes. This leads to plume behavior (for both individual plumes and plume coalescence) that may begin as escaped/ exported, but then transition to a trapped/ continuation behavior within a few hours (or vice versa) as conditions change.

4.4.2 Far-Field/ Surf Zone Plume Interactions

The cross-shore transport of small plumes across the surf zone will be influenced by the waves and the relative water densities. While less literature discusses the cross-shore transport of plumes between the surf zone and inner-shelf, there are studies that detail how buoyancy impacts this cross-shore exchange in rip currents. More dense surf zone waters will export at depth to the inner-shelf, whereas a less dense surf zone will spread to the inner-shelf at the surface (Moulton et al., 2021; Grimes et al., 2021). This pattern could apply to the cross-shore transport of plumes from the surf-zone to the far-field, and therefore be dependent on whether there is a plume in the surf zone, inner-shelf, or both.

Similar to Moulton et al. (2021); Grimes et al. (2021), a denser surf zone will transport offshore at depth given the presence of an inner-shelf plume (Figure 4.7 event 2). While a less dense surf zone plume may be expected to export offshore at the surface, this is not the case in Event 1 (Figure 4.7). Instead, the strong mixing within the surf zone causes the surf zone plume to have the same density at the surf zone edge as it does at the surface offshore (Figure 4.7). In turn, cross-shore transport of this surf zone plume is not likely to follow either of the expected behaviors for buoyancy influenced cross- surf zone exchange (Moulton et al., 2021; Grimes et al., 2021). This suggests the lateral density structure of a surf zone plume impacts the cross-shore exchange between the surf zone and inner-shelf. These are only two examples of the structures of far-field plumes, a more comprehensive analysis across a variety of tidal, wave, and discharge conditions would further improve our understanding of these processes. A limitation of the model is the use of a constant horizontal mixing coefficient (0.5 m^2/s). In practice, the value used is likely too high for the inner-shelf and too low for the surf zone, but was found to be the most accurate choice for a constant coefficient (Lou, 2025). The cross-shore mixing of a far-field plume may therefore be artificially low in the surf zone and artificially high offshore which will influence the modeled cross-shore exchange.

The far-field structure of event 1 in Figure 4.7 is the result of a continuation example of surf zone coalescence, whereas event 2's is the result of an export example. The type of surf zone coalescence behavior that occurs could serve as an indictor for far-field plume structure, reflecting the wave and discharge conditions. The difference between the rapid alongshore, and strong onshore, surf zone flow in event 1 compared with the stagnant alongshore surf zone flow, stronger undertow, and strong inner-shelf alongshore currents in event 2 could influence, and be influenced by, near-mouth surf zone coalescence and the far-field plume structure.

We show the far-field cross-shore structure of plumes may feature plumes and coalescence in the surf zone but not over the inner-shelf, and vice versa (Figure 4.7). There is high spatial and temporal complexity in the distribution of far-field plumes (Figures 4.2, 4.3, 4.4). Thus, the cross-shore structure and transport of these plumes, particularly as they interact with the surf zone and near-field plumes, can exhibit high variability with important dynamical consequences. While not discussed in this work, other far-field mechanisms for plume coalescence can include these surf zone to inner-shelf exchange processes. If a local plume exports from the surf zone into an inner-shelf plume, coalescence will occur. This applies to export within bathymetric rip currents, transient rip currents, or through general wave-driven circulation and undertow.

4.4.3 Surf Zone Pathway for Inter-Estuary Connectivity

The surf zone serves as a highway to connect adjacent estuaries. Low-inflow estuary plumes travel alongshore in the surf zone and, if they reach an adjacent LIE during flood tide, the plume intrudes into the other estuary. The surf zone is responsible for delivering the incoming plume that intrudes into the local estuary for estuary intrusion events. Despite the common co-occurrence of surf zone and inner-shelf plumes (Figure 4.2e), plume intrusion only occurs when the incoming plume's alongshore extent in the surf zone is past the local estuary (Figure 4.9). With only an inner-shelf plume present at

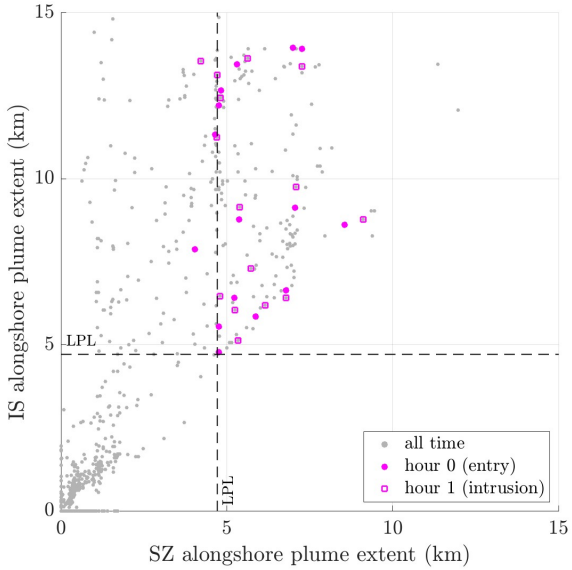


Figure 4.9. Farthest alongshore plume extent south of SDL (incoming dye source) in the surf zone vs on the inner-shelf for all time (gray circles) and for the hour before (pink squares) and first hour (pink circles) of estuarine intrusion events. Dashed lines on both axes mark the location of LPL with respect to distance traveled from SDL. Note, distances are shown as positive for clarity but represent southward transport from SDL.

the estuary mouth, there is no plume intrusion (top left quadrant of Figure 4.9). Only when a surf zone plume is present at the local estuary's mouth does plume intrusion occur (top right quadrant in Figure 4.9).

There are no instances in the 14-month study where a plume reaches the estuary mouth in the surf zone without an inner-shelf plume component. Building on the result that inner-shelf and surf zone plume areas are similar across time (Figure 4.2e,ee), we see that the inner-shelf and alongshore plumes often travel similar distances at the same time (Figure 4.9). This echos previous findings that the surf zone serves as an important pathway to far-field inner-shelf plume presence (Byrne et al., 2026). While it is more common for there to be an inner-shelf plume component farther than the surf zone plume component at distances greater than 2 km from the origin (Figure 4.9 scatter above the 1:1 line), near the mouth, there can be surf zone plumes that exist up to 2 km away with no inner-shelf component (Figure 4.9 points along the x-axis at y = 0).

In our study period, there are almost an equal number of occasions where the LPL plume intrudes into SDL (when S_{xy} is predominantly >0) compared to when the SDL plume intrudes into LPL (when S_{xy} is predominantly <0). This highlights how intrusion is equally as common in either LIE, but dependent on the wave conditions. The fifteen intrusion events in LPL all occur over a 15 day period between April 12 - 27, 2020 with an average duration of 5.3 hrs. These repeated events with short recovery windows could have ecological consequences. They may impact larval transport, pollutant and sediment distributions, and population connectivity (Roegner et al., 2002). Plumes can act as accumulation zones of nutrients and sediments (Milliman, Syvitski, 1992; Anderson et al., 2002; Ryther et al., 1967), and thus the intrusion of a plume into an adjacent estuary has the potential to deliver these quantities to an adjacent system. By the time an incoming plume reaches an adjacent LIE, it has mixed such that it is often denser than the estuary's surface water and will subduct to the estuary bed, potentially delivering larvae or other particles to depth in the estuary.

Another impact of estuarine plume intrusion is that it could enhance coastal dispersion of freshwater and constituents such as sediment, larvae, and pollutants. Prior work has shown shoreline features like embayments can enhance dispersion within estuaries (Okubo, 1973; Geyer, Signell, 1992). This data shows that plumes passing by an adjacent estuary on flood tide can be taken inside of the estuary, similar to flow diverting into an embayment. They then may export on a subsequent ebb tide enhancing coastal dispersion of that water mass. Future studies could investigate the impact an adjacent estuary has on coastal dispersion of freshwater and estuarine constituents.

4.4.4 Implications for Water Quality

Understanding small river plume fate is of particular interest in regions with polluted outflow, where health risks are highest in areas with high exposure and in regions that have more concentrated pollutants (Feddersen et al., 2021). Concentration is a function

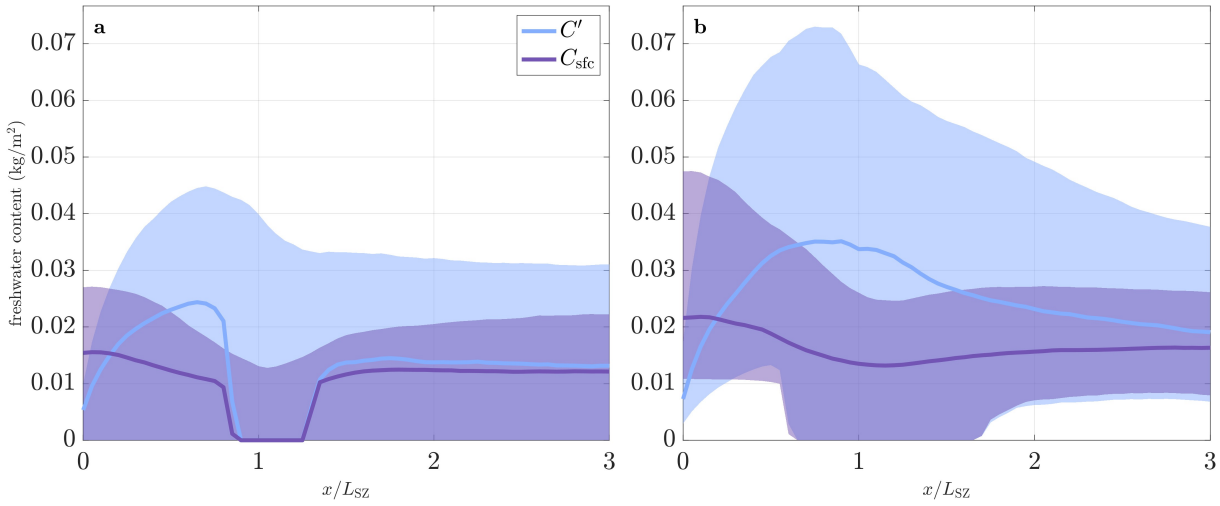


Figure 4.10. Median of grid line transect values of total depth-integrated dye (blue) and surface dye concentration (purple) across far-field transects south of LPL (a) shown in Figure 4.6 and north of LPL (b) between 32.943 and 32.947°N. Shading corresponds to the 25% to 75% quartile boundaries. Across the 14-month of study, a given time step is included in the quartiles if any grid line point in the transect-averaged values has $C' > 0.01$.

of the dilution and dispersion of a plume (Romero et al., 2016). We investigate the spatial patterns of far-field plume concentration across the surf zone to the inner-shelf for times with plumes for a region south of LPL (Figure 4.10a) and another north of LPL (Figure 4.10b). This is done as a comparison of the depth-integrated dye content (C'), which informs how much plume water is present in that region, to the average top 1-m dye concentration C_{sfc}. C_{sfc} is a relevant concentration as it is a common region of exposure for humans in the coastal ocean. All far-field transects (south of LPL (a) shown in Figure 4.6 and north of LPL (b) between 32.943 and 32.947°N) are included in Figure 4.10 across any time within the 14-months if $C' \geq 0.01\ kg/m^2$ at any point in the transects' spatial average for that hour.

The location with the most plume water present (C') is different from where the surface waters have the highest concentration (C_{sfc}) at both sites (Figure 4.10). South of LPL, C' increases across the surf zone with a peak value around $0.75L_{SZ}$ and then drops to zero by $1L_{SZ}$, before increasing back to a constant value on the inner-shelf between

1.5-3L_{SZ} (Figure 4.10). Both north and south of LPL, the surface concentration is highest in the inner- surf zone and decreases linearly until just before $1L_{SZ}$ where it drops and then begins increasing by $1.25L_{SZ}$ to a constant value maintained across the inner-shelf. Overall, the most notable divergence in C' and C_{sfc} occur in the surf zone. Near the shoreline where plume content is lowest, the surface concentration is highest, and near $0.75L_{SZ}$ where the surface concentration is low, the plume content is high (Figure 4.10). This contrasts the rest of the profile from 1-3L_{SZ} where C' and C_{sfc} are nearly identical south of LPL, and become more similar farther offshore north of LPL.

The cross- surf zone freshwater structure is a reflection of vertical mixing, water depth, and plume liftoff. The surf zone tends to be well mixed vertically due to strong vertical mixing induced by wave breaking (Thornton, Guza, 1983; Feddersen, Trowbridge, 2005; Feddersen, 2012; Kumar et al., 2012). In the model, this wave induced mixing is represented as a surface flux of TKE implemented as a surface boundary condition that solves the Generic Length Scale scheme and results in elevated surf zone TKE with the strongest values near surface, as seen in Figure 4.7k,l (Feddersen, Trowbridge, 2005; Kumar et al., 2012). Due to strong surf zone vertical mixing, the surface concentration will decrease as the water column deepens towards the surf zone edge. The inner-shelf plume, despite being in deeper water, is surface stratified with weaker vertical mixing (Figure 4.7k,l) resulting in a higher surface plume concentration (Figure 4.10b). In fact, frequently plume liftoff is seen at the surf zone edge (Rodriguez et al., 2018; Lou et al., 2025) which supports the finding that the inner-shelf plume will be surface-stratified while the surf zone plume extends to the seafloor.

The behavior of C_{sfc} between 0-$0.75L_{SZ}$ is what would be expected of a constant volume of freshwater diluting as waters get deeper, but interestingly, this is still true while C' increases across the surf zone. The increased dilution with increased water depth in the well-mixed surf zone and/or some contribution from mixing and cross-shore exchange compensate for the higher plume content that is less surface concentrated. A previous

study of shoreline released dye in a non-buoyant surf zone showed surface surf zone dye concentrations that decrease with distance from the shoreline (Clark et al., 2010), agreeing with our finding that surface concentration decreases from the shoreline to the surf zone edge. The Clark et al. (2010) observations do not show an increase in surface concentration on the inner-shelf which differs from our results that show an increase offshore due to the presence of buoyant river plumes. This makes sense as the prior study released a neutrally buoyant dye at the shoreline in ambient ocean water whereas the dye in the present study follows buoyant river plumes that transport on both the inner-shelf and in the surf zone.

Further, it is unexpected that both C_{sfc} and C' show no plume presence, in the median case, at the surf zone edge south of LPL (Figure 4.10a). This implies that plumes do not often cross the surf zone edge, instead staying only in the surf zone, only on the inner-shelf, or on both but without transporting across the surf zone edge. In this case, the surf zone edge surface concentration is lower primarily because the total plume content is less. This result is consistent across various figures including snapshot maps of surface fields where the surf zone edge tends to be saltier than the surrounding plume and contain less surface dye, and in occurrence maps where there is often a lack of plume presence and coalescence (e.g. Figures 4.3a,g, 4.4, 4.10). However, this is not the case north of LPL where plume presence is continuous cross-shore, highlighting that some far-field locations may have plumes present across the surf zone edge. In this case, the surf zone edge surface concentration is likely lower because of dilution of the well-mixed surf zone waters. Future work investigating the spatio-temporal variability in surface plume concentration and total plume content at different alongshore locations could illuminate the differences between the surface dye concentrations north and south of LPL seen between Figure 4.10a and b. The differences between the two sites could reflect trends specific to their relative distances from neighboring estuary mouths, or differences in the strength of surf zone to inner-shelf exchange in the alongshore stretch between the estuary mouth and the given site. A given stretch of coastline may be more likely to have only a surf zone plume, only an inner-shelf

plume, or both; the surface concentrations in these distinct cases will be the subject of future work. Additionally, separating the dye by each contributing river will inform if these cross-shore differences north and south of LPL are due to the presence of other plumes. Lastly, a freshwater and momentum budget within the surf zone could provide context for what is advecting and/or mixing the plume at the surf zone edge in some cases but not in others (Figure 4.10).

If this was a polluted plume, swimmers in the surface water would have the least exposure to pollutants at the surf zone edge, and a similar exposure at the shallowest surf zone waters and on the inner-shelf (past 1.5 L_{SZ}) while plumes are present. A limitation of this model is the surf zone is nearly always well mixed vertically. While this is often true, surf zone stratification in the presence of plumes has been observed (Kastner et al., 2018). Our model does show vertical stratification in the surfzone at a few times, but more commonly the modeled surf zone plumes are nearly well mixed vertically. If the model is over-mixing in the vertical, it would artificially lower surface concentrations compared to reality. Additionally, this model uses a constant horizontal diffusivity which may underestimate the surf zone's, and overestimate the inner-shelf's, lateral dispersion of tracers. This highlights the need for future research that investigates the vertical structure of small plumes in the surf zone under varying conditions with in-situ data.

4.5 Conclusions

In this work, we detail novel interactions that occur due to the surf zone transport of plumes in a region with multiple low-inflow estuaries. Over 14 months, the plumes from three LIEs can occupy anywhere within a continuous band spanning >20 km alongshore in the surf zone and inner-shelf, and cross-shore to the 100-m isobath. Under typical low discharge conditions, plumes do not travel far from their respective LIE mouth. Plumes can occupy a large area of the surf zone and inner-shelf, up to 60% of the time with high

discharge. Plumes are more common in the surf zone and inner-shelf when waves are larger.

The percent of relative plume area in the surf zone and inner-shelf match closely across the study period. Despite averaging $\sim 4\%$ plume area coverage in the surf zone and inner-shelf within a representative box spanning 4 km north of SDL to 4 km south of LPL, the elevated outflow following rain events increases plume area, covering up to $\sim 100\%$ of the surf zone and inner-shelf boxes. Plume presence increases ambient inner-shelf stratification with implications for surf zone to inner-shelf exchange.

The cross-shore structure of far-field plumes varies depending on whether there is a plume in the surf zone or not. Comparing an example of a strong surf zone plume and a weak inner-shelf plume (event 1) with an example of only an inner-shelf plume (event 2), we find the wave-influenced onshore velocities are stronger in event 1 and the offshore-directed undertow is stronger in event 2. Notably, the alongshore currents vary significantly in the cross-shore where event 1 (event 2) has strong southward flow (no flow) in the mid- surf zone and weaker (strong) inner-shelf currents. Cross-shore variability in the far-field's total plume content and surface plume concentration shows that plume content and surface concentrations follow inverse spatial patterns in the inner-surf zone. The surface concentration is high in the inner- surf zone and on the inner-shelf despite having low plume content. The surf zone edge has the least concentrated surface plume waters.

Due to the temporal and spatial overlap of surf zone and inner-shelf plumes, there can be plume coalescence between the LIE plumes on the inner-shelf and in the surf zone. Plume coalescence is most common south of LPL or north of SEL due to the region broadly having coherent surf zone and inner-shelf currents during and after rain events (Byrne et al., 2026). Coalescence is most common with moderate to high discharge conditions, occurring $\sim 10\%$ of time in the surf zone and inner-shelf. Surf zone coalescence is more common than inner-shelf coalescence near the mouth of LPL with large waves, whereas

inner-shelf coalescence is more common with smaller waves. Plume coalesce occurs in the surf zone when S_{xy}, and the resulting alongshore surf zone current, drive a plume from one estuary to another. Inner-shelf plume coalescence occurs when currents drive one plume towards another, often due to wind following storm events (Vundavilli et al., 2024; Byrne et al., 2026). Additionally, we show that inner-shelf coalescence can occur due to surf zone plume export to the inner-shelf.

Two types of surf zone coalescence are possible when a surf zone plume reaches an adjacent estuary mouth at ebb tide. The incoming surf zone plume can be exported out to the inner-shelf by the local plume, or it can continue past the mouth trapped with the local plume in the surf zone. The trapping or escaping behavior of the local plume will dictate whether the incoming plume is exporting to the inner-shelf or continuing in the surf zone. The exporting cases occur when the freshwater content is higher, the surf zone currents are weaker, and there is offshore flow in the inner-shelf. The continuation cases occur when the wave-driven currents are strong and freshwater content is lower. In the export case, plumes that could contain pollutants are forced to export from the surf zone because of an adjacent ebbing LIE plume, thus reducing the chance of beachgoer interactions with the polluted waters in the surf zone. The type of surf zone coalescence behavior that occurs could serve as an indictor for far-field plume structure that reflects the prevalent wave and discharge conditions.

If a surf zone plume reaches an adjacent estuary on flood tide, the incoming plume will intrude into the adjacent estuary. Despite the common co-occurrence of surf zone and inner-shelf plumes, plume intrusion only occurs when a plume is present in the surf zone. The distance up-estuary a plume intrusion reaches is a function of the strength and timing of the flood tide. The farthest extents are reached when the tidal amplitudes are greatest and when the plume overlaps with the flood tide for the longest duration. Moreover tidal pumping of plume water in and out of an adjacent estuary will influence coastal dispersion.

In summary, we present novel results that show how the surf zone can serve as a

pathway for inter-estuary connectivity and for plume coalescence for adjacent low inflow estuaries. Understanding the fate of small plumes will help us appropriately model river plumes and better understand the transport of their constituents, which can have implications for ecosystem and human health.

Availability Statement

River gauges operated by the U.S. Geological Survey (USGS) provide Q_{river} for Los Peñasquitos Lagoon, Santa Maria Creek, and San Diego River. San Elijo Lagoon Q_{river} is provided by the San Diego County Flood Control District https://sandiego.onerain.com. The City of San Diego Transportation & Storm Water Department provided information for the Lake Hodges dam discharge entering San Dieguito Lagoon. Sources for all other model data are detailed in Pan et al. (2025) and Wu et al. (2020).

Acknowledgments

Chapter 4, in full, is currently being prepared for submission for publication of the material. Byrne, S.M.; Giddings, S.N.; Merrifield, M.A.; Horner-Devine, A.R.; Spydell, M.S.; and Lou, Y. The dissertation author was the primary investigator and author of this material.

We would like to acknowledge high-performance computing support from the Derecho system (doi:10.5065/qx9a-pg09) provided by the NSF National Center for Atmospheric Research (NCAR), sponsored by the National Science Foundation. We thank X. Wu for the model and grid development, in addition to preparing the model's input files and executing the parent runs for LVs 1-3. Thanks to other collaborators related to this work including: F. Feddersen, V. Boatwright, H. Zhang, H.Y. Chen and A. Simpson. National Science Foundation (NSF) Graduate Research Fellowship Program Grant numbers DGE-2038238 and DGE-2545911 provided support for SMB. Any opinions, findings, and conclusions or

recommendations expressed in this material are those of the authors and do not necessarily reflect the views of the National Science Foundation or any other funding institution. COAWST development and inspiration for this work came from our wonderful colleague Nirnimesh Kumar, who left us too early and with whom we would have enjoyed discussing these results.

4.6 Supplementary Information

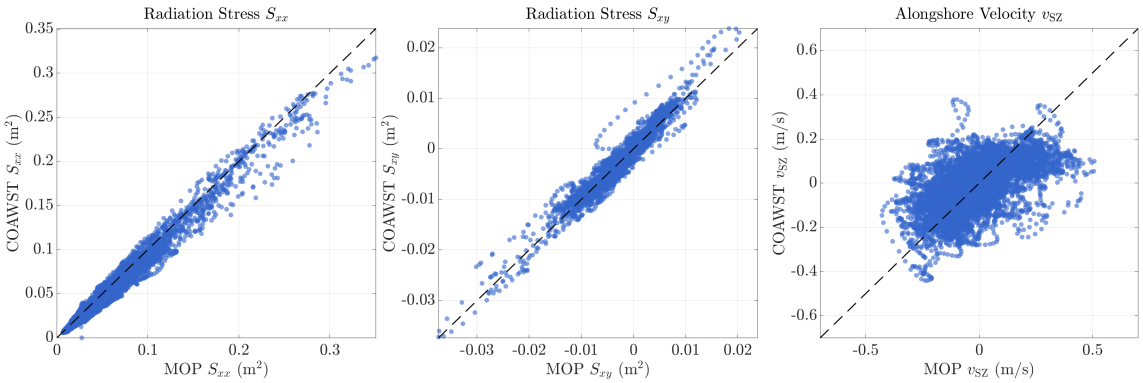


Figure 4.11. Comparison of wave properties (S_{xx}, S_{xy}, and alongshore surf zone current v_{SZ}) between the present study's COAWST model run (y-axis) and Byrne et al. (2026) method using MOP data from the Coastal Data Information Program (x-axis). COAWST surf zone currents here are surface maximum values from the surf zone whereas the MOP approach calculates the current near depth of wave breaking and assumes that the surf zone's cross-shore gradient in S_{xy} is constant. Data shown are averaged over the alongshore by averaging 14 transects surrounding LPL's mouth, and smoothed over 6 hours.

Chapter 5

Conclusions

In this dissertation, I advance what is known about the response of small plumes to variable conditions in the surf zone and inner-shelf. In Chapter 2, I show the occurrence of river plumes in the far-field is influenced by climate patterns using over 100 years of daily salinity measurements. Specifically, negative Pacific Decadal Oscillation and La Niña conditions correspond consistently with dry winters and a lack of plume presence 8 km from the river mouth. Wet winters occur during positive phase Pacific Decadal Oscillation and El Niño winters and produce plumes that travel $\geq$8 km alongshore, although not consistently. This chapter illustrates that small, intermittent freshwater plumes have a robust impact on coastal ocean freshening in the study region.

In Chapter 3, I present the first observational evidence that small plume transport following a storm can be described by regional waves and winds, with a direct contribution from the plume's buoyancy. The occurrence of small plumes in low-inflow systems is typically driven by tides, only forming during ebb tide. However, after sizable rain events, plumes can form regardless of tidal phase. I define a parameter to differentiate tidally-pulsed plumes versus river-driven plumes for given water level, tide, and wave conditions. Additionally, the different dynamic plume regions in the three case studies illustrate the strong event-by-event variability in the transport of even the most strongly forced small plumes during the observational period. While previous work has looked at near-mouth

surf zone properties to determine if a plume is initially surf zone trapped, this work instead considers the influence of the surf zone on plume transport with implications for its ultimate fate. In one of the three cases, I show that the surf zone plays a critical role in far-field plume fate, spreading the plume alongshore more quickly than otherwise possible and likely contributing to mixing. Once a plume is in the far-field region on the inner-shelf, the transport is influenced by winds and its own buoyancy. Ultimately, the precise timing of the river discharge exiting the mouth with regards to the tide, wind, and waves will influence both plume formation and transport.

In Chapter 4, I detail novel interactions that occur due to the surf zone transport of plumes in a region with multiple low-inflow estuaries. While inner-shelf plume coalescence between plumes from multiple rivers is explored in previous literature, I show that surf zone plume coalescence occurs just as commonly. When an incoming surf zone plume reaches another estuary mouth at ebb tide, the incoming plume can be forced offshore to the inner-shelf if the local plume is escaping past the surf zone to the inner-shelf. However, if the local plume is trapped in the surf zone, the incoming plume will continue along in the surf zone with it. In a third case where an incoming surf zone plume reaches an adjacent estuary during flood tide, the incoming plume will intrude into the adjacent estuary. The distance up-estuary a plume intrusion reaches is a function of the strength and timing of the flood tide. The farthest extents are reached when the tidal amplitudes are greatest and when the plume overlaps with the flood tide for the longest duration. I also show how river plumes generally increase the stratification near a river mouth, altering the ambient stratification that a new ebb plume will enter. This has repercussions for the surf zone to inner-shelf exchange of a small plume because it could influence the lateral density gradients and the depths of exchange. The far-field surface plume concentrations are highest in the inner- surf zone, lowest at the surf zone edge, and moderate across the inner-shelf. These findings show how surf zone processes impact the transport and eventual fate of small plumes.

Bibliography

Aguilera Rosana, Gershunov Alexander, Benmarhnia Tarik. Atmospheric rivers impact California's coastal water quality via extreme precipitation // Science of the total environment. 2019. 671. 488–494.

Anderson Donald M, Glibert Patricia M, Burkholder Joann M. Harmful algal blooms and eutrophication: nutrient sources, composition, and consequences // Estuaries. 2002. 25. 704–726.

Arnau Pedro, Liquete Camino, Canals Miquel. River mouth plume events and their dispersal in the Northwestern Mediterranean Sea // OCEANOGRAPHY-WASHINGTON DC-OCEANOGRAPHY SOCIETY-. 2004. 17. 22–31.

Axler Kelia E, Sponaugle Su, Briseño-Avena Christian, Hernandez Jr Frank, Warner Sally J, Dzwonkowski Brian, Dykstra Steven L, Cowen Robert K. Fine-scale larval fish distributions and predator-prey dynamics in a coastal river-dominated ecosystem // Marine Ecology Progress Series. 2020. 650. 37–61.

Baldoni Agnese, Perugini Eleonora, Penna Pierluigi, Parlagreco Luca, Brocchini Maurizio. A comprehensive study of the river plume in a microtidal setting // Estuarine, Coastal and Shelf Science. 2022. 275. 107995.

Banas NS, Hickey BM, MacCready P, Newton JA. Dynamics of Willapa Bay, Washington: A highly unsteady, partially mixed estuary // Journal of Physical Oceanography. 2004. 34, 11. 2413–2427.

Banas NS, MacCready P, Hickey BM. The Columbia River plume as cross-shelf exporter and along-coast barrier // Continental Shelf Research. 2009. 29, 1. 292–301.

Barnston Anthony G, Livezey Robert E. Classification, seasonality and persistence of low-frequency atmospheric circulation patterns // Monthly weather review. 1987. 115, 6. 1083–1126.

Basdurak NB, Largier JL. Wind effects on small-scale river and creek plumes // Journal of Geophysical Research: Oceans. 2022. 127, 12. e2021JC018381.

Basdurak NB, Largier JL, Nidzieko NJ. Modeling the dynamics of small-scale river and creek plumes in tidal waters // Journal of Geophysical Research: Oceans. 2020. 125, 7. e2019JC015737.

Beighley R Edward, Melack John M, Dunne Thomas. IMPACTS OF CALIFORNIA'S CLIMATIC REGIMES AND COASTAL LAND USE CHANGE ON STREAMFLOW CHARACTERISTICS 1 // JAWRA Journal of the American Water Resources Association. 2003. 39, 6. 1419–1433.

Boicourt William C. The circulation of water on the continental shelf from Chesapeake Bay to Cape Hatteras // PhD Dissertation, The John Hopkins University. 1973.

Booij NRRC, Ris Roeland C, Holthuijsen Leo H. A third-generation wave model for coastal regions: 1. Model description and validation // Journal of geophysical research: Oceans. 1999. 104, C4. 7649–7666.

Bowen Anthony J. The generation of longshore currents on a plane beach // Journal of Marine Research. 1969. 27, 2. 206–215.

Brasseale Elizabeth, Feddersen Falk, Wu Xiaodong, Zimmer-Faust Amity G, Giddings Sarah N. Performance of a One-Dimensional Model of Wave-Driven Nearshore Alongshore Tracer Transport and Decay with Applications for Dry Weather Coastal Pollution // Environmental Science & Technology. 2023. 57, 39. 14674–14683.

Bruneau Nicolas, Castelle Bruno, Bonneton Philippe, Pedreros Rodrigo, Almar Rafael, Bonneton Natalie, Bretel Patrice, Parisot Jean-Paul, Sénéchal Nadia. Field observations of an evolving rip current on a meso-macrotidal well-developed inner bar and rip morphology // Continental shelf research. 2009. 29, 14. 1650–1662.

Byrne Sierra M, Giddings Sarah N, Merrifield Mark A, Horner-Devine Alexander R, Spydell Matthew S, Simpson Alexandra J, O'Reilly William C. Processes impacting the fate of small river plumes following storms // Journal of Geophysical Research: Oceans. 2026. 131, 9. e2026JC024342.

Byrne Sierra M, Merrifield Mark A, Carter Melissa L, Cayan Daniel R, Flick Reinhard E, Gershunov Alexander, Giddings Sarah N. Southern California winter precipitation variability reflected in 100-year ocean salinity record // Communications Earth & Environment. 2023. 4, 1. 143.

Campbell RH. Debris flows originating from soil slips during rainstorms in Southern California // Quarterly Journal of Engineering Geology and Hydrogeology. 1974. 7, 4. 339–349.

Cannon Forest, Oakley Nina S, Hecht Chad W, Michaelis Allison, Cordeira Jason M,

Kawzenuk Brian, Demirdjian Reuben, Weihs Rachel, Fish Meredith A, Wilson Anna M, others . Observations and predictability of a high-impact narrow cold-frontal rainband over Southern California on 2 February 2019 // Weather and Forecasting. 2020. 35, 5. 2083–2097.

Carter Melissa L., Flick Reinhard E., Terrill Eric, Beckhaus Elena C., Martin Kayla, Fey Connie L., Walker Patricia W., Largier John L., McGowan John A. Shore Stations Program, La Jolla - Scripps Pier. In Shore Stations Program Data Archive: Current and historical coastal ocean temperature and salinity measurements from California stations. 2022.

Cayan Daniel R, DeHaan Laurel L, Gershunov Alexander, Guzman-Morales Janin, Keeley Jon E, Mumford Joshua, Syphard Alexandra D. Autumn precipitation: the competition with Santa Ana winds in determining fire outcomes in southern California // International Journal of Wildland Fire. 2022. 31, 11. 1056–1067.

Cayan Daniel R, Dettinger Michael D, Diaz Henry F, Graham Nicholas E. Decadal variability of precipitation over western North America // Journal of Climate. 1998. 11, 12. 3148–3166.

Cayan Daniel R, Redmond Kelly T, Riddle Laurence G. ENSO and hydrologic extremes in the western United States // Journal of climate. 1999. 12, 9. 2881–2893.

Chapman William E, Subramanian Aneesh C, Xie Shang-Ping, Sierks Michael D, Ralph F Martin, Kamae Youichi. Monthly modulations of ENSO teleconnections: Implications for potential predictability in North America // Journal of Climate. 2021. 34, 14. 5899–5921.

Clark David B, Feddersen Falk, Guza RT. Cross-shore surfzone tracer dispersion in an alongshore current // Journal of Geophysical Research: Oceans. 2010. 115, C10.

Cloern James E. Our evolving conceptual model of the coastal eutrophication problem // Marine ecology progress series. 2001. 210. 223–253.

Cole Kelly L, Hetland Robert D. The effects of rotation and river discharge on net mixing in small-mouth Kelvin number plumes // Journal of Physical Oceanography. 2016. 46, 5. 1421–1436.

Collins Charine, Macdonald Helen S. Modelling the variability and dynamics of river plumes in Hawke's Bay, Aotearoa New Zealand // Frontiers in Marine Science. 2025. 12. 1536550.

Committee on Natural Disasters , National Research Council . Storms, Floods, and Debris Flows in Southern California and Arizona 1978 and 1980: Proceedings of a Symposium,

September 17-18, 1980. Washington, D.C.: National Academy Press, 1982.

Corringham Thomas W, Ralph F Martin, Gershunov Alexander, Cayan Daniel R, Talbot Cary A. Atmospheric rivers drive flood damages in the western United States // Science advances. 2019. 5, 12. eaax4631.

Dalinghaus Charline, Coco Giovanni, Higuera Pablo. A predictive equation for wave setup using genetic programming // Natural Hazards and Earth System Sciences Discussions. 2022. 2022. 1–20.

Déry Stephen J, Wood Eric F. Decreasing river discharge in northern Canada // Geophysical research letters. 2005. 32, 10.

Des M, DeCastro M, Sousa MC, Dias JM, Gómez-Gesteira M. Hydrodynamics of river plume intrusion into an adjacent estuary: The Minho River and Ria de Vigo // Journal of Marine Systems. 2019. 189. 87–97.

Dettinger Michael D, Ralph Fred Martin, Das Tapash, Neiman Paul J, Cayan Daniel R. Atmospheric rivers, floods and the water resources of California // Water. 2011. 3, 2. 445–478.

Di Lorenzo Emanuele, Schneider Niklas, Cobb Kim M, Franks PJS, Chhak K, Miller Arthur J, McWilliams James C, Bograd Steven J, Arango Hernan, Curchitser Enrique, others . North Pacific Gyre Oscillation links ocean climate and ecosystem change // Geophysical research letters. 2008. 35, 8.

Durocher Martin, Requena Ana I, Burn Donald H, Pellerin Jennifer. Analysis of trends in annual streamflow to the Arctic Ocean // Hydrological Processes. 2019. 33, 7. 1143–1151.

Elwany M Hany S. Characteristics, restoration, and enhancement of Southern California lagoons // Journal of Coastal Research. 2011. 59. 246–255.

Feddersen Falk. Effect of wave directional spread on the radiation stress: Comparing theory and observations // Coastal engineering. 2004. 51, 5-6. 473–481.

Feddersen Falk. Observations of the surf-zone turbulent dissipation rate // Journal of Physical Oceanography. 2012. 42, 3. 386–399.

Feddersen Falk, Boehm Alexandria B, Giddings Sarah N, Wu Xiaodong, Liden Doug. Modeling untreated wastewater evolution and swimmer illness for four wastewater infrastructure scenarios in the San Diego-Tijuana (US/MX) border region // GeoHealth. 2021. 5, 11. e2021GH000490.

Feddersen Falk, Guza RT, Elgar Steve, Herbers THC. Alongshore momentum balances in

the nearshore // Journal of Geophysical Research: Oceans. 1998. 103, C8. 15667–15676.

Feddersen Falk, Trowbridge JH. The effect of wave breaking on surf-zone turbulence and alongshore currents: A modeling study // Journal of Physical Oceanography. 2005. 35, 11. 2187–2203.

Flores Raúl P, Williams Megan E, Horner-Devine Alexander R. River plume modulation by infragravity wave forcing // Geophysical Research Letters. 2022. 49, 15. e2021GL097467.

Fong Derek A, Geyer W Rockwell. Response of a river plume during an upwelling favorable wind event // Journal of Geophysical Research: Oceans. 2001. 106, C1. 1067–1084.

Fong Derek A, Geyer W Rockwell, Signell Richard P. The wind-forced response on a buoyant coastal current: Observations of the western Gulf of Maine plume // Journal of Marine Systems. 1997. 12, 1-4. 69–81.

Garvine Richard W. Physical features of the Connecticut River outflow during high discharge // Journal of Geophysical Research. 1974. 79, 6. 831–846.

Garvine Richard W. Radial spreading of buoyant, surface plumes in coastal waters // Journal of Geophysical Research: Oceans. 1984. 89, C2. 1989–1996.

Garvine Richard W. Estuary plumes and fronts in shelf waters: A layer model // Journal of Physical Oceanography. 1987. 17, 11. 1877–1896.

Garvine Richard W. A dynamical system for classifying buoyant coastal discharges // Continental Shelf Research. 1995. 15, 13. 1585–1596.

Gershunov Alexander, Barnett Tim P. ENSO influence on intraseasonal extreme rainfall and temperature frequencies in the contiguous United States: Observations and model results // Journal of Climate. 1998. 11, 7. 1575–1586.

Gershunov Alexander, Cayan Daniel R. Heavy daily precipitation frequency over the contiguous United States: Sources of climatic variability and seasonal predictability // Journal of Climate. 2003. 16, 16. 2752–2765.

Gershunov Alexander, Shulgina Tamara, Clemesha Rachel ES, Guirguis Kristen, Pierce David W, Dettinger Michael D, Lavers David A, Cayan Daniel R, Polade Suraj D, Kalansky Julie, others . Precipitation regime change in Western North America: the role of atmospheric rivers // Scientific reports. 2019. 9, 1. 9944.

Gershunov Alexander, Shulgina Tamara, Ralph F Martin, Lavers David A, Rutz Jonathan J. Assessing the climate-scale variability of atmospheric rivers affecting western North America // Geophysical Research Letters. 2017. 44, 15. 7900–7908.

Geyer W Rockwell, Hill P, Milligan T, Traykovski P. The structure of the Eel River plume during floods // Continental Shelf Research. 2000. 20, 16. 2067–2093.

Geyer W Rockwell, Signell Richard P. A reassessment of the role of tidal dispersion in estuaries and bays // Estuaries. 1992. 15, 2. 97–108.

Giddings Sarah N, MacCready Parker. Reverse estuarine circulation due to local and remote wind forcing, enhanced by the presence of along-coast estuaries // Journal of Geophysical Research: Oceans. 2017. 122, 12. 10184–10205.

Giddings Sarah N, MacCready Parker, Hickey Barbara M, Banas Neil S, Davis Kristen A, Siedlecki Samantha A, Trainer Vera L, Kudela Raphael M, Pelland Noel A, Connolly Tom P. Hindcasts of potential harmful algal bloom transport pathways on the Pacific Northwest coast // Journal of Geophysical Research: Oceans. 2014. 119, 4. 2439–2461.

Grant Stanley B, Kim Joon Ha, Jones Burton H, Jenkins Scott A, Wasyl Joseph, Cudaback C. Surf zone entrainment, along-shore transport, and human health implications of pollution from tidal outlets // Journal of Geophysical Research: Oceans. 2005. 110, C10.

Grimes Derek J, Feddersen F, Giddings SN. Long-distance/time surf-zone tracer evolution affected by inner-shelf tracer retention and recirculation // Journal of Geophysical Research: Oceans. 2021. 126, 12. e2021JC017661.

Grimes Derek J, Feddersen Falk, Giddings Sarah N, Pawlak Geno. Cross-shore deformation of a surfzone-released dye plume by an internal tide on the inner shelf // Journal of Physical Oceanography. 2020. 50, 1. 35–54.

Guza RT, Thornton EB, Christensen Jr Niels. Observations of steady longshore currents in the surf zone // Journal of physical oceanography. 1986. 16, 11. 1959–1969.

Hally-Rosendahl Kai, Feddersen Falk, Clark David B, Guza RT. Surfzone to inner-shelf exchange estimated from dye tracer balances // Journal of Geophysical Research: Oceans. 2015. 120, 9. 6289–6308.

Hally-Rosendahl Kai, Feddersen Falk, Guza RT. Cross-shore tracer exchange between the surfzone and inner-shelf // Journal of Geophysical Research: Oceans. 2014. 119, 7. 4367–4388.

Harvey Madeleine E, Giddings Sarah N, Pawlak Geno, Crooks Jeffrey A. Hydrodynamic variability of an intermittently closed estuary over interannual, seasonal, fortnightly, and tidal timescales // Estuaries and Coasts. 2023. 46, 1. 84–108.

Harvey Madeleine E, Giddings Sarah N, Stein Eric D, Crooks Jeffrey A, Whitcraft

Christine, Gallien Timu, Largier John L, Tiefenthaler Liesl, Meltzer Hallee, Pawlak Geno, others . Effects of elevated sea levels and waves on southern California estuaries during the 2015–2016 El Niño // Estuaries and Coasts. 2020. 43. 256–271.

Hetland Robert D. Relating river plume structure to vertical mixing // Journal of Physical Oceanography. 2005. 35, 9. 1667–1688.

Hickey B, McCabe R, Geier S, Dever E, Kachel N. Three interacting freshwater plumes in the northern California Current System // Journal of Geophysical Research: Oceans. 2009. 114, C2.

Hickey BM, Pietrafesa Leonard J, Jay David A, Boicourt William C. The Columbia River plume study: Subtidal variability in the velocity and salinity fields // Journal of Geophysical Research: Oceans. 1998. 103, C5. 10339–10368.

Hickey BMSL, Geier S, Kachel N, MacFadyen A. A bi-directional river plume: The Columbia in summer // Continental Shelf Research. 2005. 25, 14. 1631–1656.

Hickey Barbara M, Kudela Raphael M, Nash JD, Bruland Kenneth W, Peterson William T, MacCready P, Lessard Evelyn J, Jay David A, Banas Neil S, Baptista Antonio M, others . River influences on shelf ecosystems: introduction and synthesis // Journal of Geophysical Research: Oceans. 2010. 115, C2.

Ho Minna, Kessouri Fayçal, Frieder Christina A, Sutula Martha, Bianchi Daniele, McWilliams James C. Effect of ocean outfall discharge volume and dissolved inorganic nitrogen load on urban eutrophication outcomes in the Southern California Bight // Scientific Reports. 2023. 13, 1. 22148.

Horner-Devine Alexander R, Hetland Robert D, MacDonald Daniel G. Mixing and transport in coastal river plumes // Annual Review of Fluid Mechanics. 2015. 47. 569–594.

Horner-Devine Alexander R, Jay David A, Orton Philip M, Spahn Emily Y. A conceptual model of the strongly tidal Columbia River plume // Journal of Marine Systems. 2009. 78, 3. 460–475.

Howard Meredith DA, Sutula Martha, Caron David A, Chao Yi, Farrara John D, Frenzel Hartmut, Jones Burton, Robertson George, McLaughlin Karen, Sengupta Ashmita. Anthropogenic nutrient sources rival natural sources on small scales in the coastal waters of the Southern California Bight // Limnology and Oceanography. 2014. 59, 1. 285–297.

Huang Boyin, Thorne Peter W, Banzon Viva F, Boyer Tim, Chepurin Gennady, Lawrimore Jay H, Menne Matthew J, Smith Thomas M, Vose Russell S, Zhang Huai-Min. Extended reconstructed sea surface temperature, version 5 (ERSSTv5): upgrades, validations, and intercomparisons // Journal of Climate. 2017. 30, 20. 8179–8205.

Iglesias I, Buschman FA, Simone G, Amorim F, Bio A, Vieira LR, Boisgontier H, Zaggia L, Moschino V, Madricardo F, others . Hydrodynamics of a highly stratified small estuary and the influence of nearby river plumes // Estuarine, Coastal and Shelf Science. 2024. 304. 108843.

Kakoulaki Georgia, MacDonald Daniel, Horner-Devine Alexander R. The role of wind in the near field and midfield of a river plume // Geophysical Research Letters. 2014. 41, 14. 5132–5138.

Kalnay Eugenia, Kanamitsu Masao, Kistler Robert, Collins William, Deaven Dennis, Gandin Lev, Iredell Mark, Saha Suranjana, White Glenn, Woollen John, others . The NCEP/NCAR 40-year reanalysis project // Bulletin of the American Meteorological Society. 1996. 77, 3. 437–472.

Kastner SE, Horner-Devine AR, Thomson JM. A conceptual model of a river plume in the surf zone // Journal of Geophysical Research: Oceans. 2019. 124, 11. 8060–8078.

Kastner Samuel Evan, Horner-Devine AR, Thomson J. The influence of wind and waves on spreading and mixing in the Fraser River plume // Journal of Geophysical Research: Oceans. 2018. 123, 9. 6818–6840.

Kastner Samuel Evan, Horner-Devine Alex R, Thomson JM, Giddings SN. Observations of river plume mixing in the surf zone // Journal of Physical Oceanography. 2023. 53, 3. 959–977.

Kniskern Tara A, Warrick Jonathan A, Farnsworth Katherine L, Wheatcroft Robert A, Goni Miguel A. Coherence of river and ocean conditions along the US West Coast during storms // Continental Shelf Research. 2011. 31, 7-8. 789–805.

Kumar Nirnimesh, Feddersen Falk. The effect of Stokes drift and transient rip currents on the inner shelf. Part II: With stratification // Journal of Physical Oceanography. 2017. 47, 1. 243–260.

Kumar Nirnimesh, Voulgaris George, Warner John C, Olabarrieta Maitane. Implementation of the vortex force formalism in the coupled ocean-atmosphere-wave-sediment transport (COAWST) modeling system for inner shelf and surf zone applications // Ocean Modelling. 2012. 47. 65–95.

Largier John L. Recognizing Low-Inflow Estuaries as a Common Estuary Paradigm // Estuaries and Coasts. 2023. 46, 8. 1949–1970.

Lemagie Emily, Lerczak James. The evolution of a buoyant river plume in response to a pulse of high discharge from a small midlatitude river // Journal of Physical Oceanography. 2020. 50, 7. 1915–1935.

Lemos Angelo Teixeira, Gama Mateus Alexander Campeche, Bernardes Marcos Eduardo Cordeiro, Silva Allison Gonçalves, Siegle Eduardo. Dispersal of a small wave-protected river plume from drifter observations // Regional Studies in Marine Science. 2022. 55. 102513.

Lentz Steven J, Fewings Melanie R. The wind-and wave-driven inner-shelf circulation // Annual review of marine science. 2012. 4. 317–343.

Li Andy K, Paek Houk, Yu Jin-Yi. The changing influences of the AMO and PDO on the decadal variation of the Santa Ana winds // Environmental Research Letters. 2016. 11, 6. 064019.

Li Xiangyu, Klingbeil Knut, Burchard Hans. Introducing the coincidence index: A novel diagnostic and production-based framework for water body interaction analysis and its application to study the interaction of river plumes // Journal of Advances in Modeling Earth Systems. 2026. 18, 8. e2026MS005737.

Liu Tao, McGuire Luke A, Oakley Nina, Cannon Forest. Temporal changes in rainfall intensity duration thresholds for post-wildfire flash floods in southern California // Natural Hazards and Earth System Sciences. 2022. 22, 2. 361–376.

Liu Yi-Chin, Di Pingkuan, Chen Shu-Hua, DaMassa John. Relationships of rainy season precipitation and temperature to climate indices in California: long-term variability and extreme events // Journal of Climate. 2018. 31, 5. 1921–1942.

Liu Yonggang, MacCready Parker, Hickey Barbara M. Columbia River plume patterns in summer 2004 as revealed by a hindcast coastal ocean circulation model // Geophysical Research Letters. 2009. 36, 2.

Livneh Ben, Rosenberg Eric A, Lin Chiyu, Nijssen Bart, Mishra Vimal, Andreadis Kostas M, Maurer Edwin P, Lettenmaier Dennis P. A long-term hydrologically based dataset of land surface fluxes and states for the conterminous United States: Update and extensions // Journal of Climate. 2013. 26, 23. 9384–9392.

Longuet-Higgins Michael S. Longshore currents generated by obliquely incident sea waves: 1 // Journal of geophysical research. 1970. 75, 33. 6778–6789.

Longuet-Higgins Michael S, Stewart RW. A note on wave set-up // Journal of Marine Research. 1963.

Longuet-Higgins Michael S, Stewart RW. Radiation stresses in water waves; a physical discussion, with applications // Deep sea research and oceanographic abstracts. 11, 4. 1964. 529–562.

Lou Yingzhong. Dynamics of Small-Scale River Plumes in the Surf Zone: Idealized and Realistic Modeling. 2025.

Lou Yingzhong, Horner-Devine Alexander R, Derakhti Morteza, Giddings Sarah N, Spydell Matthew S, Rodriguez Angelica R, Simpson Alexandra J. Dynamics and scaling of a small river discharging into the surf zone // Journal of Physical Oceanography. 2025.

MacDonald Daniel G, Geyer W Rockwell. Turbulent energy production and entrainment at a highly stratified estuarine front // Journal of Geophysical Research: Oceans. 2004. 109, C5.

Mantua Nathan J, Hare Steven R, Zhang Yuan, Wallace John M, Francis Robert C. A Pacific interdecadal climate oscillation with impacts on salmon production // Bulletin of the american Meteorological Society. 1997. 78, 6. 1069–1080.

Mazzini Piero LF, Barth John A, Shearman R Kipp, Erofeev A. Buoyancy-driven coastal currents off Oregon during fall and winter // Journal of Physical Oceanography. 2014. 44, 11. 2854–2876.

McSweeney SL, Kennedy DM, Rutherfurd ID, Stout JC. Intermittently Closed/Open Lakes and Lagoons: Their global distribution and boundary conditions // Geomorphology. 2017. 292. 142–152.

Milliman John D, Farnsworth Katherine L. River discharge to the coastal ocean: a global synthesis. 2013.

Milliman John D, Syvitski James PM. Geomorphic/tectonic control of sediment discharge to the ocean: the importance of small mountainous rivers // The journal of Geology. 1992. 100, 5. 525–544.

Mo Kingtse C, Livezey Robert E. Tropical-extratropical geopotential height teleconnections during the Northern Hemisphere winter // Monthly Weather Review. 1986. 114, 12. 2488–2515.

Modrick Theresa M, Georgakakos Konstantine P. The character and causes of flash flood occurrence changes in mountainous small basins of Southern California under projected climatic change // Journal of Hydrology: Regional Studies. 2015. 3. 312–336.

Moulton M, Chickadel CC, Thomson J. Warm and cool nearshore plumes connecting the surf zone to the inner shelf // Geophysical Research Letters. 2021. 48, 10. e2020GL091675.

Moulton Melissa, Elgar Steve, Raubenheimer Britt, Warner John C, Kumar Nirnimesh. Rip currents and alongshore flows in single channels dredged in the surf zone // Journal of Geophysical Research: Oceans. 2017. 122, 5. 3799–3816.

Muller Caroline J, Back Larissa E, O'Gorman Paul A, Emanuel Kerry A. A model for the relationship between tropical precipitation and column water vapor // Geophysical Research Letters. 2009. 36, 16.

Nash Jonathan D, Kilcher Levi F, Moum James N. Structure and composition of a strongly stratified, tidally pulsed river plume // Journal of Geophysical Research: Oceans. 2009. 114, C2.

Nezlin Nikolay P, DiGiacomo Paul M, Stein Eric D, Ackerman Drew. Stormwater runoff plumes observed by SeaWiFS radiometer in the Southern California Bight // Remote Sensing of Environment. 2005. 98, 4. 494–510.

O'Reilly William C, Olfe Corey B, Thomas Julianna, Seymour RJ, Guza RT. The California coastal wave monitoring and prediction system // Coastal Engineering. 2016. 116. 118–132.

Oakley NS, Lancaster JT, Hatchett BJ, Stock J, Ralph FM, Roj S, Lukashov S. A 22-year climatology of cool season hourly precipitation thresholds conducive to shallow landslides in California // Earth Interactions. 2018. 22, 14. 1–35.

Okubo A. Effect of shoreline irregularities on streamwise dispersion in estuaries and other embayments // Netherlands Journal of Sea Research. 1973. 6, 1-2. 213–224.

Okun K, Desai A, Parnell PE, Masunaga E, Lucas AJ, Lerczak J, Pawlak G. Semidiurnal inner shelf flow in the Southern California Bight // Journal of Geophysical Research: Oceans. 2025. 130, 5. e2024JC021591.

Oppenheim Alan V. Discrete-time signal processing. 1999.

Orescanin Mara M, Scooler Jeff. Observations of episodic breaching and closure at an ephemeral river // Continental Shelf Research. 2018. 166. 77–82.

Osadchiev Alexander, Barymova Alexandra, Sedakov Roman, Zhiba Roman, Dbar Roman. Spatial structure, short-temporal variability, and dynamical features of small river plumes as observed by aerial drones: Case study of the Kodor and Bzyp river plumes // Remote Sensing. 2020. 12, 18. 3079.

Osadchiev Alexander, Sedakov Roman, Barymova Alexandra. Response of a small river plume on wind forcing // Frontiers in Marine Science. 2021. 8. 809566.

Pan Rui, Wu Xiaodong, Giddings Sarah N. Coastal submesoscale eddy distortion and its impacts on the cross-shore and vertical tracer transport // Journal of Geophysical Research: Oceans. 2025. 130, 8. e2025JC022351.

Paulsen May-Linn, Andersson Andreas J, Aluwihare Lihini, Cyronak Tyler, D'Angelo Sydney, Davidson Charlie, Elwany Hany, Giddings Sarah N, Page Heather N, Porrachia Magali, others . Temporal changes in seawater carbonate chemistry and carbon export from a Southern California estuary // Estuaries and Coasts. 2018. 41, 4. 1050–1068.

Piñones A, Valle-Levinson A, Narváez DA, Vargas CA, Navarrete SA, Yuras G, Castilla JC. Wind-induced diurnal variability in river plume motion // Estuarine, Coastal and Shelf Science. 2005. 65, 3. 513–525.

IPCC, 2022: Summary for policymakers. // . 2022.

Pritchard Mark, Huntley David A. A simplified energy and mixing budget for a small river plume discharge // Journal of Geophysical Research: Oceans. 2006. 111, C3.

Rabouille C, Conley DJ, Dai MH, Cai W-J, Chen CTA, Lansard B, Green R, Yin K, Harrison PJ, Dagg M, others . Comparison of hypoxia among four river-dominated ocean margins: The Changjiang (Yangtze), Mississippi, Pearl, and Rhone rivers // Continental Shelf Research. 2008. 28, 12. 1527–1537.

Ralph F Martin, Rutz Jonathan J, Cordeira Jason M, Dettinger Michael, Anderson Michael, Reynolds David, Schick Lawrence J, Smallcomb Chris. A scale to characterize the strength and impacts of atmospheric rivers // Bulletin of the American Meteorological Society. 2019. 100, 2. 269–289.

Raphael Marilyn, Mills Gerald. The role of mid-latitude Pacific cyclones in the winter precipitation of California // The Professional Geographer. 1996. 48, 3. 251–262.

Rayner NAA, Parker De E, Horton EB, Folland Chris K, Alexander Lisa V, Rowell DP, Kent Elizabeth C, Kaplan A. Global analyses of sea surface temperature, sea ice, and night marine air temperature since the late nineteenth century // Journal of Geophysical Research: Atmospheres. 2003. 108, D14.

Reeves Ryan L, Grant Stanley B, Mrse Robert D, Copil Oancea Carmen M, Sanders Brett F, Boehm Alexandria B. Scaling and management of fecal indicator bacteria in runoff from a coastal urban watershed in southern California // Environmental science & technology. 2004. 38, 9. 2637–2648.

Roco Alonso, Flores Raúl P, Williams Megan E, Saldías Gonzalo S. Observations of river-wave interactions at a small-scale river mouth // Coastal Engineering. 2024. 189. 104456.

Rodrigues Raphael Paiva, Knoppers Bastiaan Adriaan, Souza Weber Friederichs Landim de, Santos Elisamara Sabadini. Suspended matter and nutrient gradients of a small-scale river plume in Sepetiba Bay, SE-Brazil // Brazilian Archives of Biology and Technology.

2009. 52, 2. 503–512.

Rodriguez Angelica R, Giddings Sarah N, Kumar Nirnimesh. Impacts of nearshore wave-current interaction on transport and mixing of small-scale buoyant plumes // Geophysical Research Letters. 2018. 45, 16. 8379–8389.

Roegner Curtis G, Hickey Barbara M, Newton Jan A, Shanks Alan L, Armstrong David A. Wind-induced plume and bloom intrusions into Willapa Bay, Washington // Limnology and Oceanography. 2002. 47, 4. 1033–1042.

Rojas Cristian M, Saldías Gonzalo S, Flores Raúl P, Vásquez Sebastián I, Salas Cristian, Vargas Cristian A. A modeling study of hydrographic and flow variability along the river-influenced coastal ocean off central Chile // Ocean Modelling. 2023. 181. 102155.

Romero Leonel, Siegel David A, McWilliams James C, Uchiyama Yusuke, Jones Charles. Characterizing storm water dispersion and dilution from small coastal streams // Journal of Geophysical Research: Oceans. 2016. 121, 6. 3926–3943.

Ropelewski Chester F, Halpert Michael S. North American precipitation and temperature patterns associated with the El Niño/Southern Oscillation (ENSO) // Monthly Weather Review. 1986. 114, 12. 2352–2362.

Rosa Alexandra, Cardoso Cláudio, Vieira Rui, Faria Ricardo, Oliveira Ana R, Navarro Gabriel, Caldeira Rui MA. Impact of flash flood events on the coastal waters around madeira island: the "Land Mass Effect" // Frontiers in Marine Science. 2022. 8. 749638.

Ryther John H, Menzel David Washington, Menzel David W, Corwin Nathaniel. Influence of the Amazon River Outflow on the Ecology of the Western Tropical Atlantic: Hydrography and nutrient chemistry. I. 1967.

Salcedo-Castro Julio, Saldías Gonzalo S, Saavedra Freddy, Donoso David. Climatology of Maipo and Rapel river plumes off Central Chile from numerical simulations // Regional Studies in Marine Science. 2020. 38. 101389.

Saldías Gonzalo S, Sobarzo Marcus, Largier John, Moffat Carlos, Letelier Ricardo. Seasonal variability of turbid river plumes off central Chile based on high-resolution MODIS imagery // Remote Sensing of Environment. 2012. 123. 220–233.

Schwing Franklin B, Mendelssohn Roy. Increased coastal upwelling in the California Current System // Journal of Geophysical Research: Oceans. 1997. 102, C2. 3421–3438.

Sharples Jonathan, Middelburg Jack J, Fennel Katja, Jickells Timothy D. What proportion of riverine nutrients reaches the open ocean? // Global Biogeochemical Cycles. 2017. 31, 1. 39–58.

Shchepetkin Alexander F, McWilliams James C. The regional oceanic modeling system (ROMS): a split-explicit, free-surface, topography-following-coordinate oceanic model // Ocean modelling. 2005. 9, 4. 347–404.

Shepard FP. Undertow, rip tide or" rip current" // Science. 1936. 84, 2173. 181–182.

Shukla Shraddhanand, Steinemann Anne, Iacobellis Sam F, Cayan Daniel R. Annual drought in California: Association with monthly precipitation and climate phases // Journal of Applied Meteorology and Climatology. 2015. 54, 11. 2273–2281.

Sousa MC, Vaz N, Alvarez I, Gomez-Gesteira M, Dias JM. Modeling the Minho River plume intrusion into the rias Baixas (NW Iberian Peninsula) // Continental Shelf Research. 2014. 85. 30–41.

Speiser William H, Largier John L. Long-term observations of the turbid outflow plume from the Russian River, California // Estuarine, Coastal and Shelf Science. 2024. 309. 108942.

Spydell Matthew S, Feddersen Falk, Suanda Sutara. Inhomogeneous turbulent dispersion across the nearshore induced by surfzone eddies // J. Phys. Oceanogr. 2019. 49, 4. 1015–1034.

Stockdon Hilary F, Holman Rob A, Howd Peter A, Sallenger Jr Asbury H. Empirical parameterization of setup, swash, and runup // Coastal engineering. 2006. 53, 7. 573–588.

Sutula Martha, Ho Minna, Sengupta Ashmita, Kessouri Fayçal, McLaughlin Karen, McCune Kenny, Bianchi Daniele. A baseline of terrestrial freshwater and nitrogen fluxes to the Southern California Bight, USA // Marine pollution bulletin. 2021. 170. 112669.

Swieca Kelsey, Sponaugle Su, Briseño-Avena Christian, Schmid Moritz S, Brodeur Richard D, Cowen Robert K. Changing with the tides: fine-scale larval fish prey availability and predation pressure near a tidally modulated river plume // Marine Ecology Progress Series. 2020. 650. 217–238.

Syed Tajdarul H, Famiglietti James S, Chambers Don P, Willis Josh K, Hilburn Kyle. Satellite-based global-ocean mass balance estimates of interannual variability and emerging trends in continental freshwater discharge // Proceedings of the National Academy of Sciences. 2010. 107, 42. 17916–17921.

Syvitski James PM, Milliman John D. Geology, geography, and humans battle for dominance over the delivery of fluvial sediment to the coastal ocean // The Journal of Geology. 2007. 115, 1. 1–19.

Thornton Edward B, Guza R T. Energy saturation and phase speeds measured on a

natural beach // J. Geophys. Res. 1982. 87, C12. 9499–9508.

Thornton Edward B, Guza RT. Transformation of wave height distribution // Journal of Geophysical Research: Oceans. 1983. 88, C10. 5925–5938.

Thornton Edward B, Guza RT. Surf zone longshore currents and random waves: Field data and models // Journal of Physical Oceanography. 1986. 16, 7. 1165–1178.

Toublanc F, Ayoub NK, Marsaleix P. On the role of wind and tides in shaping the Gironde River plume (Bay of Biscay) // Continental Shelf Research. 2023. 253. 104891.

Vargas Cristian A, Narváez Diego A, Piñones Andrea, Navarrete Sergio A, Lagos Nelson A. River plume dynamic influences transport of barnacle larvae in the inner shelf off central Chile // Journal of the Marine Biological Association of the United Kingdom. 2006. 86, 5. 1057–1065.

Vargas-Fonseca Elena, Olds Andrew D, Gilby Ben L, Connolly Rod M, Schoeman David S, Huijbers Chantal M, Hyndes Glenn A, Schlacher Thomas A. Combined effects of urbanization and connectivity on iconic coastal fishes // Diversity and Distributions. 2016. 22, 12. 1328–1341.

Vundavilli Hemanth, Mullarney Julia C, MacDonald Iain T. The influence of river plume discharge and winds on sediment transport into a coastal mangrove environment // Estuaries and Coasts. 2024. 47, 5. 1236–1254.

Wang Daoping, Guan Dabo, Zhu Shupeng, Kinnon Michael Mac, Geng Guannan, Zhang Qiang, Zheng Heran, Lei Tianyang, Shao Shuai, Gong Peng, others . Economic footprint of California wildfires in 2018 // Nature Sustainability. 2021. 4, 3. 252–260.

Warner John C, Armstrong Brandy, He Ruoying, Zambon Joseph B. Development of a coupled ocean–atmosphere–wave–sediment transport (COAWST) modeling system // Ocean modelling. 2010. 35, 3. 230–244.

Warrick Jonathan A, DiGiacomo Paul M, Weisberg Stephen B, Nezlin Nikolay P, Mengel M, Jones Burton H, Ohlmann J Carter, Washburn Libe, Terrill Eric J, Farnsworth Katie L. River plume patterns and dynamics within the Southern California Bight // Continental Shelf Research. 2007. 27, 19. 2427–2448.

Warrick Jonathan A, Farnsworth Katherine L. Coastal river plumes: Collisions and coalescence // Progress in oceanography. 2017. 151. 245–260.

Warrick Jonathan A, Fong Derek A. Dispersal scaling from the world's rivers // Geophysical Research Letters. 2004. 31, 4.

Westerling Anthony L, Swetnam Thomas W. Interannual to decadal drought and wildfire in the western United States // EOS, Transactions American Geophysical Union. 2003. 84, 49. 545–555.

Wetz Michael S, Hales Burke, Chase Zanna, Wheeler Patricia A, Whitney Michael M. Riverine input of macronutrients, iron, and organic matter to the coastal ocean off Oregon, USA, during the winter // Limnology and Oceanography. 2006. 51, 5. 2221–2231.

Whitney Michael M, Garvine Richard W. Wind influence on a coastal buoyant outflow // Journal of Geophysical Research: Oceans. 2005. 110, C3.

Whitney Michael M, Jia Yan, McManus Pearse M, Kunz Christopher J. Sill effects on physical dynamics in eastern Long Island Sound // Ocean Dynamics. 2014. 64. 443–458.

Williams Megan E, Stacey Mark T. Tidally discontinuous ocean forcing in bar-built estuaries: The interaction of tides, infragravity motions, and frictional control // Journal of Geophysical Research: Oceans. 2016. 121, 1. 571–585.

Wong Kuo-Chuin, Lu Xin. Low-frequency variability in Delaware's inland bays // Journal of Geophysical Research: Oceans. 1994. 99, C6. 12683–12695.

Wong Simon HC, Monismith Stephen G, Boehm Alexandria B. Simple estimate of entrainment rate of pollutants from a coastal discharge into the surf zone // Environmental science & technology. 2013. 47, 20. 11554–11561.

Wright LD, Coleman James M. Effluent expansion and interfacial mixing in the presence of a salt wedge, Mississippi River delta // Journal of Geophysical Research. 1971. 76, 36. 8649–8661.

Wu Xiaodong, Feddersen Falk, Giddings Sarah N. Automated temporal tracking of coherently evolving density fronts in numerical models // Journal of Atmospheric and Oceanic Technology. 2021a. 38, 12. 2095–2108.

Wu Xiaodong, Feddersen Falk, Giddings Sarah N. Characteristics and dynamics of density fronts over the inner to midshelf under weak wind conditions // Journal of Physical Oceanography. 2021b. 51, 3. 789–808.

Wu Xiaodong, Feddersen Falk, Giddings Sarah N. Diagnosing surfzone impacts on inner-shelf flow spatial variability using realistic model experiments with and without surface gravity waves // Journal of Physical Oceanography. 2021c. 51, 8. 2505–2515.

Wu Xiaodong, Feddersen Falk, Giddings Sarah N, Kumar Nirnimesh, Gopalakrishnan Ganesh. Mechanisms of mid-to outer-shelf transport of shoreline-released tracers // Journal of Physical Oceanography. 2020. 50, 7. 1813–1837.

Yankovsky Elizabeth, Yankovsky Alexander. The cross-shelf regime of a wind-driven supercritical river plume // Journal of Physical Oceanography. 2024. 54, 2. 537–556.

Yuan Yeping, Horner-Devine Alexander R. Laboratory investigation of the impact of lateral spreading on buoyancy flux in a river plume // Journal of Physical Oceanography. 2013. 43, 12. 2588–2610.